THE UNIVERSITY of EDINBURGH
School of Engineering

Cryo-SEM visualization of bulk nanobubbles in aqueous solutions

Diploma thesis

Student: Evangelos Patounas

Supervisors:

Professor Vasileios Koutsos

Professor Doros Theodorou

October 2020

Acknowledgements

The present diploma thesis was undertaken at the Institute for Materials and Processes of the University of Edinburgh, under the supervision of the Head of Research Institute Prof. Vasileios Koutsos.

I would like to wholeheartedly thank Professor Vasileios Koutsos for giving me the opportunity to conduct research for my diploma thesis at the University of Edinburgh. Being a student in Edinburgh was a unique experience and being supervised by Prof. Koutsos gave me a better understanding of research and the challenges it entails.

At the same time, I would like to thank Professor Doros Theodorou for his willingness and trust to become my supervisor at the NTUA, his support and cooperation throughout the implementation of my thesis.

Moreover, I would like to thank all the community of students and faculty at the University of Edinburgh for supporting me and especially Dr Norbert Radacsi for helping me with the conduction of my experiments and for making me feel a part of his research group.

Finally, as I now complete the circle of my undergraduate studies, I would like to thank my family and friends for all the experiences we shared during the last five years, that have defined me and will forever stay in my heart.

Evangelos Patounas,

Athens 2020

Abstract

The objective of this diploma thesis is to identify nanobubbles present in bulk solutions, with regard to their morphology and size, by implementing cryo-SEM measurements. Particularly, aqueous samples containing O_2 and N_2 bulk nanobubbles in pure water and pure water blended with magnetic ionic liquid, that are produced with hydrodynamic cavitation in the Materials & Membranes for Environmental Separations Laboratory of NCSR "Demokritos" were visualized by applying cryo scanning electron microscopy (cryo-SEM).

This is the first study where the technique of cryo-SEM is applied for the observation of bulk nanobubbles in aqueous solutions. Cryo-SEM enables high-resolution and preservation of the morphology of the initial sample, as the sample is abruptly frozen in a manner that retains the structure of its contents.

In the case of this study, rapid freezing was performed with liquid nitrogen both at ambient pressure and at high-pressure of 2000 bar. Subsequently, cryo-SEM imaging was applied, analysis was performed, and conclusions were extracted from the visualization regarding the size and morphology of the bulk nanobubbles present in the samples.

Spherical formations attributed to oxygen NBs were observed in pure water and pure water blended with magnetic ionic liquid after preliminary freezing both at ambient pressure and high pressure (2000 bar). However, nitrogen nanobubbles could not be identified. The influence of pressure and the formation of ice during the freezing process, as well as the influence of the magnetic ionic liquid are assessed.

Moreover, the formations that were observed, attributed to bulk nanobubbles, were compared to results of other similar studies and the measured sizes of the observed bubbles from this direct imaging technique were correlated with the results of dynamic light scattering (DLS) and Tyndall effect obtained for the bubbles previously at NCSR "Demokritos".

Περίληψη

Το αντικείμενο αυτής της διπλωματικής εργασίας είναι να ταυτοποιήσει νανοφυσαλλίδες παρούσες σε συνεχή υγρά διαλύματα ως προς τη μορφολογία και το μέγεθός τους, χρησιμοποιώντας τη μέθοδο της κρυο-ηλεκτρονικής μικροσκοπίας σάρωσης (cryo-SEM). Πιο συγκεκριμένα, υδατικά δείγματα που περιέχουν νανοφυσαλλίδες συνεχούς φάσεως γεμάτες από O_2 και N_2 σε καθαρό νερό και καθαρό νερό αναμεμειγμένο με μαγνητικό ιοντικό υγρό, που παράγονται μέσω υδροδυναμικής σπηλαίωσης στο Εργαστήριο Υλικών και Μεμβρανών για Περιβαλλοντικούς Διαχωρισμούς στο ΕΚΕΦΕ "Δημόκριτος", οπτικοποιήθηκαν εφαρμόζοντας κρυο-ηλεκτρονική μικροσκοπία σάρωσης (cryo-SEM).

Αυτή είναι η πρώτη μελέτη όπου εφαρμόζεται η τεχνική της κρυο-ηλεκτρονικής μικροσκοπίας σάρωσης για την παρατήρηση νανοφυσαλλίδων σε συνεχείς φάσεις υδατικών διαλυμάτων. Η cryo-SEM επιτρέπει υψηλή διακριτική ικανότητα και διατήρηση της μορφολογίας του αρχικού δείγματος, καθώς το δείγμα παγώνει απότομα κατά τρόπο που αφήνει αμετάβλητη τη δομή του περιεχομένου του.

Στην περίπτωση αυτής της μελέτης, η απότομη πήξη των δειγμάτων επιτεύχθηκε με υγρό άζωτο, τόσο υπό ατμοσφαιρική πίεση, όσο και σε υψηλή πίεση 2000 bar. Ακολούθησε παρατήρηση των δειγμάτων με cryo-SEM, ανάλυση των αποτελεσμάτων και εξαγωγή συμπερασμάτων από την οπτικοποίηση για το μέγεθος και τη μορφολογία των νανοφυσαλλίδων συνεχούς υγρής φάσης μέσα στα δείγματα.

Σφαιρικοί σχηματισμοί που αποδόθηκαν σε νανοφυσαλλίδες οξυγόνου παρατηρήθηκαν σε καθαρό νερό και καθαρό νερό αναμεμειγμένο με μαγνητικό ιοντικό υγρό τόσο μετά από πήξη σε ατμοσφαιρική πίεση όσο και μετά από πήξη σε υψηλή πίεση (2000 bar). Ωστόσο, νανοφυσαλλίδες αζώτου δεν παρατηρήθηκαν. Η επίδραση της πίεσης και ο σχηματισμός πάγου κατά την διεργασία πήξης, καθώς και η επίδραση του μαγνητικού ιοντικού υγρού αξιολογούνται.

Ακόμα, οι σχηματισμοί που παρατηρήθηκαν, αποδιδόμενοι σε νανοφυσαλλίδες συνεχούς φάσης, συγκρίθηκαν προς τα αποτελέσματα άλλων, παρόμοιων μελετών και τα μετρούμενα μεγέθη των παρατηρούμενων νανοφυσαλλίδων απ' αυτήν την άμεση τεχνική οπτικοποίησης συσχετίστηκαν με αποτελέσματα από μετρήσεις δυναμικής σκέδασης φωτός (DLS) και φαινομένου Tyndall, που έχουν ληφθεί στο παρελθόν στο ΕΚΕΦΕ "Δημόκριτος".

Introduction

Nanobubbles are defined as gas-containing cavities with diameter less than 1 μm in a liquid solution. They can be found at a solid-liquid interface and in this case they are called surface nanobubbles, or they can be dispersed in a bulk liquid phase and then they are called bulk nanobubbles. Nanobubbles are receiving increasing attention over the past few years, due to their promising applications ranging from flotation, water treatment and surface cleaning to cancer treatment and drug delivery.

Recently cryo-electron microscopy techniques have given the opportunity to obtain images of nanobubbles and better understand their morphology, which could provide further information on their stability and the mechanisms behind their long-term existence. Having a better understanding of their nature could subsequently help us acknowledge their influence on each process they are applied to, and further improve the already-existing processes.

In this study, cryo-Scanning Electron Microscopy (cryo-SEM) is applied for the observation of O_2 and N_2 bulk NBs in pure water and pure water blended with magnetic ionic liquid (MIL). The goal is to assess if the cryo-SEM technique can be applied effectively for the observation of bulk nanobubbles, towards the standardization of a process for observing nanobubbles.

Therefore, not only the morphology and size of the nanobubbles imaged were assessed but also how the sample preparation technique for the cryo-SEM imaging influences the resulted images, and how the formations imaged could differ from those present in the initial sample.

This diploma thesis is situated into three main chapters. The first chapter constitutes a literature review of bulk and surface nanobubbles, the second chapter presents the cryo-SEM technique applied, the images obtained and discusses the results of our study while comparing them to the literature, whereas in the third chapter the conclusions of this study are presented.

Specifically, in the first chapter the stability mechanisms, the production methods, the applications and the characterisation methods for bulk and surface nanobubbles are presented. Emphasis is laid on the electron microscopy research for the characterisation of nanobubbles, as the visualization performed with the cryo-SEM technique can be directly compared to the results of these studies.

In chapter 2, firstly an introduction to cryo-electron microscopy techniques is made and the procedure followed for the cryo-SEM imaging is described in detail. Afterwards, the images obtained by the cryo-SEM imaging are presented and the images of each type of sample are discussed in detail. Lastly, images obtained by the cryo-SEM imaging are compared to those of the literature.

In chapter 3, conclusions are drawn based on the discussion of the results in chapter 2. Also, directions in which this work could be continued, towards the effective visualization of bulk nanobubbles, are described. With this chapter, the presentation of the diploma thesis is completed.

Contents

Chapter 1: Literature Review 1
1. Introduction to NBs 1
2. Stability of NBs 3
2.1 Stability of surface NBs 3
2.2 Stability of bulk NBs 4
3. Production methods 6
3.1 Production of bulk NBs 6
3.2 Production of surface NBs 7
4. Applications 8
4.1 Flotation 8
4.2 Water treatment 8
4.3 Surface cleaning 9
4.4 Biological applications 10
5. Characterization methods of NBs 11
5.1 Bulk NBs 11
5.2 Surface NBs 18
6. Future of NBs 19
Chapter 2: Cryo-SEM imaging 20
1. Introduction to cryo-SEM 20
2. Procedure followed for the cryo-SEM imaging 21
3. Cryo-SEM results 25
3.1 Pure water with O_2 NBs 25
3.2 Pure water with O_2 NBs blended with magnetic ionic liquid (MIL), 20% v/v 32
3.3 Pure water with N_2 NBs 39
3.4 Pure water with N_2 NBs blended with magnetic ionic liquid (MIL), 20% v/v 42
4. Discussion 46
4.1 Pure water with O_2 NBs 46
4.2 Pure water with O_2 NBs blended with magnetic ionic liquid (MIL), 20% v/v 47
4.3 Pure water with N_2 NBs 49
4.4 Pure water with N_2 NBs blended with magnetic ionic liquid (MIL), 20% v/v 49
5. Comparison of results with literature 50
Chapter 3: Conclusions and Outlook 53
References 55

Chapter 1: Literature Review

1. Introduction to NBs

Nanobubbles (NBs) are classified into three categories: surface NBs (nanoscopic spherical-cap-shaped domains that are found at a solid/liquid interface) [1], micropancakes (quasi-two-dimensional gaseous domains present at a solid/liquid interface) [2] and bulk NBs (nanoscopic gaseous domains dispersed in a bulk liquid) [3]. Surface NBs present typical widths and heights of 50-100 nm and 10-20 nm respectively, whereas micropancakes have a diameter of several microns, but their height is only 1-2 nm [7]. Bulk NBs have a diameter of less than 1 μm [15].

The NBs have intrigued the scientific community on account of their longevity, that contradicts classical thermodynamics. Specifically, due to high Laplace pressure inside the NBs, an estimate by Epstein and Plesset predicts that a bubble of radius R ~ 100 nm and of gas diffusion coefficient D ~ $1x10^{-9}$ m^2/s should dissolve within a diffusion timescale of $\tau_{dis} \sim R^2/D \sim 10$ μs [13],[14]. However, contrary to the theory, bulk NBs have been reported to last weeks or even months [8],[9],[10],[11],[12].

In this chapter, a brief overview of surface and bulk NBs will be given, focusing on their stability mechanisms, production methods, potential applications and characterization methods.

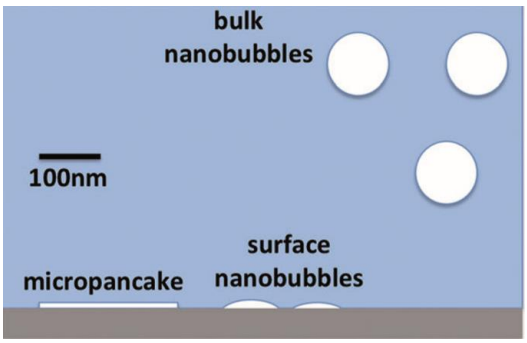

Figure 1.1. *The three types of NBs observed in the literature.*

Adapted from Seddon, J., Lohse, D., Ducker, W. and Craig, V. (2012). A Deliberation on Nanobubbles at Surfaces and in Bulk. *ChemPhysChem*, 13(8), pp.2179-2187.

Surface NBs were first speculated to exist in 1994, when Parker et al. observed step-wise features in atomic force curves between two hydrophobic surfaces (as seen in Fig. 1.2) [4], which led to the first atomic force microscopy (AFM) images by Lou et al. [5] and Ishida et al. [6] in 2000 (as seen in Fig. 1.3). Bulk NBs were first reported in 1981 by Johnson and Cooke and they were measured to be stable for periods longer than 22 hours [15]. Some significant publications in the field of NBs are presented in Fig. 1.4.

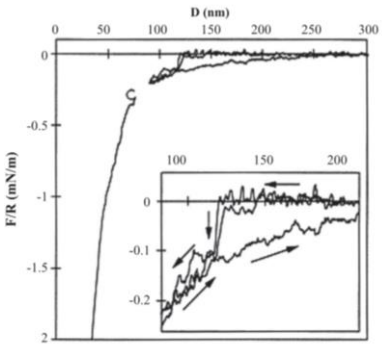

Figure 1.2. *Stepwise force discontinuity in the force vs distance curve from measurements between two hydrophobic surfaces.*

Adapted from Parker, J., Claesson, P. and Attard, P. (1994). Bubbles, cavities, and the long-ranged attraction between hydrophobic surfaces. The Journal of Physical Chemistry, *98(34), pp.8468-8480.*

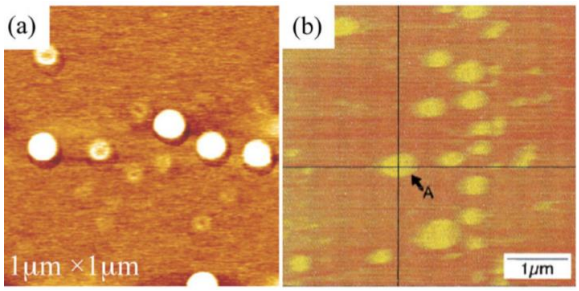

Figure 1.3. *The first AFM images of surface NBs in 2000 by Lou et al. (a) and Ishida et al. (b).*

Adapted from Lohse, D. and Zhang, X. (2015). Surface nanobubbles and nanodroplets. *Reviews of Modern Physics*, 87(3), pp.981-1035.

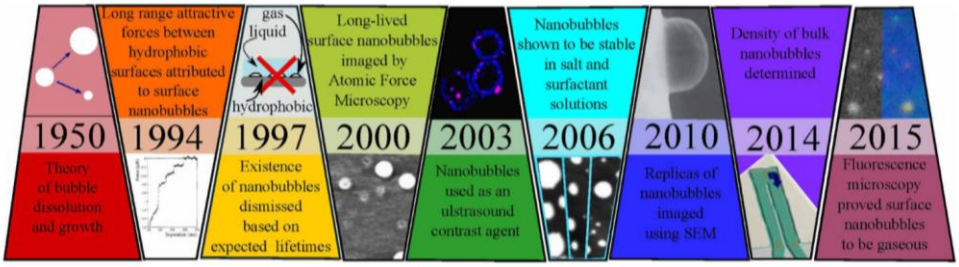

Figure 1.4. *Notable publications concerning bulk and surface NBs. Contributions to the field of bulk NB are highlighted in bold.* ***1950: The Epstein-Plesset theory is used to assess the lifetime of a single bubble as a function of the radius of the bubble and saturation. According to the theory, NBs should dissolve in microseconds [13].*** *1994: Surface NBs proposed to account for long-range attractive forces that were measured between hydrophobic surfaces [4]. 1997: The role of surface NBs in the long-range attractive forces between hydrophobic surfaces claimed earlier [4] was dismissed by the short-expected lifetimes calculated [14]. 2000: The first images of surface NBs using atomic force microscopy (AFM) were published [5],[6].* ***2003: The application of NBs as ultrasound contrast agents was reported [16].*** *2006: The effect of surfactants and salt on the size and shape of NBs was found to be negligible, thus indicating that the stabilization of surface NBs was unlikely to be due to contaminants [17].* ***2010: Replicas of bulk NBs were imaged with scanning electron microscopy [8]. 2014: The relative mass density of nanoparticles compared to the solvent was measured by a microresonator, indicating that the particles are gaseous [18].*** *2015: Surface NBs found to be gaseous using fluorescence microscopy coincided with other imaging techniques [19].*

Adapted from: Alheshibri, M., Qian, J., Jehannin, M. and Craig, V. (2016). A History of Nanobubbles. Langmuir, *32(43), pp.11086-11100.*

2. Stability of NBs

2.1 Stability of surface NBs

Surface NBs have a typical height, h, of a few tens of nanometres, and a width, a, up to a few hundred nanometres. Their typical radii of curvature, R, are $(a^2+h^2)/2h \sim 100$ nm-1 μm, and their Laplace pressure, if γ is the surface tension of pure water, is $p= p_o + 2\gamma/R \sim 2$-10 atm, where p_o is the ambient pressure [22],[23],[24]. Therefore, they are expected to dissolve in a time period of $\tau \sim R^2/D \sim 1$-10 μs, where D is the diffusion constant [22]. Nevertheless, surface NBs can exist for days, contrary to the classical prediction, and therefore they are considered stable [1].

Two main possible explanations have been introduced. The first one, by Drucker, states that each bubble is coated with a trapped layer of contaminant, that provides a barrier to diffusion and decreases the surface tension [20]. The second theory, by Brenner and Lohse, states that gas escapes through the spherical cap of the NB due to the high Laplace pressure, but this outflux is balanced by an influx at the three-phase line (where solid, gas, and liquid meet), so that each surface NB exists in a dynamic equilibrium [21]. Both theories have advantages and disadvantages, which are described in sections 2.1.1 and 2.1.2.

2.1.1 Contamination theory

According to this theory, when sufficient contaminants accumulate on the liquid/gas interface of a surface NB, then two effects take place, a decrease in surface tension as well as the formation of a barrier to diffusion [20]. By the adsorption of contaminants on the liquid/gas surface, the reduction of surface tension is achieved [20]. In particular, if contaminants (e.g. polymers or insoluble polymers) become pinned on the bubble, then as dissolution of the gaseous content of the bubble takes place, the bubble shrinks in volume and the surface density of contamination increases at the gas/liquid interface. As the density of contamination increases, the surface tension further decreases and may become zero [22]. In that case, the pressure difference across the interface becomes zero and therefore the diffusive driving force for dissolution also becomes zero. For this reason, the dissolution of NBs would only occur due to entropic favourability of mixing, which may take a long time [22]. Moreover, the insoluble film of contaminants acts as a diffusion barrier, slowing diffusion that results from pressure differences [20].

This theory explains the stability of NBs, by providing a barrier to diffusion and diminishing the driving force for diffusion. Nevertheless, there are disadvantages to this theory. Firstly, the concept of "universal" contamination is questioned, because surface NBs are found in different systems and are generated with a range of techniques and setups. However, even purified water is thought to contain enough contaminants to alter the hydrodynamic boundary condition of a NB [25]. Secondly, the effect of a diffusion barrier would be diminished due to thermal fluctuations, that would result in the creation of pores on the contaminant barrier, which would then lead to a general outflux of gas with the passage of time [22]. However, the resulting outflux of gas contrasts the stability of surface NBs. Lastly, Das et al. found that surface tension is reduced by ionic and non-ionic contaminants, but this is not sufficient for the prevention of the outflux of gas due to diffusion [26].

2.1.2 Dynamic Equilibrium Model

According to this model, the diffusive outflux through the spherical cap is replenished with a gaseous influx at the three-phase line (where solid, gas, and liquid meet, solid being a hydrophobic material) [21]. There is an equilibrium size for surface NBs, and therefore oversized bubbles shrink

while undersized bubbles grow in order to reach it [21]. The model explains therefore both stability of surface NBs and preferred sizes of NBs that have been found experimentally [22].

Nevertheless, there are setbacks to this theory. Firstly, if both an influx and an outflux of gas occurs, the outfluxing gas should move back inside the NB to prolong its lifetime. Therefore, there must be a recirculatory stream where the gas flows and energy input is required [22]. Secondly, no stable point for the influx and outflux of gas should exist [22]. Thirdly, Brenner and Lohse [21] created the "gas enrichment" concept based on a numerical paper [27] which assumed that gas flux towards the wall (substrate) was not influenced by the diffusive flux away from the wall, due to the presence of the NB [22]. Lastly, as this model is based on the fact that the existence of the NBs is on hydrophobic surfaces, it does not explain the existence of NBs on hydrophilic surfaces. However, surface NBs have been found on all substrates investigated till now, with macroscopic contact angles ranging from 15° (mica) to 108° (hydrophobized silicon) [22].

2.2 Stability of bulk NBs

The longevity of bulk NBs opposes classical thermodynamics, and therefore the phenomenon has stimulated the interest and curiosity of the scientific community. Specifically, according to Young-Laplace, the internal pressure (inside of the NB) is notably increased with the decrease of the diameter [28]:

$$\Delta P = \frac{2\gamma}{R} \quad (2.1),$$

where $\Delta P = P_{vap} - P_{liq}$ is the difference in pressure between the one inside the nanobubble (vapor state), and the one outside (liquid state), and γ is the surface tension. The pressure estimated for a NB with diameter 100 nm in pure water according to eq. (2.1) is ~ 30 atm. For this reason, according to the Epstein and Plesset theory [13], the NB should have dissolved ~ 10 μs after its formation. Therefore, it would be anticipated that bubbles at nanoscale dissolve immediately, in the effects of bubble coalescence, bubble breakage or Ostwald ripening [3],[9]. However, contrary to the theory, bulk NBs have been reported to last weeks or even months [8]-[12]. The long-term stability of NBs is dependent on a number of factors, which are analyzed in this section.

2.2.1 Electrostatic double layer

The stability of bulk NBs is achieved by the existence of an electrical double layer [30]-[32]. The electrostatic double layer repulsion exists due to the negatively charged gas/liquid interface [3]. Specifically, in the 19th century, electrophoretic measurements concluded that at neutral pH water air bubbles bear a spontaneous negative surface charge, as the bubbles migrated towards the positive electrode [33]. The results of electrophoresis were further confirmed when McTaggart used a cylindrical rotating cell to offset the buoyancy of the bubbles. He speculated that the negative surface charge is due to the selective adsorption of hydroxide ions [34]. This speculation was then reinforced by measurements of the zeta potential in different pH values [29],[35]-[38]. Takahashi et al. measured a zeta potential of -100 mV at pH 10. The zeta potential then decreased to -35 mV with a decreased pH equal to 5.8. They also found an isoelectric point at pH 3-4 [38]. Moreover, the influence of an increased electrolyte concentration on the zeta potential was investigated. Creux et al. found that the zeta potential is reduced (becomes less negative) as the sodium halide salt concentration increases above 10^{-5} M due to double layer compression [29]. Furthermore, in the same study, the zeta potential increases (becomes more negative) with an increase of the

concentration of NaOH, suggesting specific adsorption of hydroxide at the gas/liquid interface of the bubble [29].

Due to the studies mentioned and similar ones, it is believed that an electrical double layer surrounds bulk NBs [39], [40]. This layer provides a repulsive force for the prevention of coalescence and interbubble aggregation of the stable NBs [41]. Particularly, strong adsorption of hydroxide ions is considered responsible for the negative charge. In order to satisfy electroneutrality, hydroxide is balanced by protons or salt on the diffuse layer [35].

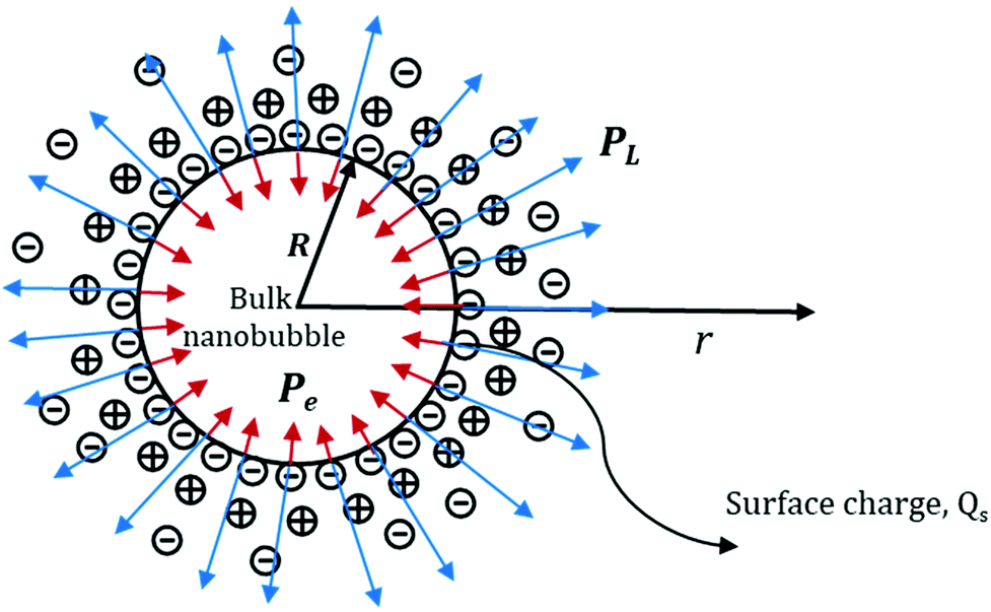

Figure 2.1. *Representation of the Laplace and electrostatic pressures influencing a bulk nanobubble.*

Adapted from Nirmalkar, N., Pacek, A. W., & Barigou, M. (2018). Interpreting the interfacial and colloidal stability of bulk nanobubbles. Soft Matter, 14(47), 9643–9656. doi: 10.1039/c8sm01949e

2.2.2 Negligible buoyancy force

For a spherical bubble of radius R at a no-slip boundary condition, the terminal rise velocity U_T is given by

$$U_T = \frac{2R^2 \Delta\rho g}{9\mu} \qquad (2.2),$$

where g is the acceleration due to gravity, Δρ is the difference in density between the bubble and the solution, and μ is the viscosity of the liquid. The no-slip terminal rise velocity for a NB with radius 50 nm is 2.7 nm s^{-1}, and for a NB of radius 500 nm is 272 nm s^{-1} [15]. Due to the very low values of the rise velocities, the effect of buoyancy is considered insignificant and negligible compared to Brownian movement [15].

2.2.3 Reduction of surface tension

As discussed in section 2.2, high calculated Laplace pressures contradict the longevity of NBs. Therefore, increase in stability of NBs can be achieved by a reduction of the Laplace pressure that according to eq. (2.1) can be achieved by a decrease of surface tension at the gas/water interface.

Such decrease can be achieved by the presence of impurities. Impurities can be a result of improper sample preparation, sloppy experimental procedures or organic impurities in the solvent employed [20],[43]-[46]. The theory by Drucker et al. presented in section 2.1.1 for surface NBs can be applied to bulk NBs as well. According to this theory, a layer of water insoluble organic contaminants coats the gas/water interface, therefore obstructing the diffusion of gases and decreasing surface tension [20],[42].

The reduction of surface tension could be also achieved by the existence of adsorbed ions at the gas/water interface. The presence of ions, due to thermal electrolytic dissociation, as well as carbonic acid anions could reduce the surface tension, and thus stabilize NBs [31],[47]-[51]. Bunkin et al. proposed a quantitative model according to which gas bubbles can be stabilized by adsorbed ions. These ions charge the surface of the bubble and are screened by a cloud of less adsorbing counter-ions [31],[51].

3. Production methods

3.1 Production of bulk NBs

Most commonly, NBs are produced via cavitation, a phenomenon in which sudden reduction of pressure in a homogenous liquid, below a critical value, results in a phase change [52]. Cavitation is classified into four categories: hydrodynamic, acoustic, particle and optic cavitation. Cavitation caused by pressure variations in a flowing liquid is called hydrodynamic cavitation whereas the cavitation caused by passage of ultrasonic waves is called acoustic cavitation. Hydrodynamic and acoustic cavitation are the phenomena through which NBs in the bulk solution are produced [53].

Hydrodynamic cavitation is applied mainly through Venturi tubes for the generation of NBs. In the Venturi-tube generator system, liquid and gas are passed through the Venturi tube simultaneously. When pressurized fluid enters the tubular part, flow velocity of the liquid increases in the cylindrical throat while pressure becomes lower in comparison with the inlet section. This process results in cavitation [3]. By applying this method, Ahmadi et al. produced NBs with diameter 130-545 nm [57]. Fan et al. also produced NBs but with considerably smaller diameters (<50 nm) [58]. Furthermore, Wu et al. applied batch high-intensity cavitation to produce NBs by a generator. The generated NBs had diameters smaller than 500 nm [59].

One method of applying acoustic cavitation to produce bulk NBs is sonication. Kim et al. applied sonication (70 W, 42 kHz) to produce bulk NBs directly in a cuvette, by placing an electrode coated by palladium in a DLS apparatus [54]. Oeffinger and Wheatley applied ultrasonication of a mixed surfactant solution with regular purging using octafluoropropane gas to generate NBs, with a mean diameter of 450-700 nm [56]. Cho et al. also applied ultrasonication (20 kHz) and found that the size of NBs increases with production time and US power. By this method NBs were produced with diameter greater than 700 nm [55].

Another method that has been applied for the generation of NBs is electrolysis. After applying electrolysis, Kikuchi et al. detected stable nanoparticles, characterized as NBs via dynamic light scattering (DLS) [60],[61],[62]. Ohgaki et al. generated NBs by injecting gas (Ar, CH_4 and N_2) in water [8]. Uchida et al. also produced NBs by injection of pure oxygen gas into water [63].

3.2 Production of surface NBs

Surface NBs can be produced by a solvent exchange, a temperature increase, as well as by photochemical, catalytic and electrochemical methods [1]. These methods are described in the following paragraphs.

Surface NBs can be produced as a result of supersaturation on hydrophobic surfaces via solvent exchange. In this case, the surface (substrate) is immersed in water, with a high level of dissolved gas (stage 1). Then, water is replaced by ethanol (stage 2) and subsequently ethanol is replaced by water (stage 3), as depicted in Fig. 3.1. Both water and ethanol are saturated or oversaturated with air or a specific gas. As gases present a higher solubility in ethanol than in water, a transient gas oversaturation is locally created when ethanol (which is a good solvent) is replaced by water (which is a poor solvent) [1],[64]. Therefore, there is an excess of gas near to the surface that leads to the nucleation of surface NBs. Also, instead of using ethanol as a solvent, other water miscible organic solvents such as methanol and isopropanol can be used [66].

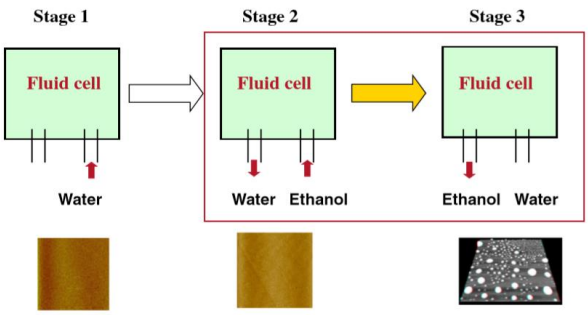

Figure 3.1. *Schematic drawings that depict the solvent exchange method. The substrate (e.g. HOPG) is initially exposed to water (stage 1) and characterized by AFM. Then, water is replaced by ethanol (stage 2) and the substrate is imaged again by AFM. For both stages, no NBs are imaged. Nucleation of surface NBs can occur from a subsequent replacement of ethanol with water (stage 3). In this case, surface NBs are visible with AFM.*

Adapted from Lohse, D. and Zhang, X. (2015). Surface nanobubbles and nanodroplets. *Reviews of Modern Physics*, 87(3), pp.981-1035.

Alternatively, to ethanol-water exchange, exchange of cold water with warm water has also been applied [17],[67]. In this method, NBs are generated by exchanging cold water (4 ^{o}C) with warm water (25-40 ^{o}C) [1]. Due to the fact that gas solubility is higher in cold water in comparison with warm water, oversaturation is achieved during the process. The advantage of this method is that no organic solvents are employed, and therefore the risk of contamination is avoided as no organic solvents are present (a risk that the exchange method of Fig. 3.1 presents).

Moreover, surface NBs can be produced by electrochemical reactions as well as photochemical and catalytic reactions. In particular, gas molecules can be generated through electrolysis at an electrode. Zhang et al. were the first to experimentally observe surface NBs produced by electrochemical reactions. They combined in situ tapping mode atomic force microscopy (AFM) with an electrochemical reaction cell in order to produce and image electrochemically produced surface NBs [68]. Furthermore, surface NBs are also produced by photochemical and catalytic reactions from generated gases. Paxton et al. generated oxygen NBs by the catalytic decomposition of H_2O_2 to H_2 and O_2 on a Pt surface [69]. In another study Shen et al. observed surface NBs on

surface-coated titanium dioxide in a methanol and water solution through a photocatalytic reaction [70].

4. Applications

4.1 Flotation

Flotation is a separation process with wide application in the mineral processing industry for the separation and recovery of valuable materials, such as minerals, phosphates and coal, from undesirable gangue. The process is also used in the recycling industry as well as the water-treatment industry. Due to the applied mechanisms of the process, a system is created, defined by three interfacial tensions: (1) the solid-liquid tension, (2) the gas-solid tension, and (3) the gas-liquid tension [72].

The froth floatation process has two basic parameters, the hydrophobicity of the surface as well as the coal and minerals particle size that influence the following important steps of the process: particle-bubble collision, adhesion and detachment. The process of flotation is based on the fact that the surface of the valuable mineral is hydrophobic, and the surface of gangue minerals is hydrophilic [73]. Air bubbles are generated in tanks, known as flotation cells, where the hydrophobic and hydrophilic particles are introduced. Hydrophobic particles collide and adhere to the bubbles, which are by nature hydrophobic. Then the bubble-hydrophobic particle aggregates are transported from the collection zone to the froth zone, where the froth is drained and enriched. Then they overflow from the cell top and are collected, whereas hydrophilic particles remain in the pulp and are discharged as tailings [74].

The enhancement of the mineral flotation process with NBs is supported by a number of studies, which claimed the following advantages:

1. The contact angles are increased by the presence of nanobubbles. Therefore, the probability of flotation is enhanced for phosphates and coal, i.e. the attachment and stability (reduction of detachment probability) between bubbles and particles [74],[75].
2. The presence of NBs can result in particle aggregation and the particles are therefore recovered easier due to increased collision probability [3].
3. The flotation recoveries of lower frother and collector dosages and at high kinetic flotation rate are enhanced by the presence of nanobubbles [75],[76].

Fan et al. also concluded that by utilizing NBs in the flotation process, the phosphate and coal froth flotation recovery is improved due to the wider particle size range for flotation, and the reduced probability of detachment [77].

4.2 Water treatment

In recent years, nanobubbles have attracted growing attention due to their potential applications in the water treatment. Nanobubbles along with microbubbles (MBs) have been applied to increase the detoxification efficiency of water [78], by this way improving the efficiency of chemical treatment of water. Water pretreatment targets the reduction of chemical, biological and physical loads with the aim of increasing the treated water quality and reducing the running costs. In this

frame, air MBs and NBs can be applied as a pretreatment means in order to downsize the wastewater treatment facilities and improve the quality of product water [78],[79].

Moreover, Uchida et al. demonstrated that bulk NBs adsorb impurities in solutions effectively and concentrate them on their surface. As a result, impurities are separated from solutions [63]. Xiao et al. studied the effect of NBs on phosphine recovery in artificial wastewater. They suggested that the roles of bulk NBs in precipitation and flotation are different. In particular, NBs inhibit the precipitation of styryl phosphoric acid (SPA) – Pb particles with small size (~ 1 nm), whereas when the size of the SPA-Pb is large (~ 2 μm), NBs promote the flotation of precipitated SPA-Pb particles. Furthermore, when NBs are added into precipitated SPA-Pb particles, the efficiency of flotation recovery can be enhanced up to 90% [71].

Furthermore, studies have focused on the application of NBs for the removal of organic contaminants. MBs and NBs have been utilized for the removal of a variety of organic pollutants in water and aqueous solutions, such as alachlor [80], p-nitrophenol [81] and rhodamine B [82]. Another study suggests that ozone MBs and NBs lead to faster disinfection kinetics in the case of Escherichia coli, which causes smaller doses of ozone and a reduced reactor size in comparison with conventional ozone disinfection [83]. Furthermore, the efficiency of the deactivation of E. coli has been increased through hydrodynamic cavitation [84]. Also, it has been proved that ozone NBs prevent pathogen growth in bathing pool assemblies [85].

4.3 Surface cleaning

Nanobubbles have been studied for the prevention of fouling and the promotion of antifouling on surfaces. Specifically, Wu et al. [86], have produced NBs electrochemically on a surface that remove pre-adsorbed proteins on the surface. The NBs have also been found to reduce the adsorption of proteins if they preexist on the surface, leading to prevention of fouling. Generally, NBs are applied both for the desorption (antifouling) or for the prevention of adsorption (fouling) of different components onto surfaces.

It has been shown that NBs can be utilized for the removal of organic pollutants from gold surfaces [88] and pyrolytic graphite [86],[87]. Moreover, NBs on a mica surface inhibit the adsorption of bovine serum albumin (BSA) [53]. Generally, the application of NBs constitutes a novel method for the cleaning of surfaces where fouling exists in biomedia, in the form of proteins. Specifically, the role of NBs is to act as antifouling agents, i.e. to present a mechanical barrier to the adsorption of material on the surface. For this reason, the parts of the surface that are covered by nanobubbles prevent exposure to contaminants [89]. As for the defouling mechanism it is illustrated in Fig. 4.1.

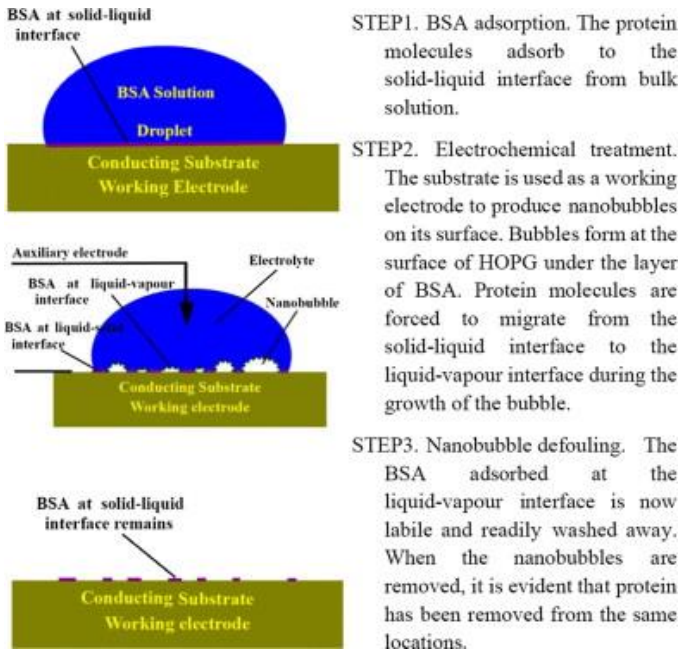

Figure 4.1. *Proposed mechanism for defouling of NBs. Nanobubbles are produced electrochemically on the surface and subsequently remove the fouling material from the surface. The substrate should be a conductor, such as stainless steel or HOPG.*

Adapted from Wu, Z., Chen, H., Dong, Y., Mao, H., Sun, J., Chen, S., … Hu, J. (2008). Cleaning using nanobubbles: Defouling by electrochemical generation of bubbles. Journal of Colloid and Interface Science, 328(1), 10–14. doi: 10.1016/j.jcis.2008.08.064

Moreover, NBs could potentially prevent fouling of ceramic membrane filtration processes due to their high mass transfer efficiency. Ghadimkhani et al. studied the impact of NBs on the defouling of such surfaces. First, they simulated fouling by applying an organic foulant, specifically humic acid, on the ceramic membrane. Then, defouling resulted after feeding air NBs on the membrane. The ceramic membrane was blogged by the NBs. It was suggested that hydroxyl radicals ($OH^{\cdot}$), that are generated after the MBs and NBs collapse, bond with organic foulants, such as humic acids, and decompose the organic matter [90].

4.4 Biological applications

Research in the field of biological processes has increased considerably in the last few years. Hyperoxia has been presented by Yoshida et al. as well as Owerkowicz et al. to promote the growth in plants [91] and animals [92] respectively. Liu et al. demonstrated that barley seeds dipped in water present higher germination rates, Moreover, Ushikubo et al. concluded that when barley coleoptile cells were floated in water after the production of oxygen MBs and NBs, cytoplasmic streaming rates inside the cells were accelerated [93].

Ebina et al. studied the influence of hyperoxia, by examining the growth of living organisms after oral administration of air and O_2 NBs [11]. During the study, plants of Brassica campestris were cultivated hydroponically for four weeks using air NBs. The impact on fish and mice was also examined. Specifically, rainbow trout and sweetfish were kept in water tanks that contained air NBs, and DBA1/J mice were bred normally with free drinking enhanced by O_2 NBs. In all cases, the presence of NBs in the water provided remarkable results compared with normal water. In the case of B. Campestris, the height (16.7 cm with normal water, 19.1 cm with NBs), length of leaves

(22.4 cm with normal water, 24.4 cm with NBs) and aerial fresh weight (20.3 g with normal water, 27.3 g with NBs) were increased. In the case of sweetfish, their beginning weight of 3 kg increased to 10.2 kg with NB-enriched water, and to 6.4 kg with normal water. As for rainbow trout, the total beginning weight of 50.0 kg increased to 148.0 kg with NB-enriched water, and to 129.5 kg with normal water. Finally, the length and weight of mice were also increased. The length and weight for NB-enhanced water was 17.0 cm and 23.5 g compared to 16.1 cm and 21.8 g in the case of normal water, respectively.

In a study by Hayakumo et al. [94], the cytotoxicity of NBs against human oral cells as well as the bactericidal activity of ozone NBs on periodontal pathogenic bacteria were examined. Specifically, the bactericidal activity was assessed by in vitro time-kill assays against Aggregatibacter actinomycetemcomitans and Porphyromonas gingivalis. It was found that in both cases of A. actinomycetemcomitans and P. gingivalis, the numbers of colony-forming units (CFUs)/mL, after exposure to ozone NBs for 0.5 min, dropped below detection limit (<10 CFU mL^{-1}). This result occurs from free-mediated oxidation reactions. However, after treatment with ozone NBs for 24 hours, minor viability decrease of oral tissue cells was presented, after being evaluated by the MTT assay. Therefore, it is concluded that ozone NBs could constitute a periodontal therapy by eliminating biofilms that contain pathogens.

Furthermore, studies concluded that NBs alter the cell function [95],[22]. Specifically, NBs provide a transport mechanism for gas delivery to a cell or membrane and therefore the membrane structure and the transmembrane proteins are affected respectively. Moreover, as hypoxia is considered critical for the progression of diseases like cancer, focus was placed on this research area. Specifically, Owen et al. [96] assessed the reduction of tumor hypoxia by an orally delivered suspension of submicrometer-sized oxygen NBs. Oxygen into NBs in comparison with oxygen directly dissolved in water presents higher concentrations and stability. The influence of both argon and oxygen nanobubbles was estimated. The hypoxia-inducible factor-1α (HIF1α) protein was measured in order to evaluate the ability of NBs' suspensions to impact tumor hypoxia. They concluded that only by oxygen NBs (and not argon NBs) a statistically notable reduction occurs in terms of the expression of vascular endothelial growth factor (VEGF) as well as the HIF1a.

In another study by Iijima et al. [97] the combination of radiation and enhanced water with oxygen NBs was studied in vitro in the case of cancer cells. EBC-1 lung cancer and MDA-MB-231 breast cancer were cultured with and without NBs. HIF1α and cell viability were assessed under normoxic and hypoxic conditions. There was a noteworthy suppression of HIF1α in the media enhanced with NBs in comparison with the normal culture media. Moreover, under hypoxic conditions, EBC-1 and MDA-MB-231 cells presented resistance to radiation, which was suppressed noteworthy with the use of oxygen NBs at a range of radiation doses.

5. Characterization methods of NBs

5.1 Bulk NBs

5.1.1 Nanoparticle tracking analysis (NTA)

This noninvasive technique is based on a laser light source to assess the concentration and size distribution of “nanoparticles”. It utilizes properties of Brownian motion and light scattering in order to analyze, in real time, the Brownian movement of the nanoparticles, in our case

nanobubbles, with results being bubble number density, mean bubble diameter and bubble size distribution [9]. A scattering spot emerges when the laser impinges on the particle. A high-speed camera is used in order to record the path of the scattered light spots. The camera captures a video file of Brownian motion of nanoparticles. Subsequently, the size of nanoparticles is evaluated by the Stokes-Einstein equation:

$$D_t = \frac{TK_B}{3\pi\eta d} \quad (5.1),$$

Where η, T and K_B are the liquid viscosity, the temperature and the Boltzmann constant, respectively, and D_t is the diffusion coefficient that is evaluated experimentally from the Brownian motions of the particles. Also, the concentration of particles can be assessed by dividing the volume of the field with the number of nanoparticles [98].

This technique can be applied for the real-time analysis of polydisperse systems with range in size from 10 to 2000 nm and particle number density from 10^6 to 10^9 particles/mL [99].

5.1.2 Dynamic Light Scattering (DLS)

With this noninvasive technique the bubble size distribution of the nanobubble suspensions is evaluated. Applications of the technique involve the characterization of particles, emulsions or molecules that have been dissolved or dispersed in a liquid. A laser light is scattered at different intensities due to the Brownian motion of particles/molecules in suspension. From the intensity fluctuations of the laser beam, the velocity of Brownian motion is calculated, and with use of eq. (5.1) the particle size. Counter to the NTA method, DLS does not calculate the bubble number density [9].

The DLS technique is applied for particle analysis for a size range of 0.3 nm to 10 μm and for a concentration range of 10^8 to 10^{12} particles/mL [100]. Nirmalkar et al. [9], and Filipe et al. [100] that studied bulk nanobubbles and standard latex nanoparticle suspensions respectively, identified that NTA provides better results in comparison with DLS. This is because DLS tracks the intensity of scattered light, and NTA tracks the Brownian motion of nanobubbles. Larger bubbles will scatter more light and therefore will tend to mask the light scattered by the smaller bubbles in the case of DLS, and for this reason it is stated that NTA constitutes a more accurate technique [9].

5.1.3 Zeta potential

The zeta potential is a crucial parameter in identifying the interaction energy between particles and for this reason the long-term stability of colloid suspension systems [101]. In the case that all suspended particles present a high zeta potential (positive or negative), then the suspension or dispersion will resist agglomeration. Regarding NBs, zeta potential has negative values, which is explained by the excess of OH^- ions at the gas-water interface, in pure water [3]. Many authors studied the parameters on the zeta potential in the case of air bubbles and have found that the pH of the medium, the surfactant type and concentration, and the kind of gas that is introduced in the bubbles play crucial roles [12],[41][54].

5.1.4 Electron Microscopy

Uchida et al. [63],[103] applied the freeze-fracture method to observe oxygen micro- and nanobubbles (MNBs) in solutions by a transmission electron microscope (TEM). They generated O_2 MNBs after introducing pure O_2 gas into ultra-high purity water with an MNB generator. Subsequently, they prepared the replica sample by putting a small quantity of the solution on an Au-coated Cu sample holder and then performing rapid freezing by immersion into a liquid nitrogen bath. Afterwards, the frozen droplet was fractured under vacuum and low temperature to reduce the formation of artefacts. Finally, the replica film was prepared by evaporating carbon and platinum prior to the removal of the replica film from the ice body by melting. They imaged spherical and oval holes with diameters ranging from 10^{-6} to 10^{-7} m, as seen in Fig. 5.1, that were considered as MNBs. In Fig. 5.1, the smooth area is attributed to ice crystallite formed during quenching, whereas other objects (except MNBs) imaged are considered a result of the aggregation of a small number of impurities in the original solution or of the textures formed during ice crystal growth [63].

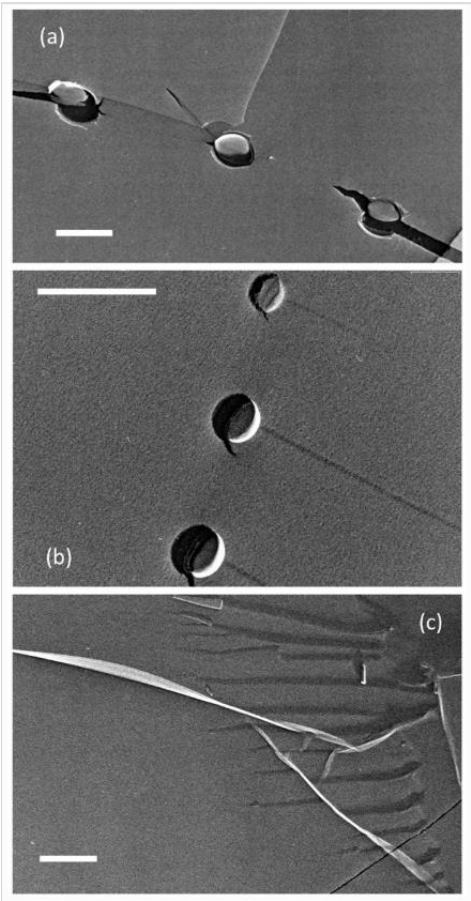

Figure 5.1. *TEM images of freeze-fractured replica of pure O_2 MNBs in pure water. Each scale bar indicates 500 nm. Spherical or oval NBs were imaged and were located in ice crystallites (smooth surface) or on their grain boundaries. These NBs had a diameter equal to (a) 500 nm or (b) 200 nm. (c) Replica sample of pure water without aeration, imaged as a control.*

Adapted from Uchida, T., Oshita, S., Ohmori, M., Tsuno, T., Soejima, K., Shinozaki, S., … Mitsuda, K. (2011). Transmission electron microscopic observations of nanobubbles and their capture of impurities in wastewater. Nanoscale Research Letters, 6(1). doi: 10.1186/1556-276x-6-295

In the same study, they imaged MNBs in a dilute salt solution (water containing 1% NaCl), prepared with the same freeze-fracture replica method, to assess the influence of solutes on MNB existence in solutions. They imaged MNBs and fine particles (with diameter less than 100 nm) on the grain boundary of ice crystallites, as seen in Fig. 5.2. The ice crystallites were considered a result of

quenching whereas the fine particles were considered as the agglomeration of condensed salts dissolved in the original solution due to the freeze-condensation mechanism [63].

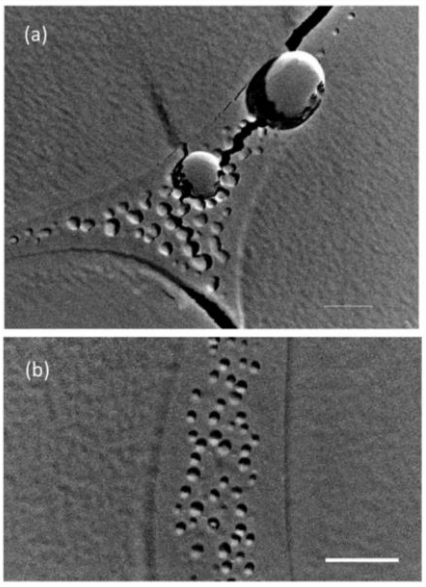

Figure 5.2. *TEM images of freeze-fractured replica of 1% NaCl solution containing O_2 MNBs. Scale bar indicates 200 nm. (a) MNBs (with diameters of 200 and 300 nm) and fine impurity particles (with diameters ranging from 10 to 60 nm) at the grain boundary of ice crystallites. A number of fine particles cover a small part around the MNBs. (b) Replica sample of 1% NaCl solution without MNBs imaged as control.*

Adapted from Uchida, T., Oshita, S., Ohmori, M., Tsuno, T., Soejima, K., Shinozaki, S., … Mitsuda, K. (2011). Transmission electron microscopic observations of nanobubbles and their capture of impurities in wastewater. Nanoscale Research Letters, 6(1). doi: 10.1186/1556-276x-6-295

Moreover, they imaged MNBs and macroscopic insoluble impurities in wastewater which was aerated to produce MNBs and then prepared with the freeze-fracture replica method. As seen in Fig. 5.3, MNBs adsorb many of the impurities that are observed in the form of fine particles [63].

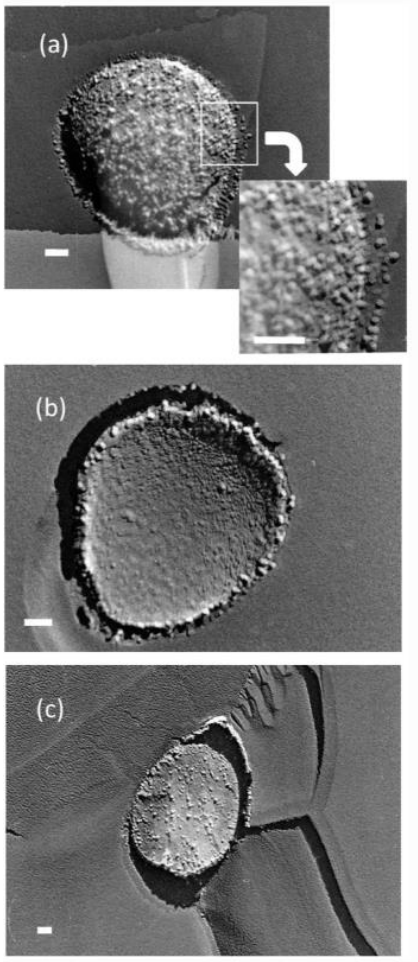

Figure 5.3. *TEM images of freeze-fractured replica of the wastewater containing O_2 MNBs. Every scale bar indicates 100 nm. (a,b) Imaged MNB 850 nm in diameter (observed on the centre ++of each image) contains fine particles, 20 nm in diameter. The extended image in (a) presents the bubble-solution boundary suggesting the process by which fine particles were attracted to the bubble surface. No fine particles were observed around the MNBs. (c) MNBs that contained fine particles were also found on the grain boundary between ice crystallites.*

Adapted from Uchida, T., Oshita, S., Ohmori, M., Tsuno, T., Soejima, K., Shinozaki, S., … Mitsuda, K. (2011). Transmission electron microscopic observations of nanobubbles and their capture of impurities in wastewater. Nanoscale Research Letters, 6(1). doi: 10.1186/1556-276x-6-295

Ohgaki et al. [8], measured the size of NBs by creating a replica film to observe by using scanning electron microscopy (SEM). They generated methane, nitrogen and argon NBs in an aqueous solution by a zero-clearance rotary pump. Afterwards, they created a replica film for SEM observation. In particular, a small droplet of the aqueous solution was put into 2-methylbutane in liquid form in order to immediately freeze the internal and interfacial structure of NBs. The quenched sample was then transferred to liquid nitrogen and was placed in a sample holder. Then, the sample was cleaved and coated in order to create a replica of the surface. Then, the replica was visualized with SEM. Methane, nitrogen and argon NBs, all of which had an average radius of 50 nm were visible, as seen in Fig. 5.4.

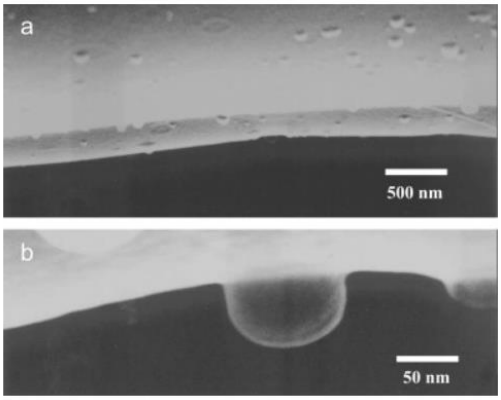

Figure 5.4. *(a) SEM image of nitrogen NBs located in an aqueous solution (b) and a magnified image of a nitrogen bubble (50 nm in radius). The sample was prepared in the form of a replica film and the observation was performed by means of a SEM of field emission type.*

Ohgaki, K., Khanh, N. Q., Joden, Y., Tsuji, A., & Nakagawa, T. (2010). Physicochemical approach to nanobubble solutions. Chemical Engineering Science, 65(3), 1296–1300. doi: 10.1016/j.ces.2009.10.003

However, freeze-fracture replicas can affect the sample morphology due to the preferential fracture plane [108], that can lead to morphological changes [123],[124], displacement of materials [125], and vesicle fusion in biological samples [126]. On the contrary, electron microscopy (EM) in cryogenic conditions (cryo-TEM & cryo-SEM) enables high-resolution and preservation of the morphology of the sample, as the sample is rapidly frozen and therefore can be imaged in a fully hydrated state [127],[128]. Furthermore, freezing minimizes the radiation damage of samples due to electron irradiation [128].

Usukura et al. [110], developed a cryo-EM facility to obtain simultaneously SEM and STEM images. They observed NBs (50-100 nm) in water, by pouring water into holes of a QUANTIFOIL membrane and instantly freezing the sample. Observed NBs can be seen in Fig. 5.5.

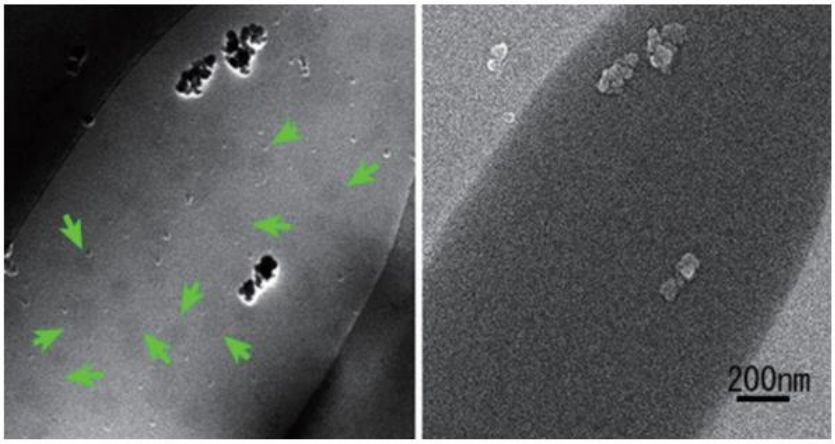

Figure 5.5. *STEM (left) and SEM (right) images obtained with developed cryo-EM facility. Nanobubbles in water observed (50-100 nm), are indicated with arrows and appear dark in STEM images. SEM and STEM was performed simultaneously. In order to image the sample, water was poured into holes in a QUANTIFOIL membrane and prior to imaging, rapid freezing was performed.*

Adapted from Usukura, J., Narita, A., Matsumoto, T., Usukura, E., Sunaoshi, T., Tamba, Y., Nagakubo, Y., Azuma, J., Mizuo, T., Nimura, K., Osumi, M., Tamochi, R., Ose, Y. (2018). Cryo-electron Microscope Developed for Simultaneous STEM, SEM Imaging and Its Application. Technical magazine of Electron Microscope and Analytical Instruments

Li et al. [109], generated N_2 NBs by a chemical reaction between two solutions in an assembly of two TEM grids coated with continuous carbon films. Excess solution was removed with filter paper after 1 min. The two-grid assembly was then put into liquid ethane, which was then cooled by liquid nitrogen. The samples were stored in liquid nitrogen until they were observed with cryo-EM.

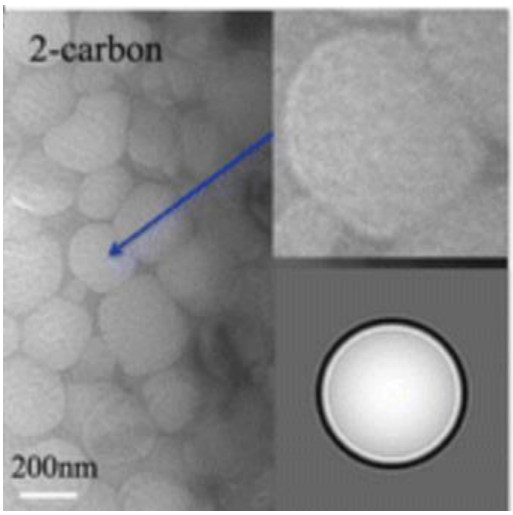

Figure 5.6. *Cryo-EM image that presents reaction solutions between two TEM grids coated with continuous carbon films. N_2 NBs were observed, and one of them (that is indicated with an arrow) is magnified in the upper inset. The lower inset presents a simulated bubble with a diameter of 50 nm.*

Adapted from Li, M., Tonggu, L., Zhan, X., Mega, T. and Wang, L. (2016). Cryo-EM Visualization of Nanobubbles in Aqueous Solutions. Langmuir, 32(43), pp.11111-11115.

NBs have also been visualized by cryo-EM in biological applications. Hernandez et al. [111] identified non-crosslinked and crosslinked NBs with perfluorocarbon gas cores, using cryo-EM. In particular, the NBs were put into QUANTIFOIL holy carbon EM grids. They were then rapidly frozen in a cryogen and imaged with TEM. They found that both types of NBs had spherical shape and diameters ranging from 100 to 500 nm.

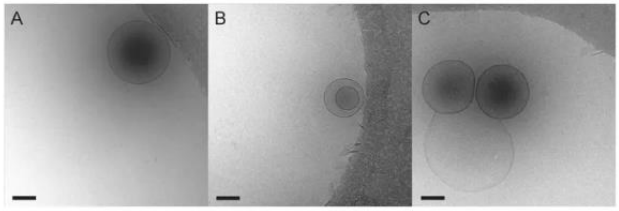

Figure 5.7. *Cryo-EM images of CL NBs. (A) A single CL NB beside the carbon support layer of the EM grid (upper right corner). (B) A larger NB encapsulating a smaller NB. (C) Two NBs interacting with a larger malformed NB. Scale bars indicate 100 nm.*

Adapted from Hernandez, C., Gulati, S., Fioravanti, G., Stewart, P. and Exner, A. (2017). Cryo-EM Visualization of Lipid and Polymer-Stabilized Perfluorocarbon Gas Nanobubbles - A Step Towards Nanobubble Mediated Drug Delivery. Scientific Reports, 7(1).

In another study, Leon et al. [112] also applied cryo-EM by imaging Propylene glycol-Glycerol-Phospholipids (PG-Gly-PL) NBs that have a dense C_3F_8 gas core. They washed the PG-Gly-PL NBs with phosphate-buffered saline, and they were imaged by cryo-TEM after they had been applied to QUANTIFOIL holey carbon EM grids.

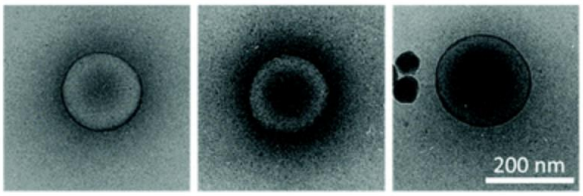

Figure 5.8. *Cryo-EM images with PG-Gly-PL NBs. They have a dense C_3F_8 gas core.*

Adapted from De Leon, A., Perera, R., Hernandez, C., Cooley, M., Jung, O., Jeganathan, S., Abenojar, E., Fishbein, G., Sojahrood, A., Emerson, C., Stewart, P., Kolios, M. and Exner, A. (2019). Contrast enhanced ultrasound imaging by nature-inspired ultrastable echogenic nanobubbles. Nanoscale, 11(33), pp.15647-15658.

5.1.5 Other techniques

In order to evaluate the existence and nature of NBs different techniques have been also applied. Ke et al. applied X-Ray fluorescence absorption near the Kr L-edge in a system containing Kr NBs, to evaluate their existence. It was found that samples measured by X-Ray fluorescence presented a decrease of Kr adsorption with the deposited time which agrees with the decreased concentration of bulk NBs measured by the NTA, proving therefore that gaseous cavities in the form of bulk NBs are present [98].

In a different study by Oh et al., ATR-FTIR measurements were applied to evaluate the existence of CO_2 bulk NBs in water. With IR spectroscopy the phase state of the CO_2 molecules was evaluated. It was found that the position and shape of the band matched the gaseous CO_2 spectrum, thus demonstrating that the generated bulk NBs were filled with CO_2 molecules [114].

Nirmalkar et al. assessed the nature of the bulk suspensions. To evaluate if the suspensions are truly bulk NBs, and not solid nanoparticles or nanodroplets that have contaminated the samples. They conducted freeze-thaw experiments, and after thawing, the suspensions reduced dramatically, therefore indicating that the nano-entities are bulk NBs and cannot be solid nanoparticles or nanodroplets [113].

5.2 Surface NBs

For the assessment of surface NBs, a range of alternative methods can be applied. Most commonly used are the techniques of atomic force microscopy (AFM) and scanning electron microscopy (SEM) by which an image of the surface NBs is created, and the shape and size of the NBs can be observed and evaluated [3],[122].

Moreover, by applying MEMS technology it is possible to fabricate a nano liquid cell, where it is possible to assess the nucleation, increase/decrease of the size of NBs, and their disappearance using transmission electron microscopy (TEM) and scanning transmission electron microscopy (STEM). This technique known as liquid cell electron microscopy (LCEM) [105] has been applied to several applications [102],[104],[105],[106],[107]. White et al. [104], used the technique to image the formation of a single NB initiated due to ingestion of heat near a platinum nanowire, after the application of a voltage pulse (as seen in Fig. 5.9).

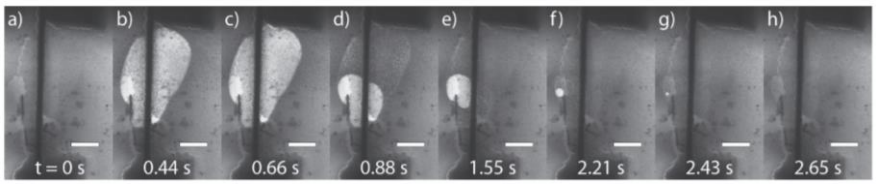

Figure 5.9. *STEM images presented in a time series that depict the nucleation and collapse of a NB. (a) A 0.5 V, 1 mA pulse lasting 740 ms is initiated on the nanowire. The nanowire is covered in water. (b) A NB appears and (c) grows, as the input electrical power is maintained. After the pulse ends, images (d)-(g) show the collapse of the NB. The dark strip observed, spanning each image from top to bottom, is the nanowire. The scale bar indicates 1 μm.*

Adapted from White, E., Mecklenburg, M., Singer, S., Aloni, S. and Regan, B. (2011). Imaging Nanobubbles in Water with Scanning Transmission Electron Microscopy. Applied Physics Express, 4(5), p.055201.

Other methods, namely attenuated total reflection infrared spectroscopy (ATR-FTIR) [115],[116], X-Ray scattering (SAXS) [119], neutron reflectivity [117],[118] and attenuated total reflection infrared spectroscopy [115], provide indirect assessment through the alteration in the physicochemical properties of a system. Characterization of the NB nucleation process has been achieved by using transmission electron microscopy in situ [102],[120], a technique that provides highly accurate temporal and spatial resolution. Moreover, quartz crystal microbalance (QCM) can be applied for the quantitative assessment of the adsorption of the crystal surface. Bubble nucleation can also be detected with electrochemical QCM as proposed by Carr et al [121].

6. Future of NBs

NBs unique physicochemical properties can be used in a variety of applications, from flotation to drug delivery. NBs improve already existing processes, yet the mechanisms behind their existence are not fully understood. Their stability is a paradox to classical thermodynamics, and a generally accepted model behind their longevity does not exist. Additional research is needed on the production of NBs and their identification methods, in order to standardize these procedures. Production methods should also target the applications where large concentrations of NBs are needed. Recently cryo-EM techniques have given the opportunity to obtain images of NBs and better understand their morphology, which could provide further information on their stability and the mechanisms behind their long-term existence. Having a better understanding of their nature could subsequently help us acknowledge their influence on each process they are applied to, and further improve the already-existing processes.

Chapter 2: Cryo-SEM imaging

1. Introduction to cryo-SEM

When imaging samples with electron microscopy (EM), cryogenic conditions are necessary in order to observe a specimen in its 'natural' hydrated state [134]. Cryogenic conditions are applied for aqueous and nonaqueous systems, like emulsions, suspensions, gels, biological specimens and even solids of high vapour pressure [129]. EM at cryogenic conditions (cryo-EM) does not require conventional preparation techniques, such as critical point drying or freeze-drying of the specimen [134]. Moreover, cryogenic conditions suppress motion on the supramolecular level that may have caused blurry images [129].

Another parameter is the freezing rate of the sample. If the cooling is achieved abruptly, it vitrifies the sample by preserving its nanostructure [130]. Rapid cooling of the specimen is achieved preferably by thermal fixation and not chemical fixation, as it does not change the structure of the sample [131].

Cryo-EM is performed either with scanning electron microscopy imaging (cryo-SEM) or transmission electron microscopy imaging (cryo-TEM). Cryo-TEM constitutes a direct-imaging method, for the observation of thin samples (100-300 nm thick), however larger objects are excluded [132].

On the other hand, cryo-SEM does not have this restriction. With cryo-SEM macro- micro- and nanostructures can be imaged [129]. In addition, a 3D topographical analysis of the sample's surface can be performed. The method was first suggested in 1970 [133], but only lately progress has been made due to the development of appropriate hardware [129].

Cryo-SEM is the method we incorporated for the imaging of the nanobubbles (NBs). A general description of a typical cryo-SEM can be seen in Fig. 1.1.

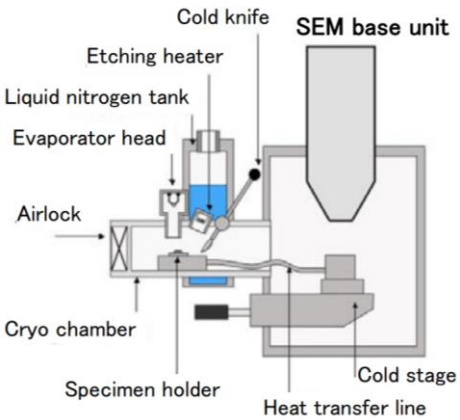

Figure 2.1 *Components of a cryo-SEM*

A cryo-SEM generally consists of a cryo chamber, where cleaving and coating of frozen specimens take place, and a cold stage for SEM imaging, as depicted in Fig. 1.1.

The cryo-SEM also incorporates a liquid nitrogen tank that cools both the cryo chamber and the cold stage. Part of the cryo chamber is a heater for etching (subliming) the ice formed on samples. A cold knife can also be present in order to cleave the sample and analyse its internal structure. Also, incorporated is a resistance heating vacuum evaporator that achieves the coating of the samples with metal by sputtering or with carbon by thermal evaporation [134],[135].

2. Procedure followed for the cryo-SEM imaging

The four different samples containing NBs were imaged with the cryo-SEM method. Before the imaging of the specimens, rapid thermal fixation (freezing) of the sample should occur by liquid nitrogen, in order to image the specimen in its 'hydrated' state [129],[135]. Water has the smallest cubic volume at 4°C. Therefore, as it freezes, it will expand, and can destroy the structure of the sample [135]. At the same time, when using liquid nitrogen, the freezing speed decreases due to boiling of the liquid nitrogen [135]. For this reason, rapid freezing is essential in order to preserve the morphology of the initial sample, in a manner that retains the structure of its contents.

To achieve this, in our lab, rapid freezing is performed with liquid nitrogen at high-pressure of 2000 bar. However, because we analysed NBs, it was uncertain whether NBs would be destroyed due to the high pressure applied. We therefore decided apart from performing preliminary freezing at high pressure, to implement freezing at ambient pressure as well. In the case of ambient pressure, due to the low freezing rate there is time for ice to potentially develop on the sample and influence its morphology. Despite this possibility, we deemed that such preliminary freezing could provide additional information regarding the morphology of the NBs.

The samples containing NBs were generated by hydrodynamic cavitation in the "Materials & Membranes for Environmental Separations Laboratory" of the Institute of Nanoscience and Nanotechnology at the NCSR "Demokritos" in Athens, Greece. The samples were imaged after both freezing at ambient pressure and high-pressure freezing and they are namely:

a) pure water with O_2 NBs
b) pure water with O_2 NBs blended with magnetic ionic liquid (MIL), 20% v/v
c) pure water with N_2 NBs
d) pure water with N_2 NBs blended with magnetic ionic liquid (MIL), 20% v/v

Figure 3.1. *The samples under analysis that contained NBs.*

Before the freezing of the samples containing MIL, the samples were mixed by a Vortex mixer. It is noted that the MIL, in samples b and d, is 1-Butyl-3-methylimidazolium tetrachloroferrate

($C_8H_{15}Cl_4FeN_2$). Samples a and c were blended with the MIL to create samples b and d, in order to assess how the MIL affects the dispersion of NBs observed after cryo-SEM imaging.

For the freezing at ambient pressure, a few droplets from every sample were sucked by a pipette and released into circular hollow cavities of an aluminium sample holder, indicated with arrows in Fig. 2.2. These cavities were then frozen by liquid nitrogen at atmospheric pressure.

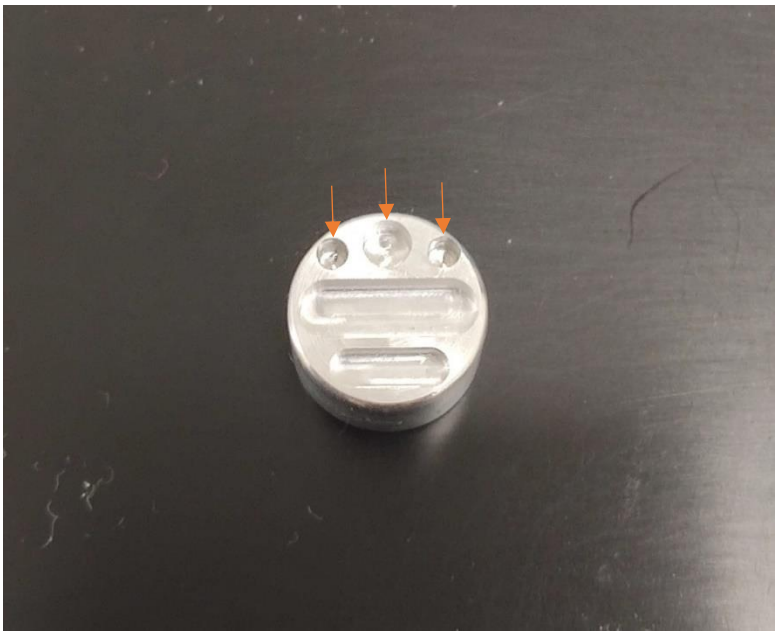

Figure 2.2. *Aluminium sample holder. The sample was inserted into the circular hollow cavities on the top of the disk, indicated with arrows.*

For the freezing at high pressure, a few drops were sucked by a pipette and released into a small round shallow aluminium receptacle. A second identical aluminium receptacle was placed on top of the one containing the liquid in order for the liquid to be sandwiched between the receptacles. The assembled sandwich was then plunged into the high-pressure freezing facility "LEICA EM HPM100" of our lab (see Fig. 2.3). Before the sandwich was plunged into the facility, liquid nitrogen had been placed into the facility and high-pressure of 2000 bar had been achieved. After the sample has been vitrified, the assembled sandwich is then transferred to a cryogen box containing liquid nitrogen, in order to be opened using tweezers in cryogenic temperatures, thus producing two fracture surfaces (each receptacle contains one fracture surface).

Figure 2.3. *The "LEICA EM HPM100" facility of the lab that achieves high-pressure freezing of specimens at 2000 bar.*

After the preliminary freezing is performed and the sample is at cryogenic conditions, it is loaded into the "PP3010T Cryo-SEM Preparation System", which is located in the cryo preparation chamber of the facility. The loading of the sample into the preparation system is applied after both freezing at ambient pressure and high pressure. In the case of high-pressure freezing, one of the receptacles is transported into the preparation system. The facility of the lab is named "Zeiss Crossbeam 550 FIB-SEM" (as seen in Fig. 2.5).

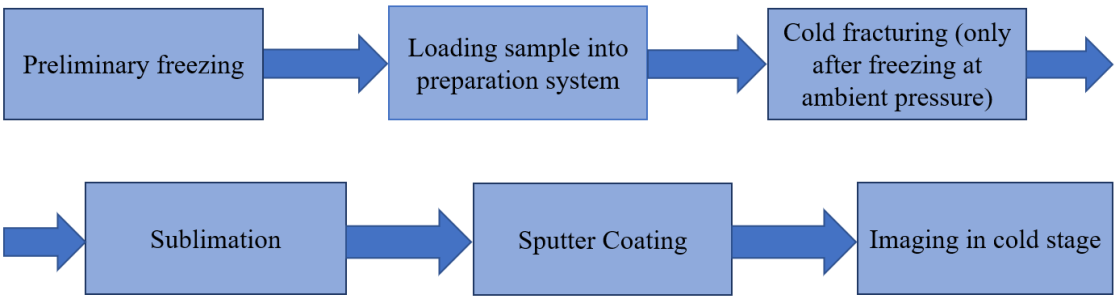

Figure 2.4. *Procedure followed for cryo-SEM imaging*

At the preparation system, cold fracturing of the sample after freezing at ambient pressure is performed in order to image its internal structure. This step is not applied after freezing at high pressure, as the fracture surface of the receptacle allows imaging of the internal structure without additional processing. For all samples (both after freezing at ambient pressure and high pressure) etching to remove the ice

(ice sublimation) is performed in a controlled manner for 10 min. Subsequently, each sample is sputter coated with platinum (10-12 nm) in order to create conductivity, which will then allow the SEM imaging, that is performed after the sample is transported to the cold stage of the cryo-SEM facility.

Figure 2.5. *The "Zeiss Crossbeam 550 FIB-SEM" facility of the lab*

At all stages of the preparation and imaging the specimen is maintained at a 'safe' temperature of typically lower than -140°C, in order to be observed in cryogenic conditions [134].

The images obtained for all four samples containing NBs are presented in section "3. Cryo-SEM results". Measurement of the diameters of the formations that are presented in section "3. Cryo-SEM results" was performed with the ImageJ software.

3. Cryo-SEM results

3.1 Pure water with O_2 NBs

In the case of vitrification of the sample of pure water with O_2 NBs at ambient pressure, formations attributed to NBs were imaged, as seen in Figs. 3.1-3.8.

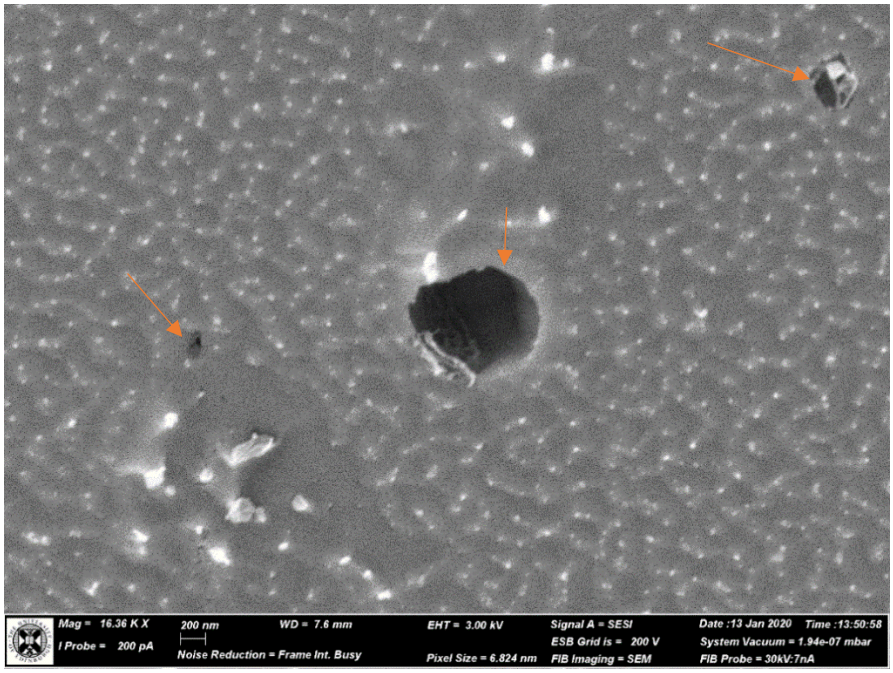

Figure 3.1. *Formations that could be attributed to O_2 NBs in pure water, indicated with arrows. The sample was frozen with liquid nitrogen at ambient pressure. The formation found at the center of the image has a measured diameter of 934 nm. The other two cavities (left and right) do not have a spherical shape and therefore no diameters were measured.*

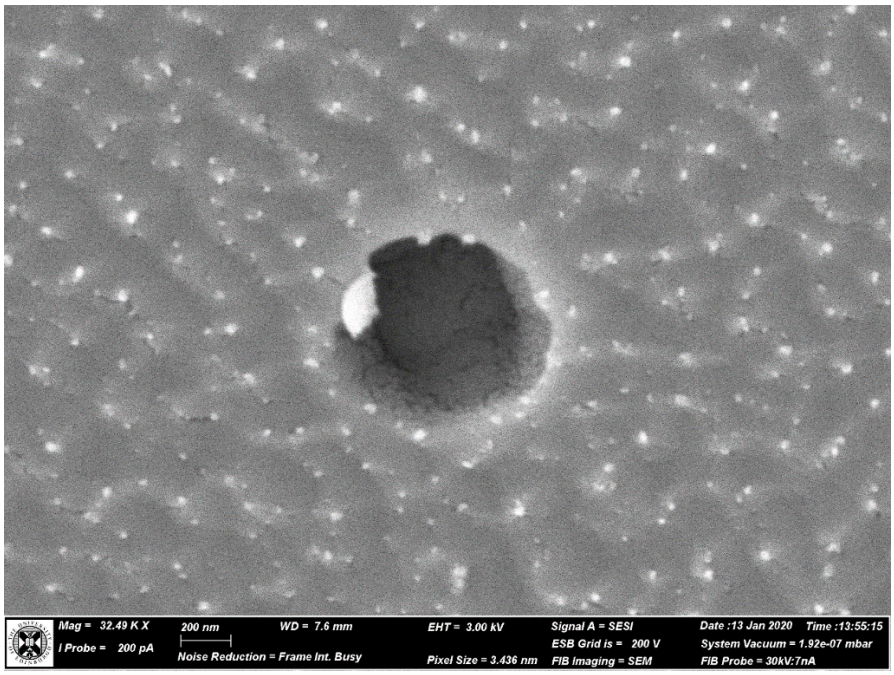

Figure 3.2. *Formation that could be attributed to an O_2 NB in pure water with a measured diameter of 741 nm. The sample was frozen with liquid nitrogen at ambient pressure.*

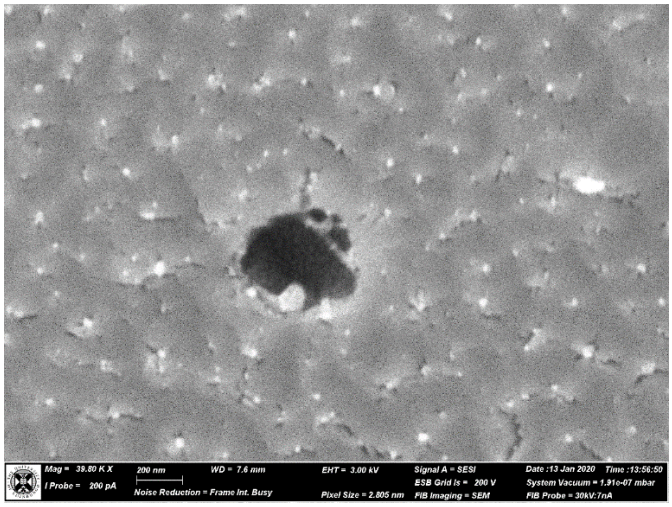

Figure 3.3. *Formation that could be attributed to an O_2 NB in pure water with a measured diameter of 560 nm. The sample was frozen with liquid nitrogen at ambient pressure.*

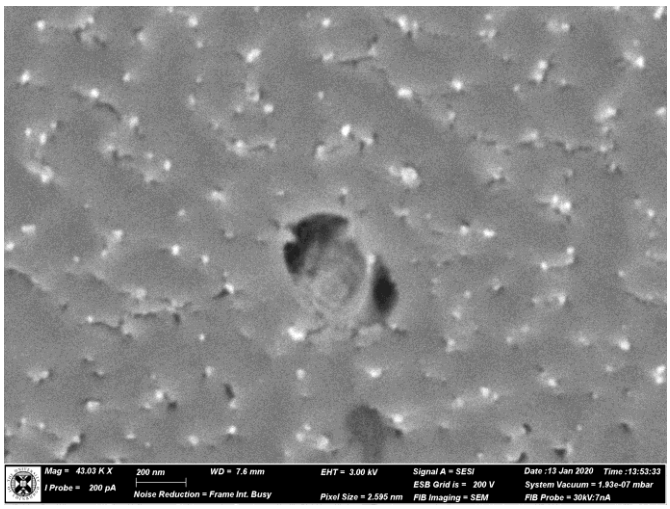

Figure 3.4. *Formation that could be attributed to an O_2 NB in pure water with a measured diameter of 512 nm. The sample was frozen with liquid nitrogen at ambient pressure.*

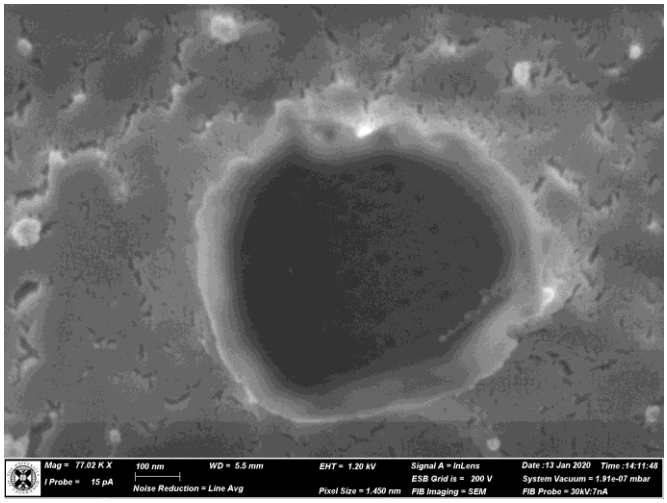

Figure 3.5. *Formation that could be attributed to an O_2 NB in pure water with a measured diameter of 774 nm. The sample was frozen with liquid nitrogen at ambient pressure.*

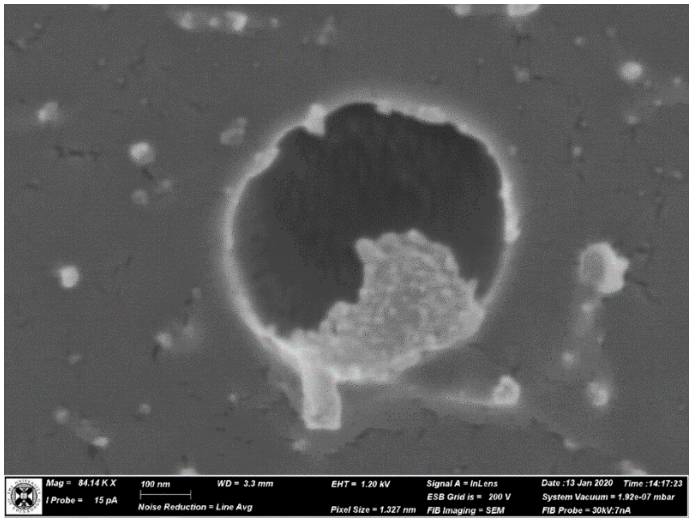

Figure 3.6. *Formation that could be attributed to an O_2 NB in pure water with a measured diameter of 553 nm. Ice has been developed on the surface of the formation. The sample was frozen with liquid nitrogen at ambient pressure.*

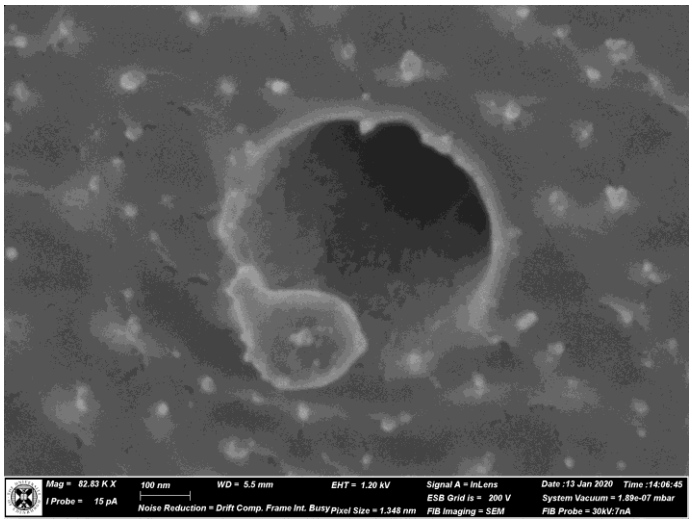

Figure 3.7. *Formation that could be attributed to an O_2 NB in pure water with a measured diameter of 514 nm. Ice has been developed on the surface of the formation. The sample was frozen with liquid nitrogen at ambient pressure.*

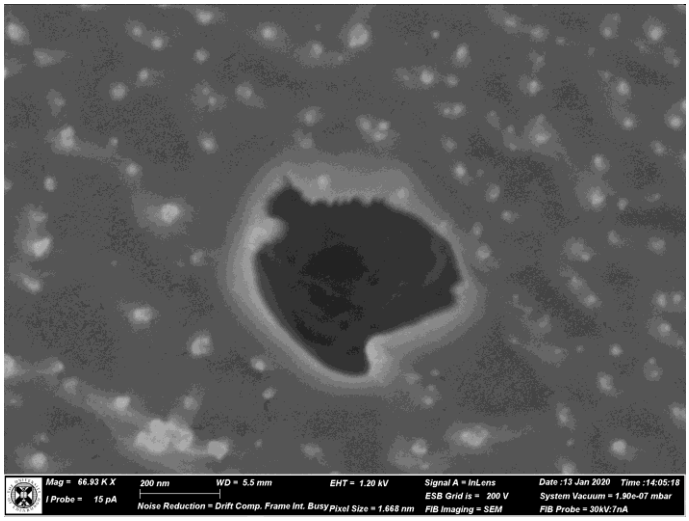

Figure 3.8. *Formation that could be attributed to an O_2 NB in pure water. The sample was frozen with liquid nitrogen at ambient pressure. The formation does not have a spherical shape and no diameter was measured in this case.*

A formation attributed to an O_2 microbubble has also been observed, as seen in Fig. 3.9.

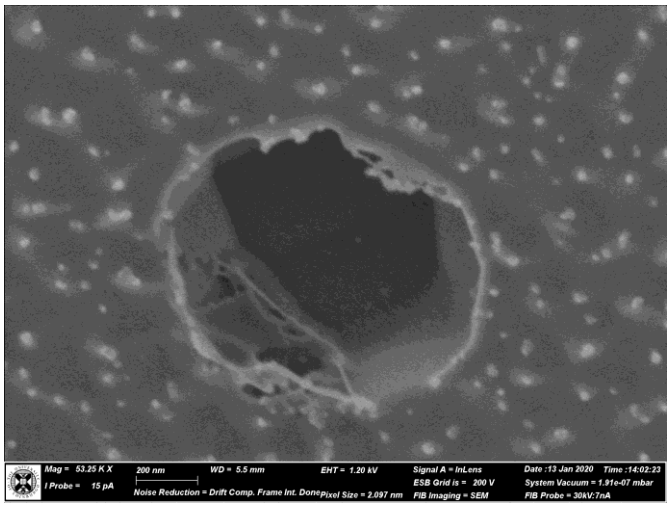

Figure 3.9. *Formation that could be attributed to an O_2 microbubble in pure water with measured diameter of 1084 nm. The sample was frozen with liquid nitrogen at ambient pressure.*

Across the surface of the sample white spots and bigger formations are observed, as seen in Figs. 3.10-3.11. These are considered as ice formations that have been developed during the preliminary freezing at ambient pressure.

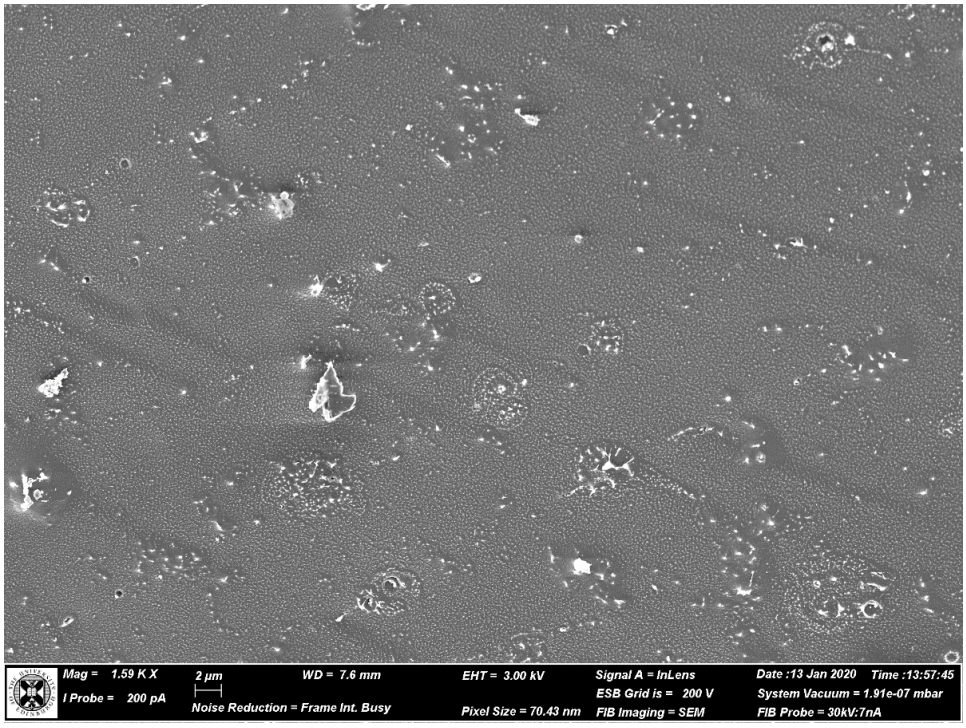

Figure 3.10. *Formations of ice in pure water with O_2 NBs. The sample was frozen with liquid nitrogen at ambient pressure.*

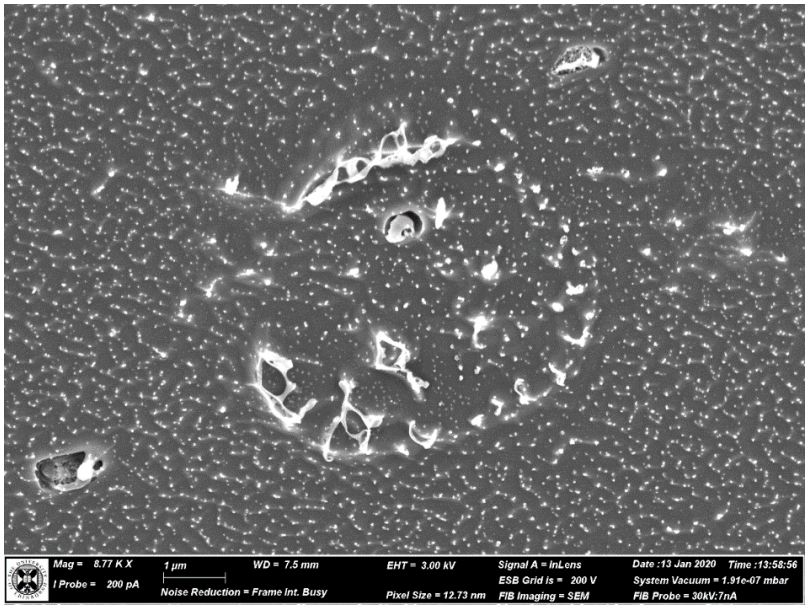

Figure 3.11. *Formations of ice in pure water. The sample was frozen with liquid nitrogen at ambient pressure.*

In the case of vitrification of the sample of pure water with O_2 NBs at high pressure (2000 bar), formations attributed to both microbubbles and NBs were imaged, as seen in Figs. 3.12–3.15 and Fig. 3.16, respectively.

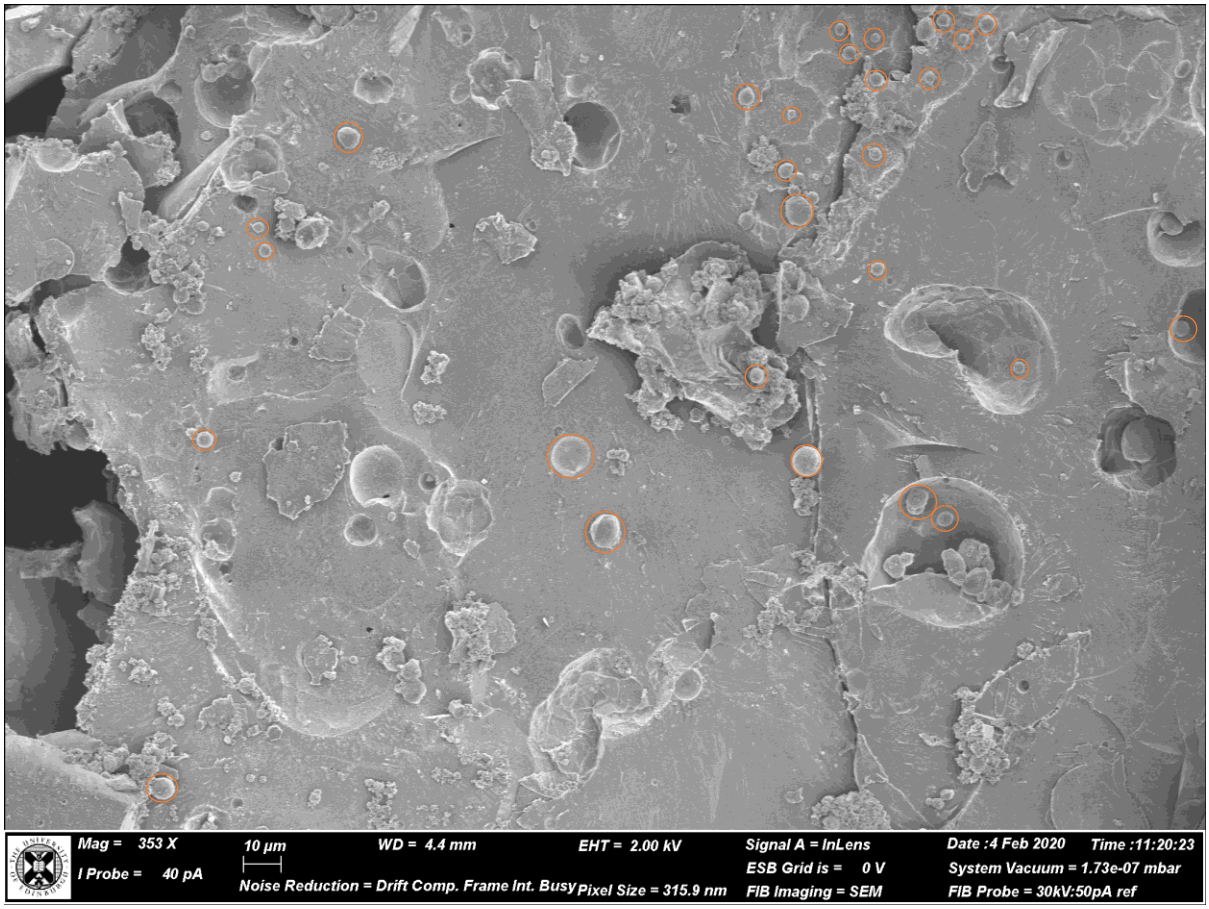

Figure 3.12. *Formations attributed to O_2 microbubbles in pure water, indicated with circles. The sample was frozen with liquid nitrogen at high pressure (2000 bar). Measured diameters of the indicated formations vary from 2.13 µm to 9.80 µm.*

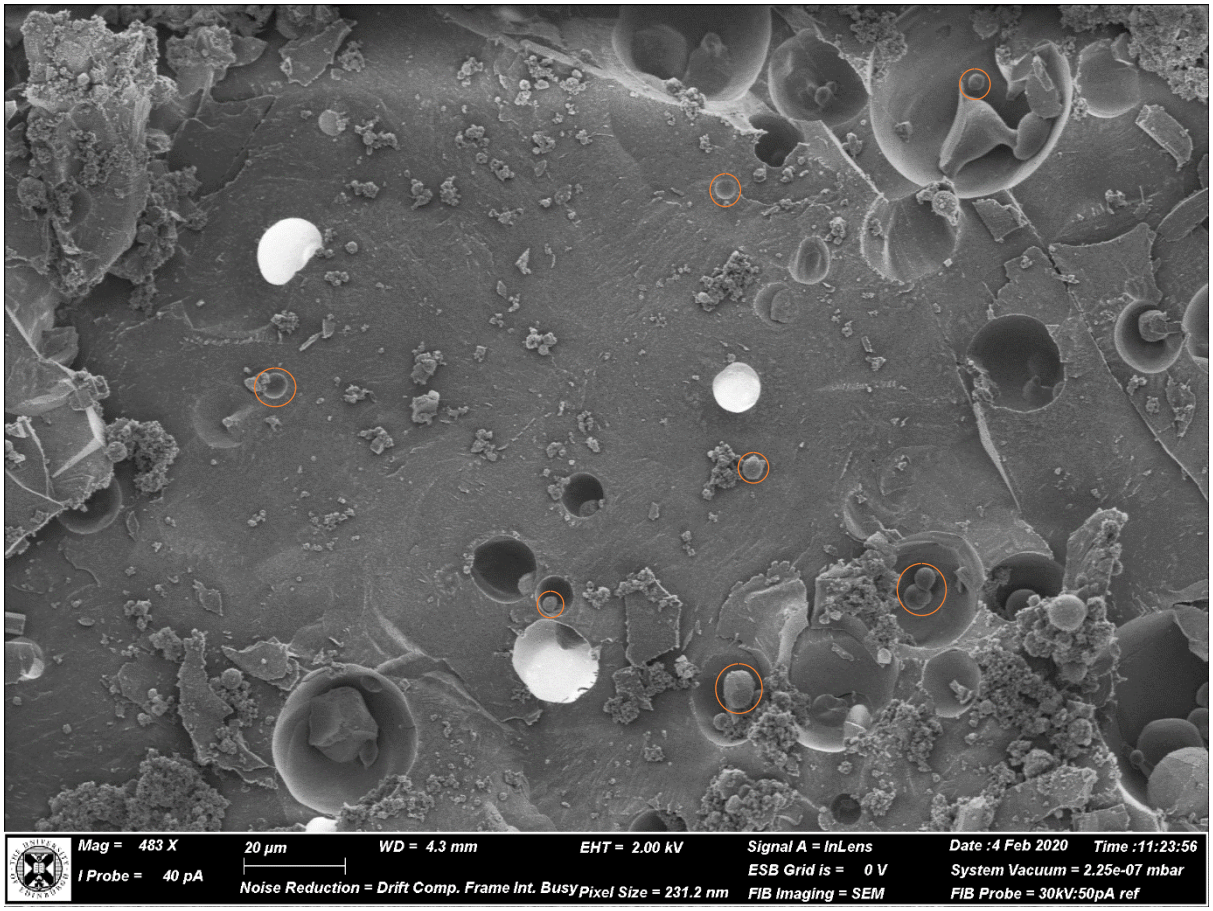

Figure 3.13. *Formations attributed to microbubbles in pure water, indicated with circles. The sample was frozen with liquid nitrogen at high pressure (2000 bar). Measured diameters of the indicated formations vary from 3.04 µm to 6.75 µm.*

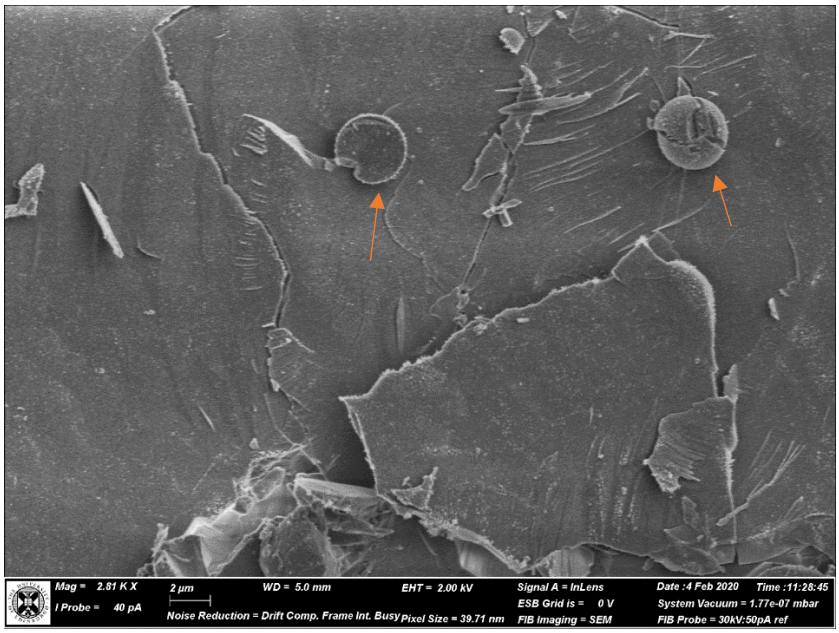

Figure 3.14. *Formations attributed to microbubbles with measured diameters of 3.43 µm (left) and 3.65 µm (right) in pure water. The sample was frozen with liquid nitrogen at high pressure (2000 bar).*

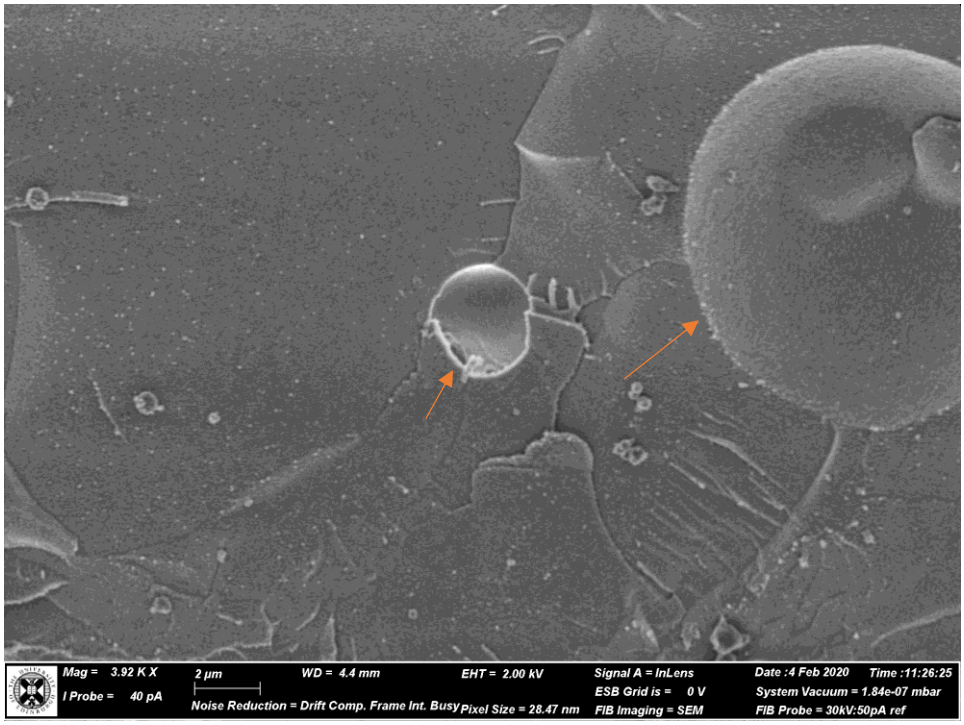

Figure 3.15. *Formations attributed to O_2 microbubbles with measured diameters of 3.33 µm (left) and 11.66 µm (right) in pure water. The sample was frozen with liquid nitrogen at high pressure (2000 bar).*

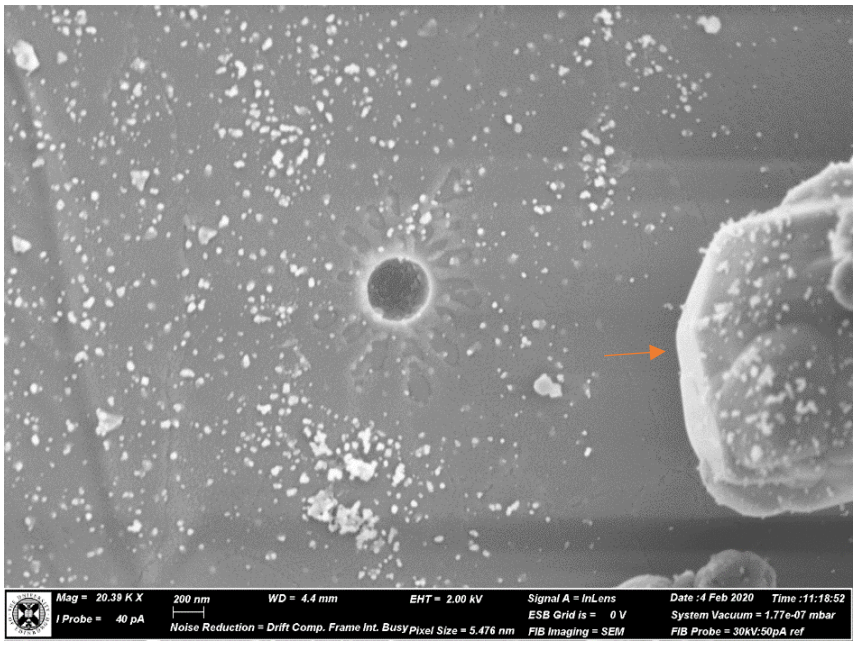

Figure 3.16. *Formation attributed to an O_2 NB with measured diameter of 430 nm in pure water (at the center of the figure). The sample was frozen with liquid nitrogen at high pressure (2000 bar). Ice has developed around the formation. Indicated with an arrow is an ice crystallite with a faceted surface.*

3.2 Pure water with O_2 NBs blended with magnetic ionic liquid (MIL), 20% v/v

In the case of vitrification of the sample of pure water with O_2 NBs at ambient pressure, formations attributed to O_2 NBs were imaged, as seen in Figs. 3.17-3.19. Also, formations attributed to O_2 microbubbles were imaged, as seen in Figs. 3.18-3.19.

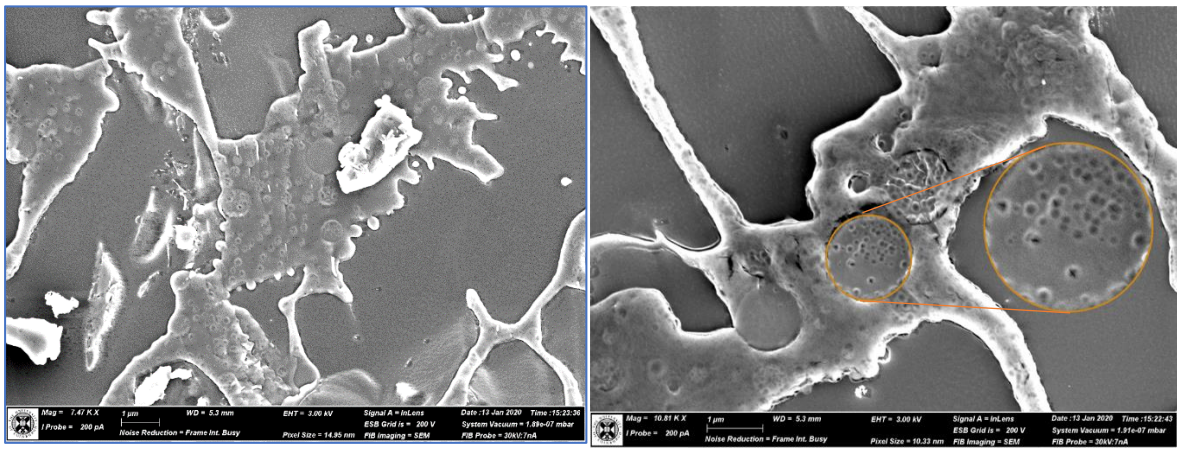

Figure 3.17. *Blots attributed to O_2 NBs in pure water blended with MIL. On the right, a specific area of blots has been magnified. The sample was frozen with liquid nitrogen at ambient pressure. Due to the minute size of the blots, their diameter was not measured accurately, but it is smaller than 200 nm.*

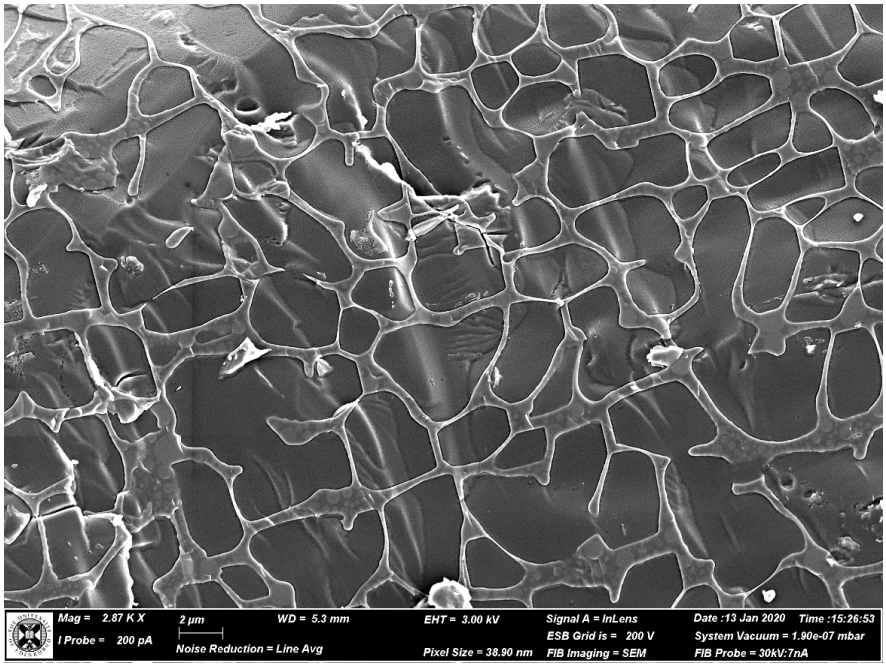

Figure 3.18. *Web-like formations on the surface of the sample of pure water blended with MIL. The sample was frozen with liquid nitrogen at ambient pressure. Inside the web-like formations there are spherical shapes attributed to O_2 NBs and microbubbles. Measurements of their diameter were made in different parts of the web-like formations and they have been found to range from 136 nm to 1.37 µm.*

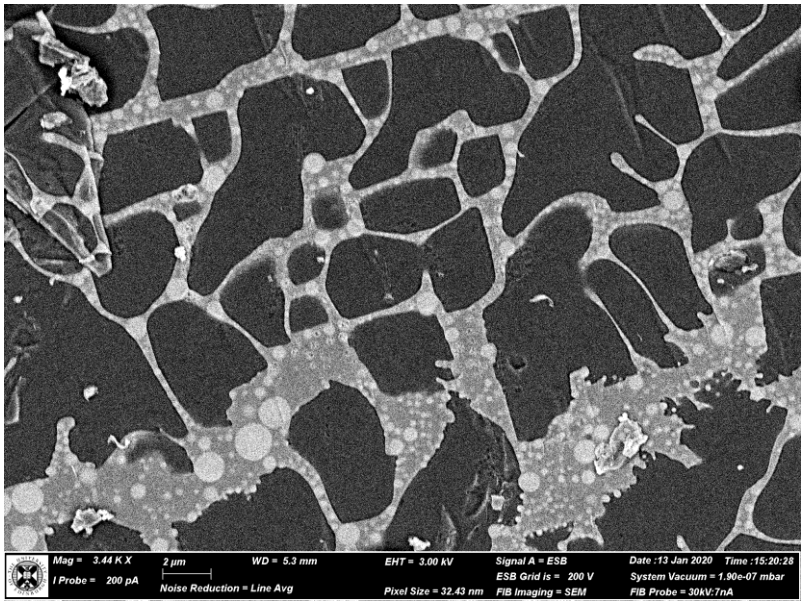

Figure 3.19. *Web-like formations on the surface of the sample of pure water blended with MIL. The sample was frozen with liquid nitrogen at ambient pressure. Inside the web-like formations there are spherical shapes attributed to O_2 NBs and microbubbles. Measurements of their diameter were made in different areas of the web-like formations and they have been found to range from 170 nm to 1.58 µm. Even smaller shapes than 170 nm, attributed to NBs are visible, but due to their minute size, their diameter could not be measured.*

In the case of vitrification of the sample of pure water with O_2 NBs at high pressure (2000 bar), formations attributed to O_2 NBs, microbubbles, as well as bigger O_2 bubbles were imaged. Formations attributed to NBs can be seen in Figs. 3.20, 3.22-3.24, 3.28-3.30 and formations attributed to microbubbles can be seen in Figs. 3.21, 3.25-3.28, 3.30. A formation attributed to a bigger bubble of diameter 12.22 µm can be seen in Fig. 3.21.

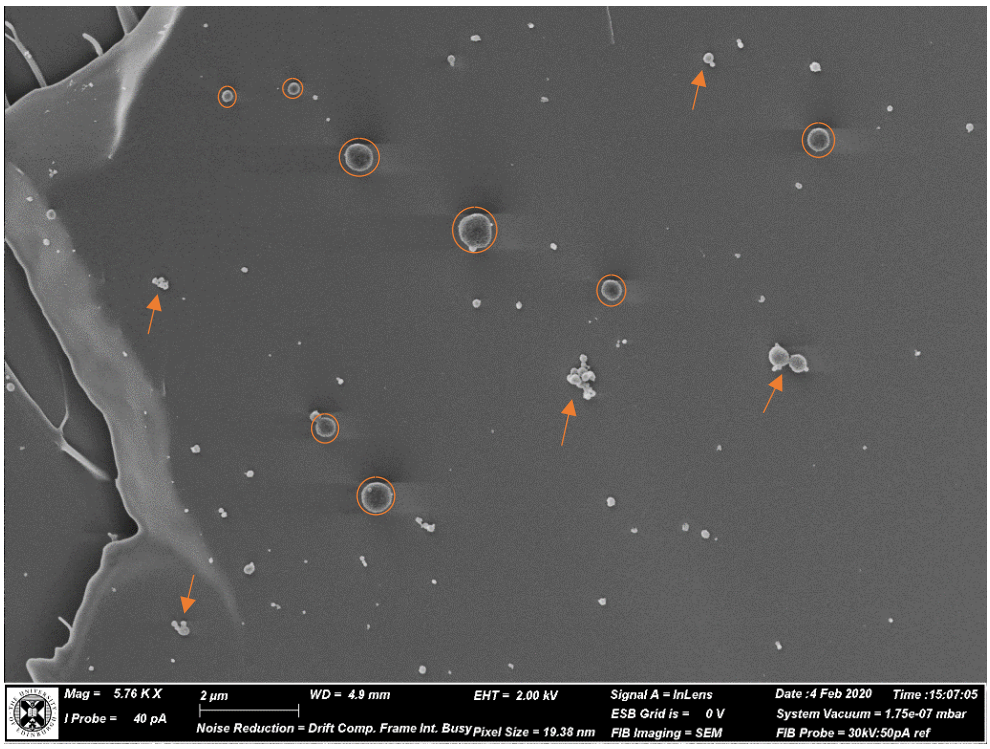

Figure 3.20. *Formations attributed to O_2 NBs in pure water blended with MIL, indicated with circles. The sample was frozen with liquid nitrogen at high pressure (2000 bar). Measured diameters of the indicated formations vary from 236 nm to 649 nm. White formations, some of which are indicated with arrows, are attributed to ice.*

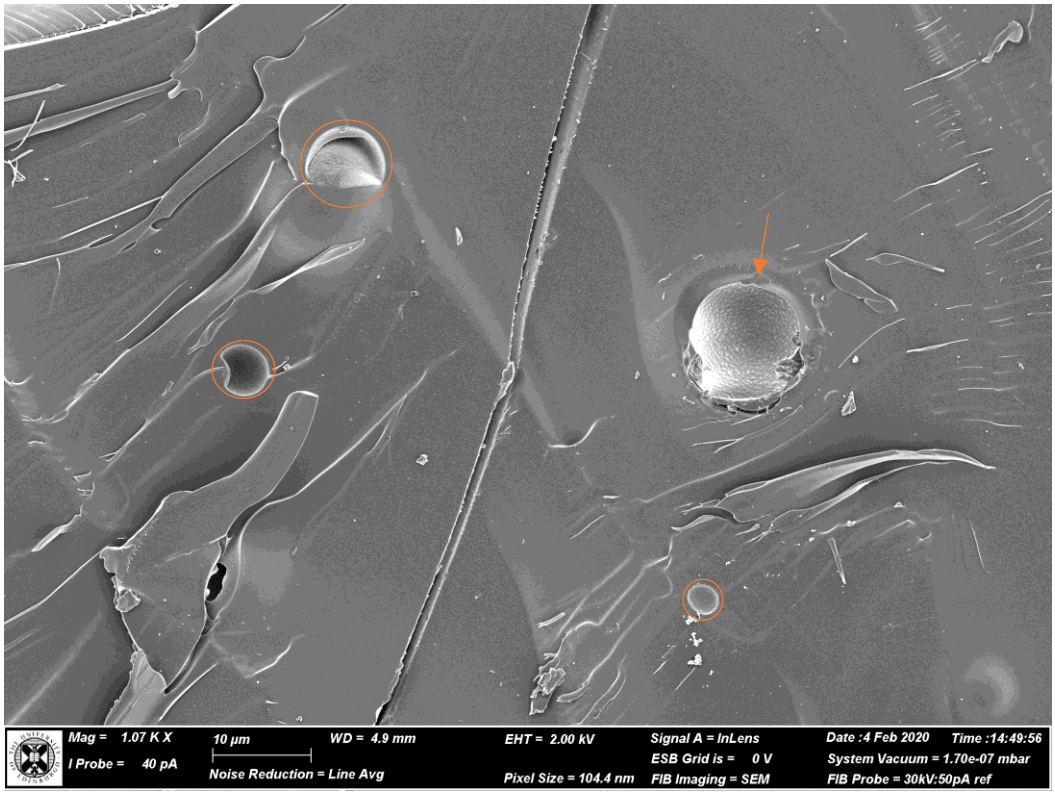

Figure 3.21. *Formations attributed to O_2 microbubbles and a bigger O_2 bubble in pure water blended with MIL are indicated with circles and an arrow, respectively. The sample was frozen with liquid nitrogen at high pressure (2000 bar). Measured diameters of the indicated formations (with circles) attributed to microbubbles vary from 2.96 µm to 8.08 µm. The formation indicated with an arrow has a measured diameter of 12.22 µm.*

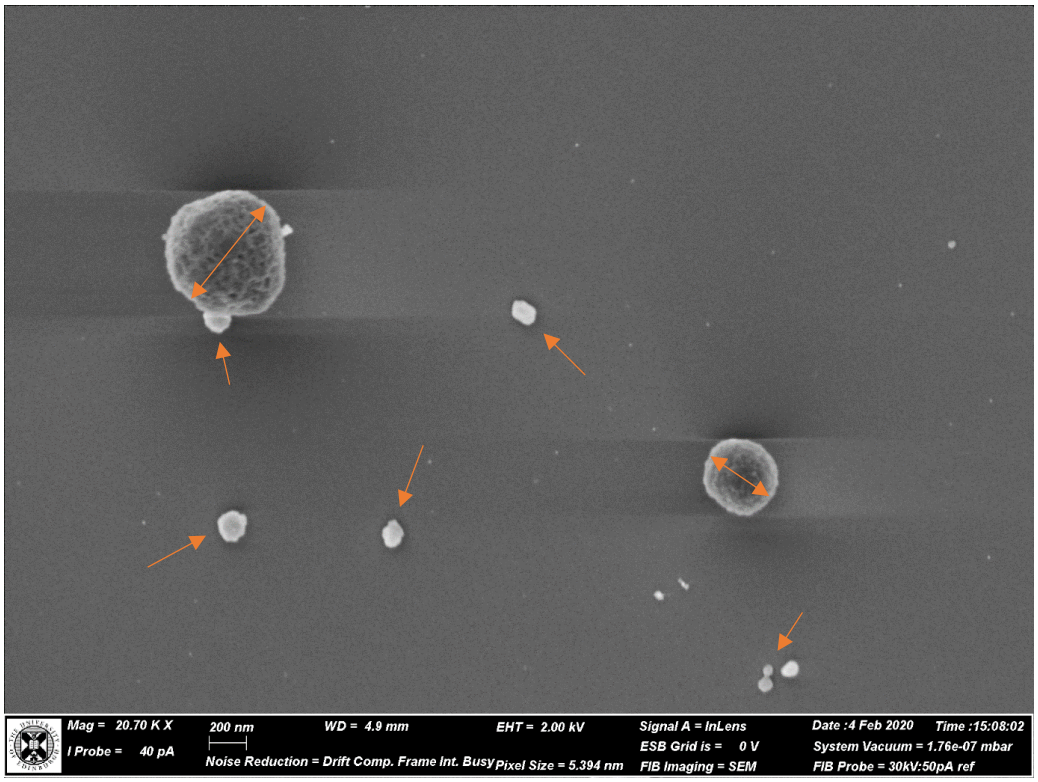

Figure 3.22. *Formations attributed to O_2 NBs, indicated with double arrows, have measured diameters of 699 nm (left) and of 431 nm (right) in pure water blended with MIL, indicated with double arrows. The sample was frozen with liquid nitrogen at high pressure (2000 bar). Smaller white formations observed, some of which are indicated with arrows, are attributed to ice.*

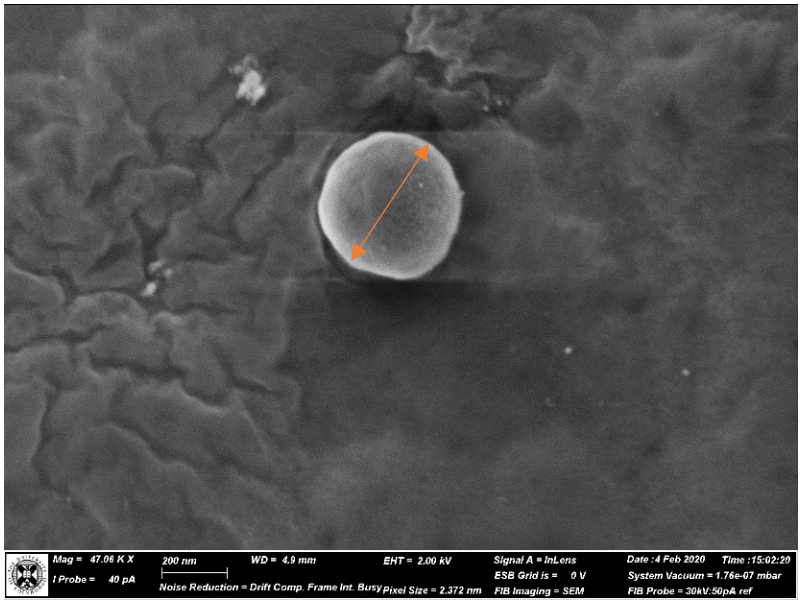

Figure 3.23. *Formation attributed to an O_2 NB with a measured diameter of 426 nm in pure water blended with MIL, indicated with a double arrow. The sample was frozen with liquid nitrogen at high pressure (2000 bar).*

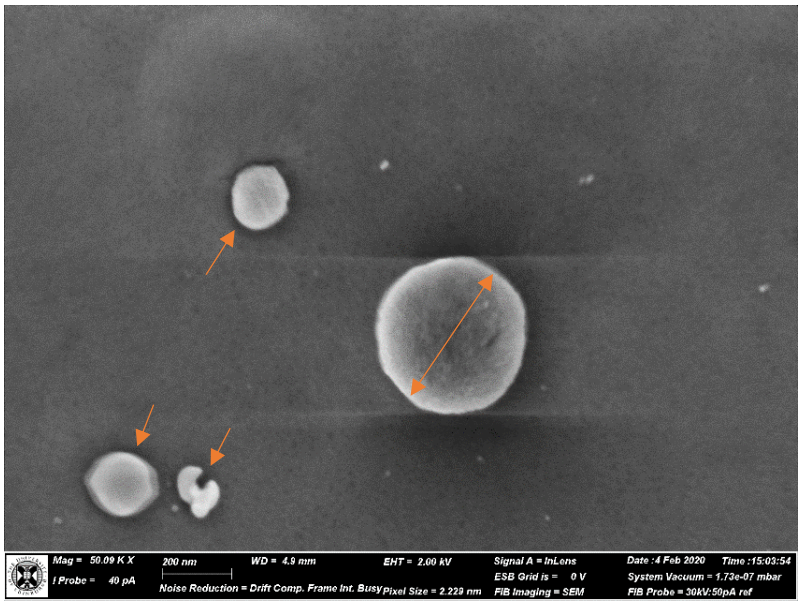

Figure 3.24. *Formation attributed to an O_2 NB with diameter 448 nm in pure water blended with MIL, indicated with a double arrow. The sample was frozen with liquid nitrogen at high pressure (2000 bar). Smaller white formations, indicated with arrows, are attributed to ice.*

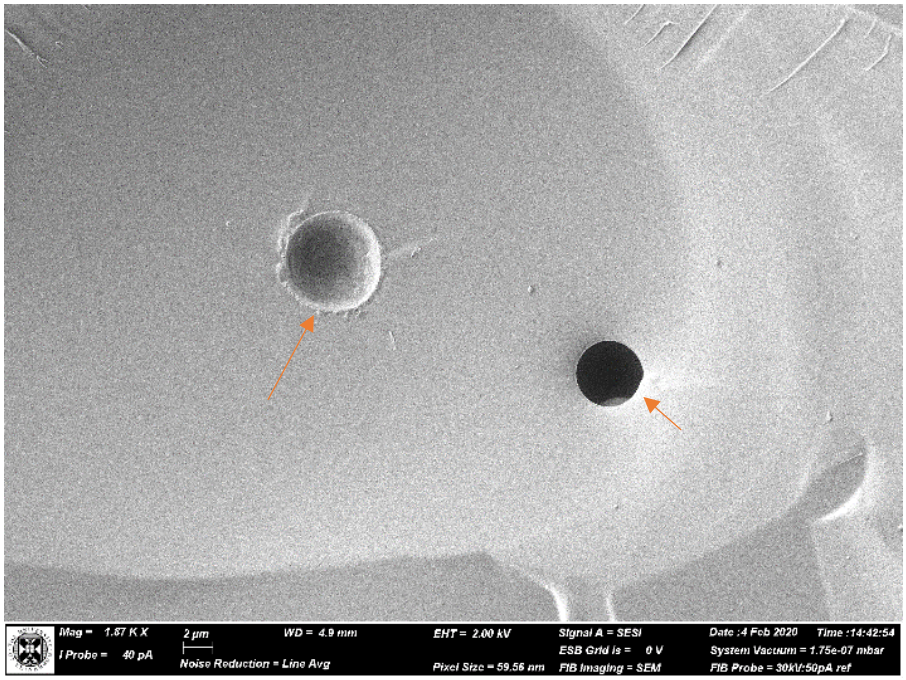

Figure 3.25. *Formations attributed to O_2 microbubbles with calculated diameters of 6.74 µm (left) and of 4.52 µm (right) in pure water blended with MIL, indicated with arrows. The sample was frozen with liquid nitrogen at high pressure (2000 bar).*

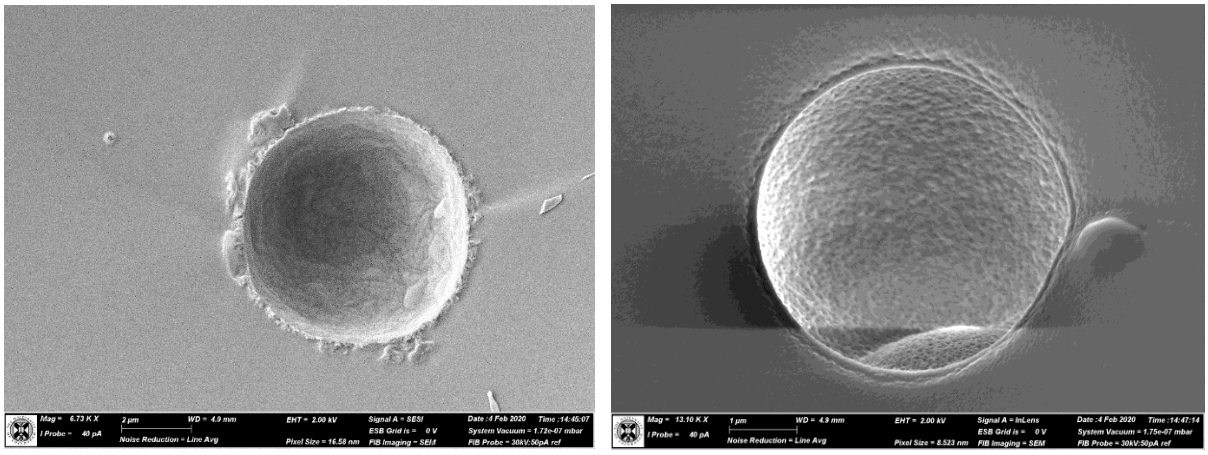

Figure 3.26. *Closer look at the formations imaged in Fig. 3.25 attributed to O_2 microbubbles with calculated diameters of 6.74 µm (left) and 4.52 µm (right) in pure water blended with MIL. The sample was frozen with liquid nitrogen at high pressure (2000 bar).*

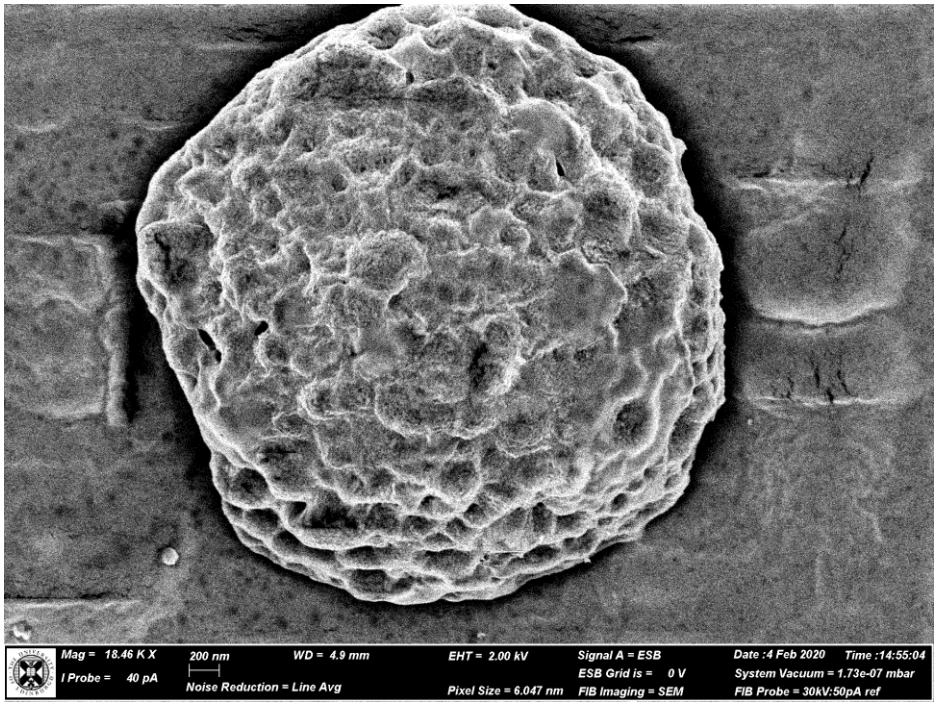

Figure 3.27. *Formation attributed to an O_2 microbubble with a calculated diameter of 4.38 µm in pure water blended with MIL. The sample was frozen with liquid nitrogen at high pressure (2000 bar). The external surface of the microbubble seems uneven and rough, which suggests that contaminants have accumulated on the liquid/gas interface of the microbubble.*

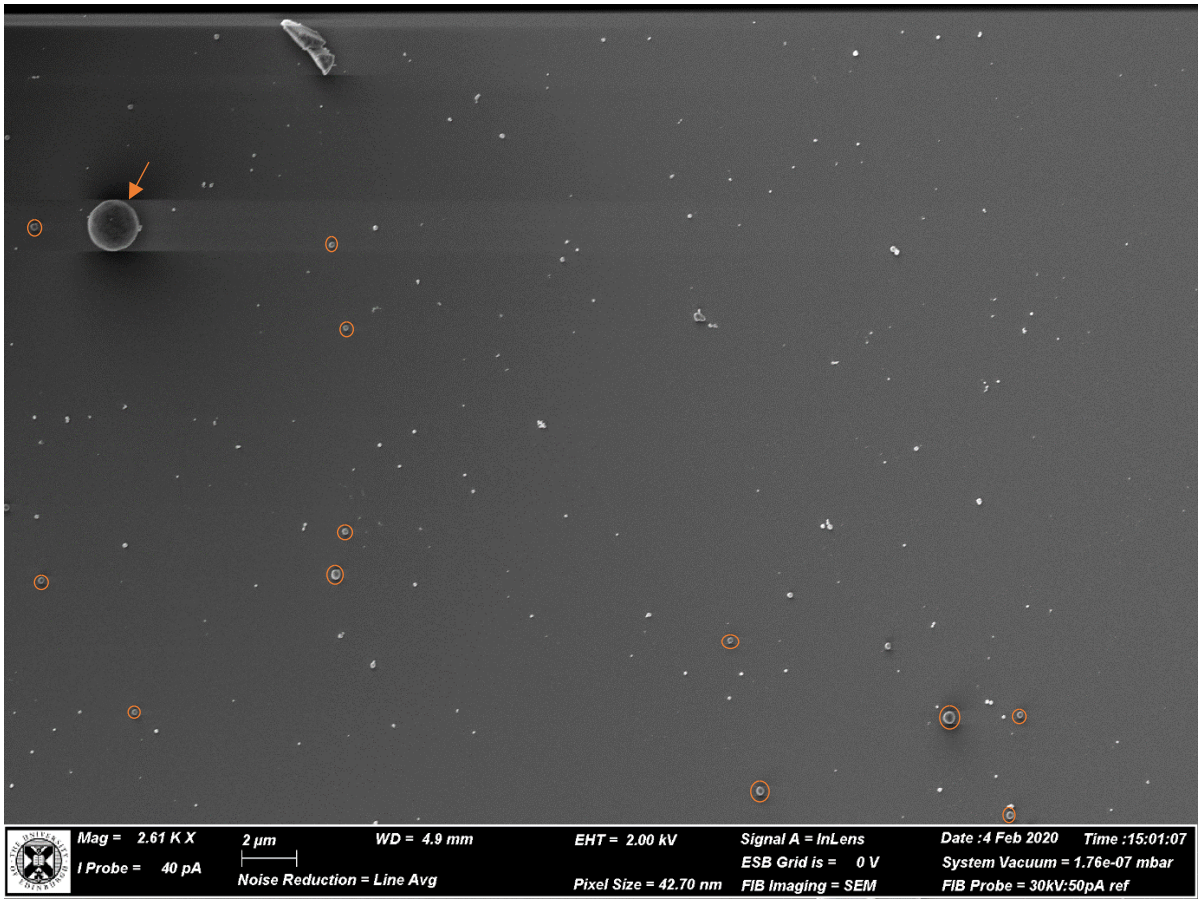

Figure 3.28. *Formations attributed to an O_2 microbubble (indicated with an arrow) of measured diameter 1.75 µm and to O_2 NBs (indicated with circles) of measured diameters ranging from 213 nm to 414 nm in pure water blended with MIL. White spots scattered on the surface of the sample are attributed to ice. The sample was frozen with liquid nitrogen at high pressure (2000 bar).*

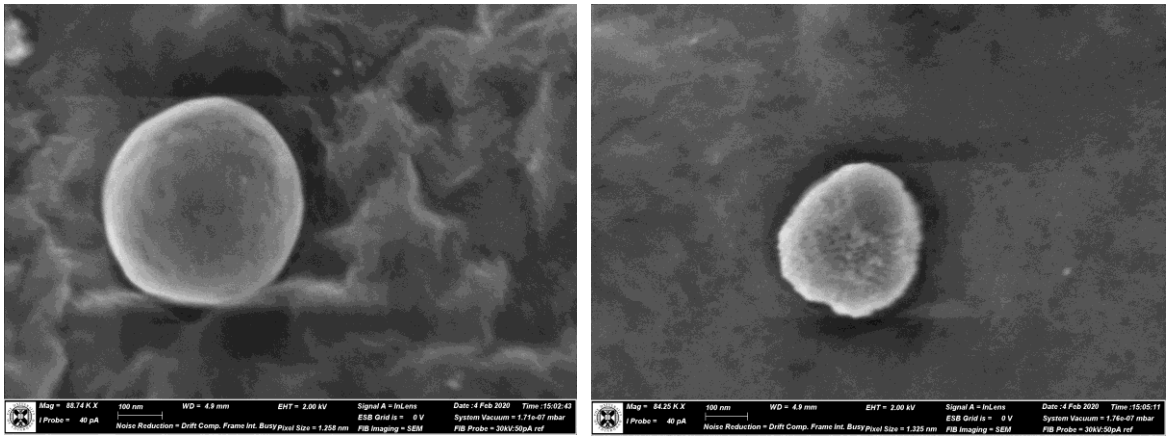

Figure 3.29. *Formations attributed to O_2 NBs of measured diameters 440 nm (left) and 335 nm (right) in pure water blended with MIL. The sample was frozen with liquid nitrogen at high pressure (2000 bar). The formation on the right seems to have an uneven and rough external surface which suggests that contaminants have accumulated on the liquid/gas interface of the NB.*

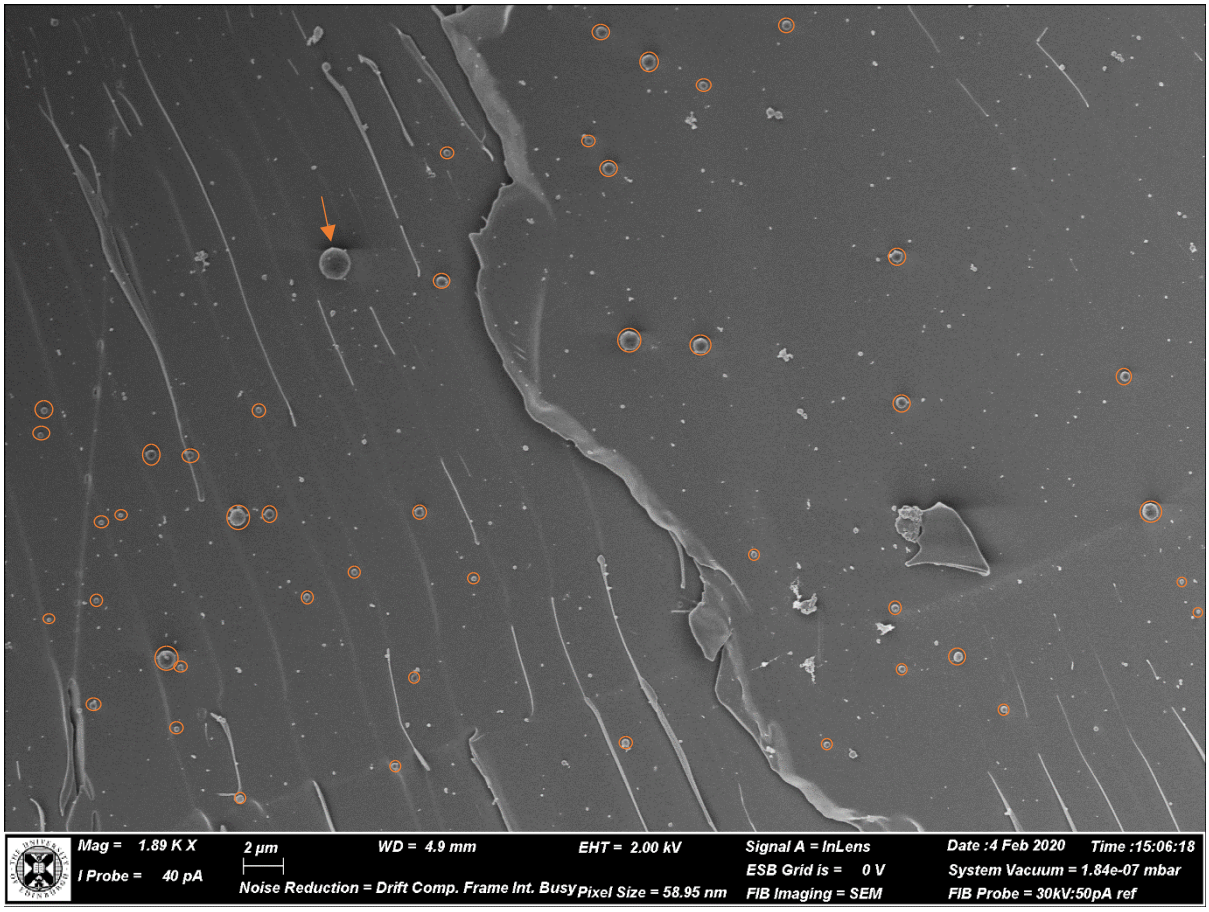

Figure 3.30. *Formations attributed to an O_2 microbubble (indicated with an arrow) of measured diameter 1.51 µm and to O_2 NBs (indicated with circles) of measured diameters ranging from 258 nm to 998 nm in pure water blended with MIL. The sample was frozen with liquid nitrogen at high pressure (2000 bar).*

3.3 Pure water with N_2 NBs

After vitrification at ambient pressure, no NBs were identified during the imaging of the sample, and therefore no figures are presented. In the case of vitrification of the sample of pure water with N_2 NBs at high pressure (2000 bar), formations attributed to both microbubbles and bigger bubbles were imaged, as seen in Figs. 3.31-3.35 and Figs. 3.31-3.32, respectively.

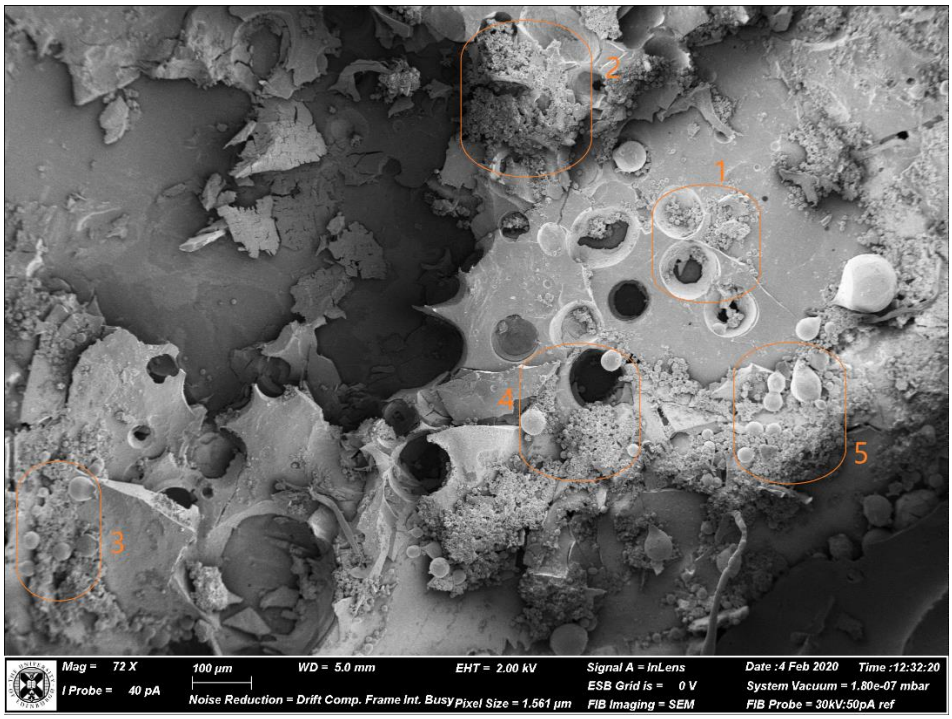

Figure 3.31. *Formations attributed to N_2 microbubbles and bigger bubbles in pure water. The sample was frozen with liquid nitrogen at high pressure (2000 bar). Bubbles are found all across the surface of the sample. Therefore, 5 specific focus points have been chosen, which are indicated by capsule shapes (1-5). 1. Formations attributed to N_2 microbubbles with measured diameters ranging from 7.07 µm to 9.23 µm. 2. Formations attributed to bubbles with measured diameters ranging from 7.02 µm to 11.76 µm. 3. Formations attributed to bubbles with measured diameters between 19.03 µm and 40.50 µm. This part of the image is characterized by blurriness. 4. Formations attributed mainly to microbubbles with measured diameters between 4.43 µm and 8.42 µm, as well as bigger bubbles of measured diameters between 21.69 µm and 44.12 µm. 5. Formations attributed mainly to microbubbles with measured diameters between 5.22 µm and 7.62 µm, as well as bigger bubbles with measured diameters between 11.06 µm and 53.07 µm.*

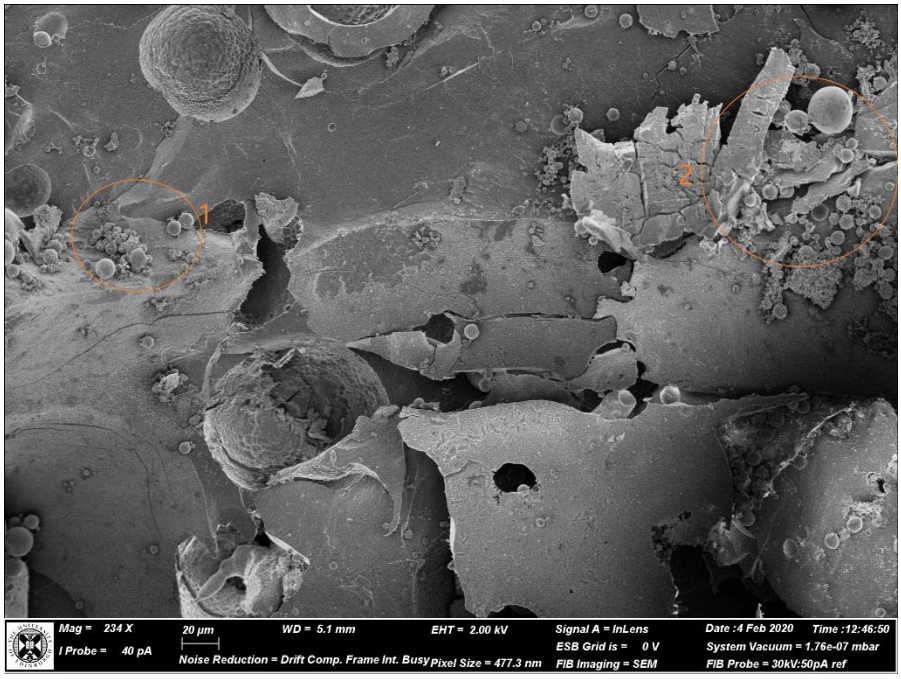

Figure 3.32. *Formations attributed to N_2 microbubbles and bigger bubbles in pure water. The sample was frozen with liquid nitrogen at high pressure (2000 bar). Bubbles are found all across the surface of the sample. Therefore, 2 specific focus points have been chosen, which are indicated by circular shapes (1-2). 1. Formations attributed to N_2 bubbles with measured diameters between 1.72 µm and 11.23 µm. 2. Formations mainly attributed to microbubbles with measured diameters between 2.36 µm and 12.32 µm. Also, two bigger formations are observed and are attributed to bubbles with measured diameters of 12.32 µm and 25.24 µm.*

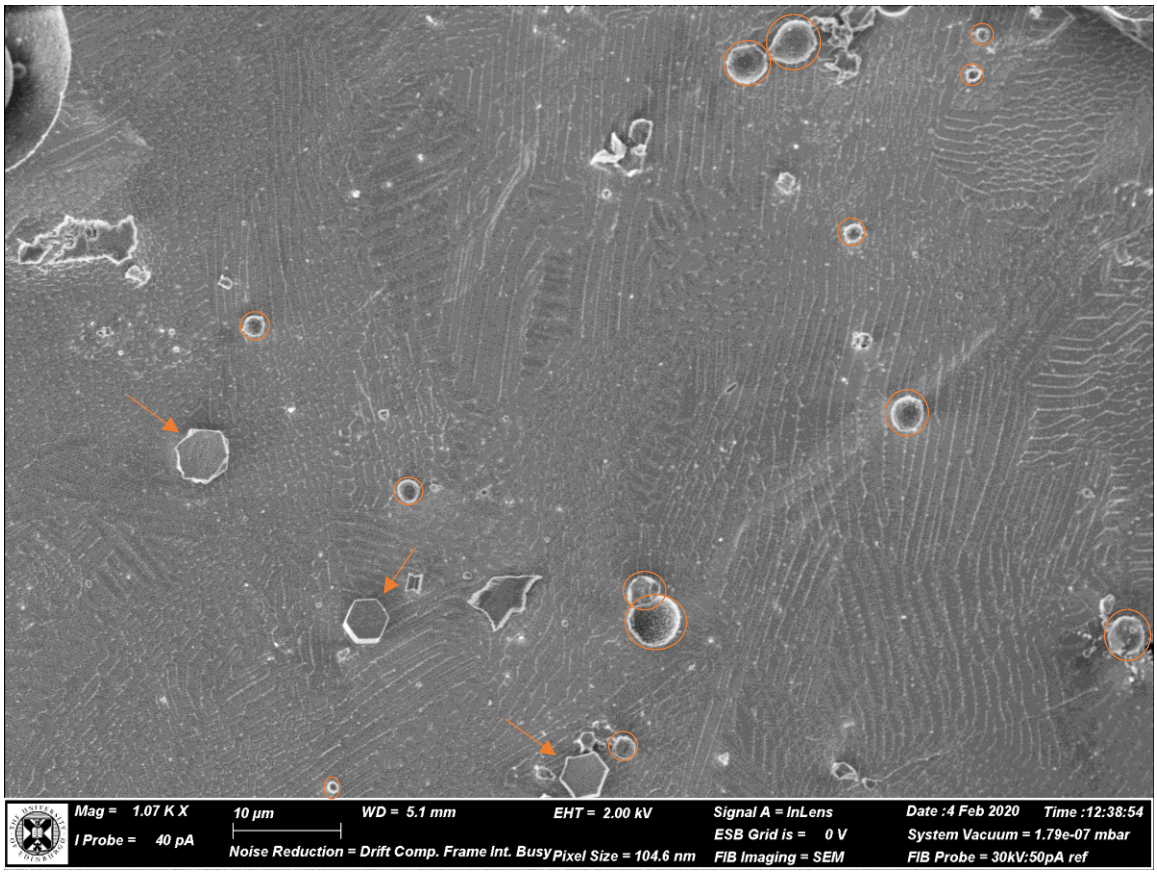

Figure 3.33. *Formations attributed to N_2 microbubbles in pure water, indicated with circles. Formations indicated with arrows are attributed to hexagonal ice crystals. The sample was frozen with liquid nitrogen at high pressure (2000 bar). Measured diameters of the indicated (with circle) formations vary from 1.06 µm to 4.52 µm.*

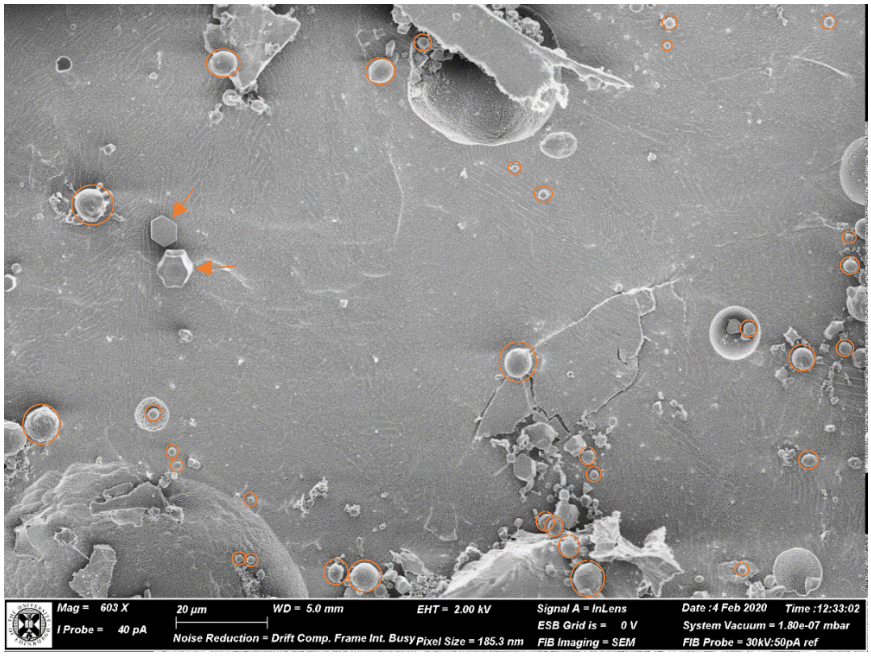

Figure 3.34. *Formations attributed to N_2 microbubbles in pure water, indicated with circles. Formations indicated with arrows are attributed to hexagonal ice crystals. The sample was frozen with liquid nitrogen at high pressure (2000 bar). Measured diameters of the indicated (with circle) formations vary from 1.36 µm to 7.66 µm.*

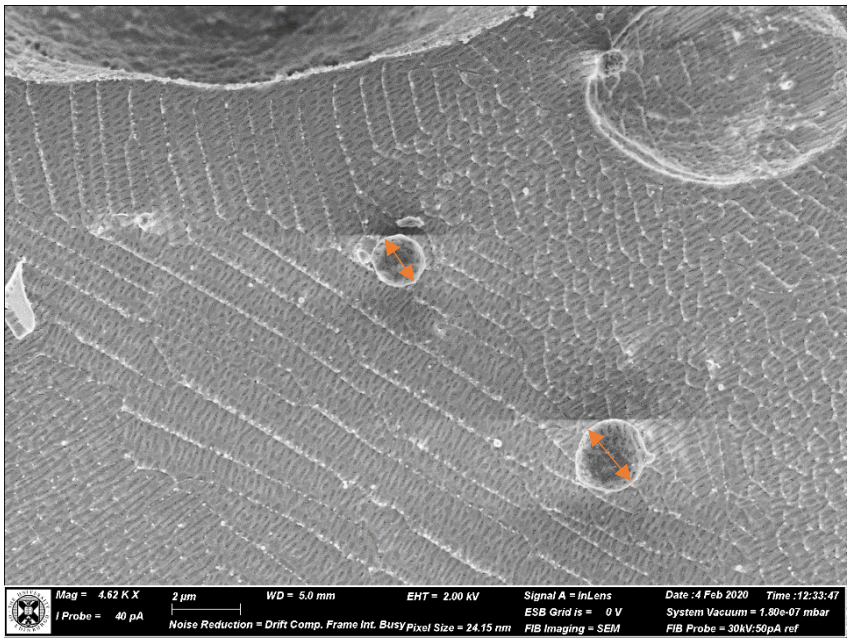

Figure 3.35. *Formations attributed to N_2 microbubbles (indicated with double arrows) in pure water with measured diameters of 1.51 µm (left) and 2.15 µm (right). The sample was frozen with liquid nitrogen at high pressure (2000 bar).*

Moreover, formations that are considered as artefacts were identified on the surface of the sample, as seen in Fig. 3.36.

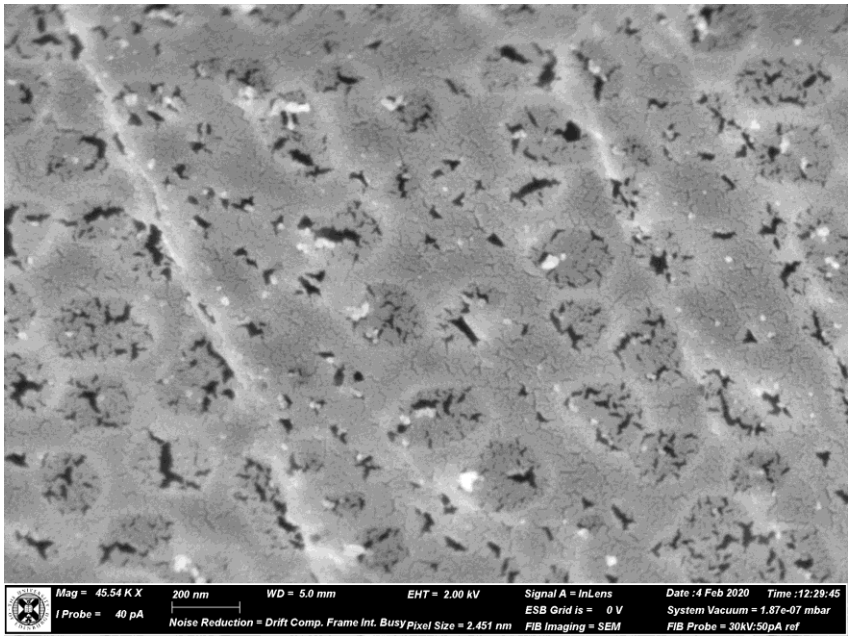

Figure 3.36. *Formations considered as artefacts on the surface of the sample of pure water with N_2 NBs. The sample was frozen with liquid nitrogen at high pressure (2000 bar).*

3.4 Pure water with N_2 NBs blended with magnetic ionic liquid (MIL), 20% v/v

After the vitrification at ambient pressure, no formations that could be attributed to NBs were imaged. Moreover, two phases were present, as can be seen in Figs. 3.37-3.38.

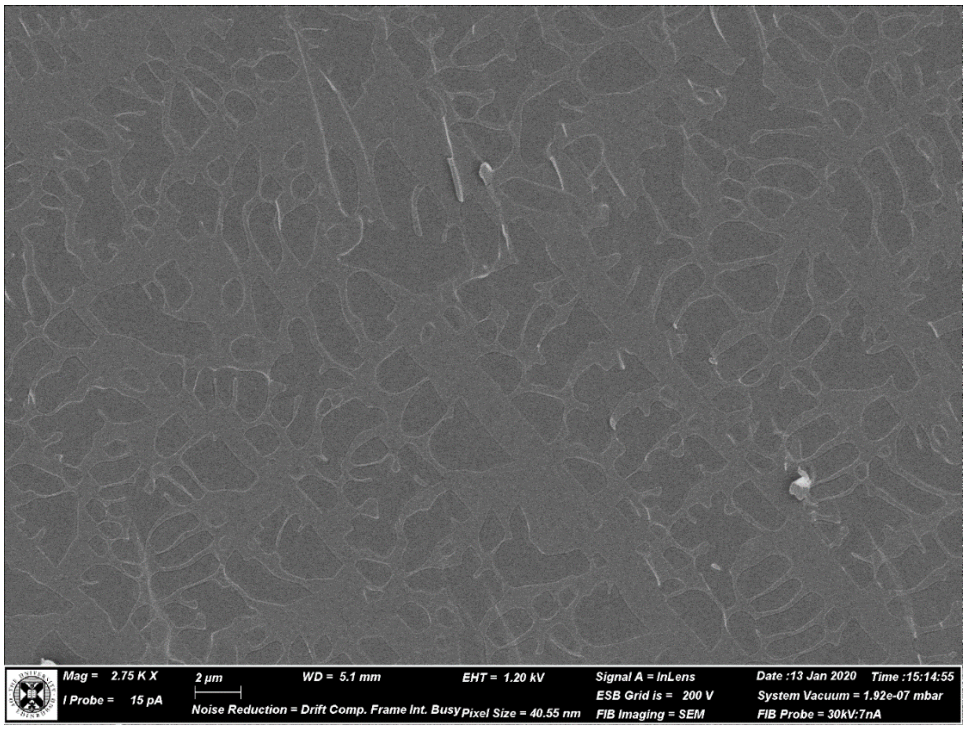

Figure 3.37. *Formations that indicate phase separation between two liquids (the pure water and the MIL) on the surface of the sample of pure water blended with MIL. The sample was frozen with liquid nitrogen at ambient pressure. No formations that could be attributed to N_2 bubbles are observed.*

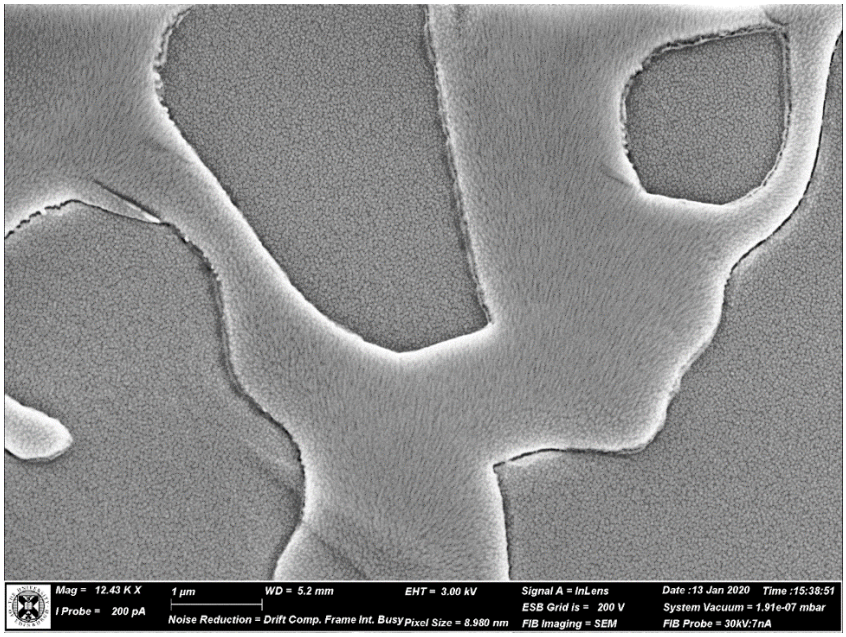

Figure 3.38. *Closer look at the formations created by the separation of phases (observed in Fig. 3.37) in the pure water blended with MIL. The sample was frozen with liquid nitrogen at ambient pressure. No formations that could be attributed to N_2 bubbles are observed.*

In the case of vitrification of the sample of pure water with N_2 NBs blended with MIL at high pressure (2000 bar), spherical and elliptical formations were identified that are considered as artefacts on the surface of the sample, as seen in Fig. 3.39. Moreover, formations that could be attributed to microbubbles were imaged, as seen in Figs. 3.40-3.44.

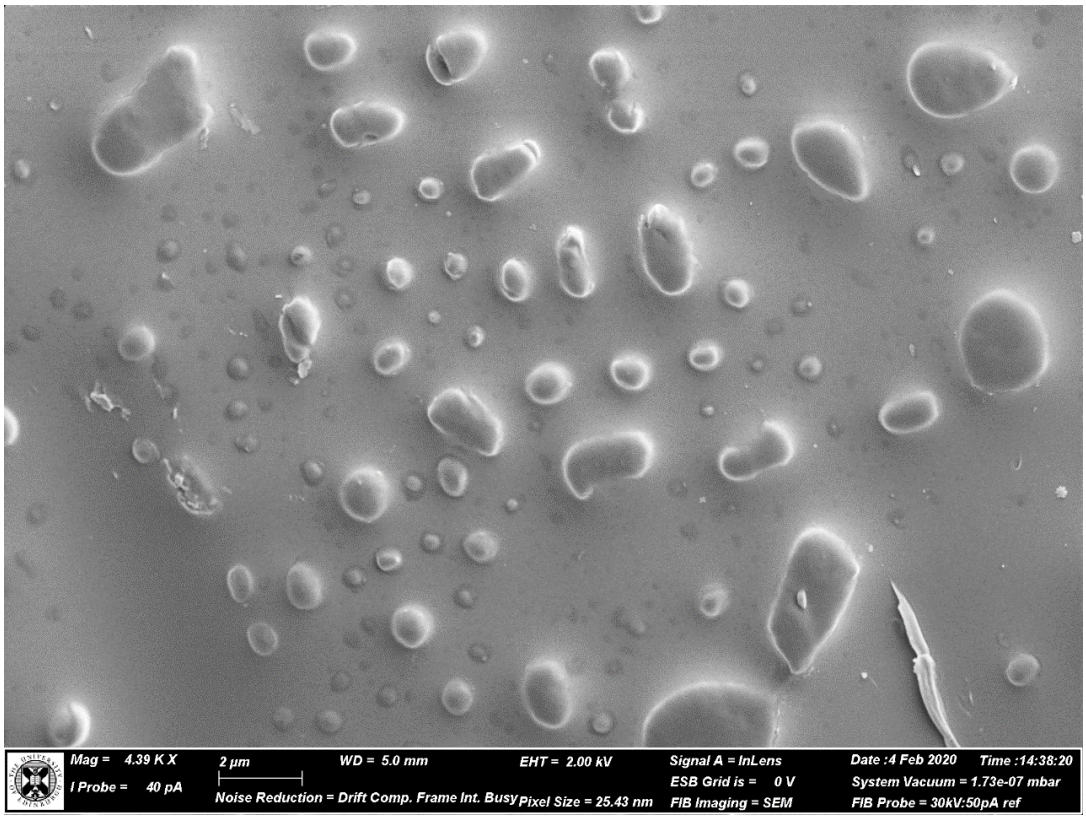

Figure 3.39. *Spherical and elliptical formations considered as artefacts on the surface of the sample of pure water blended with MIL. The sample was frozen with liquid nitrogen at high pressure (2000 bar).*

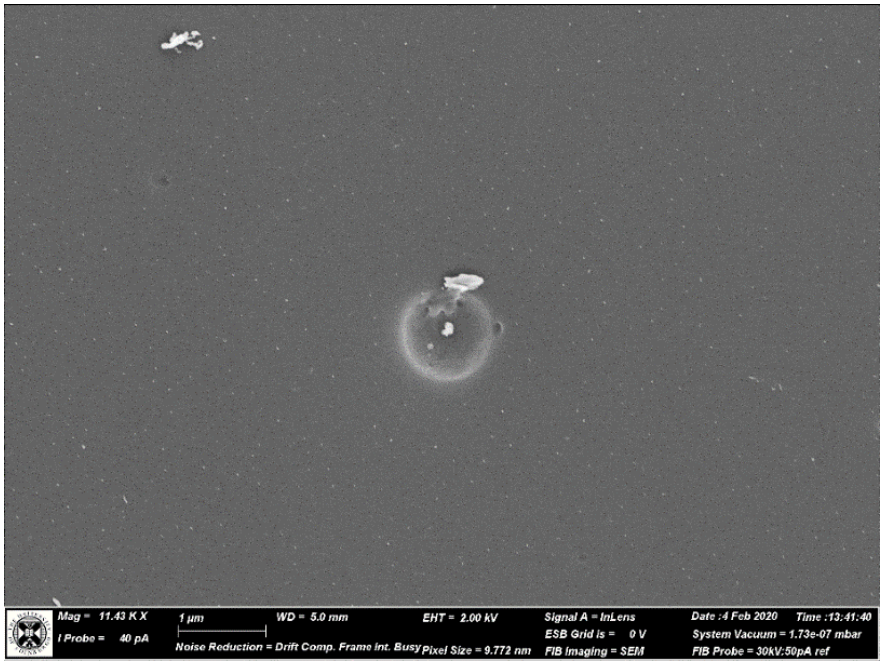

Figure 3.40. *Spherical formation attributed to a N_2 microbubble with measured diameter of 1.02 µm in pure water blended with MIL. The sample was frozen with liquid nitrogen at high pressure (2000 bar).*

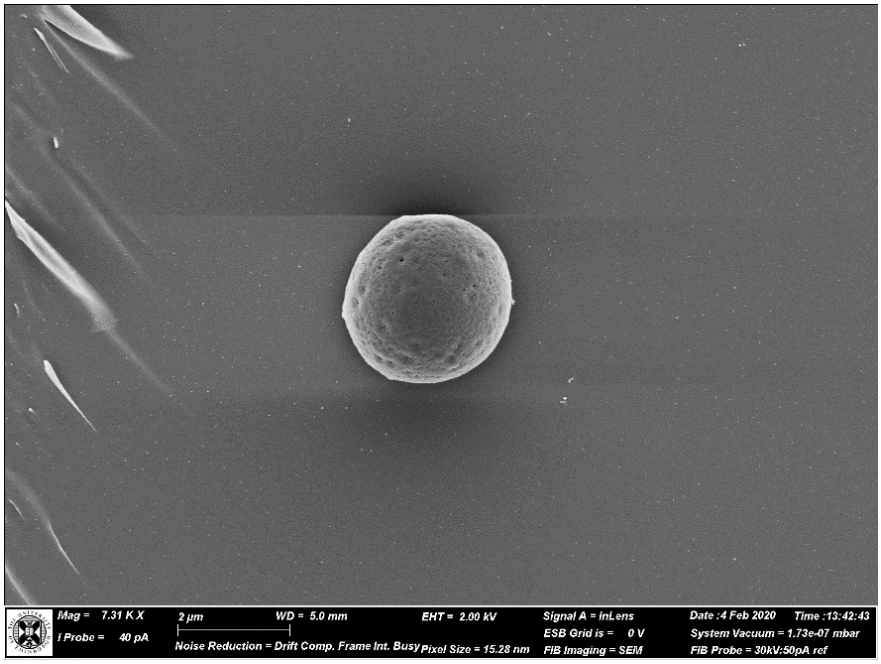

Figure 3.41. *Formation attributed to a N_2 microbubble with measured diameter of 3.10 µm in pure water blended with MIL. The sample was frozen with liquid nitrogen at high pressure (2000 bar).*

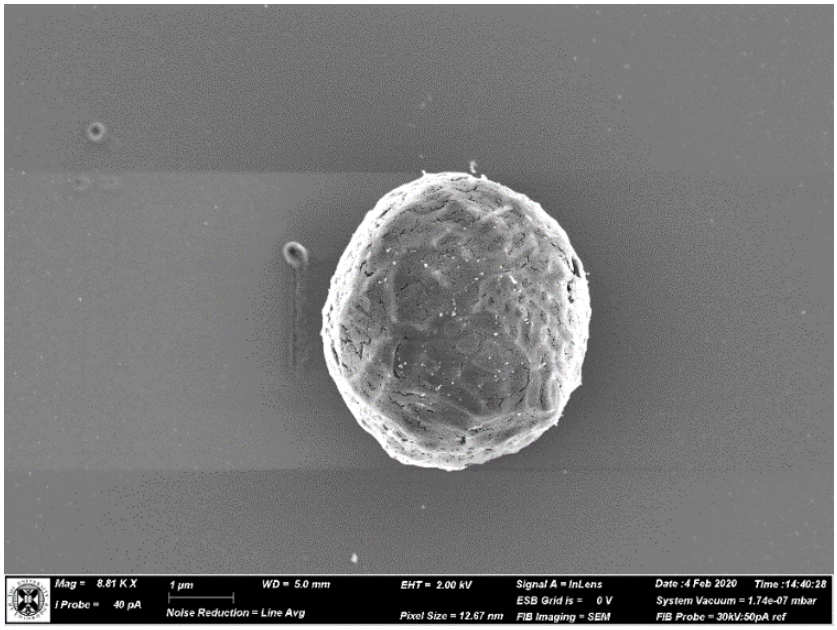

Figure 3.42. *Formation attributed to a N_2 microbubble with measured diameter of 4.28 µm in pure water blended with MIL. The sample was frozen with liquid nitrogen at high pressure (2000 bar).*

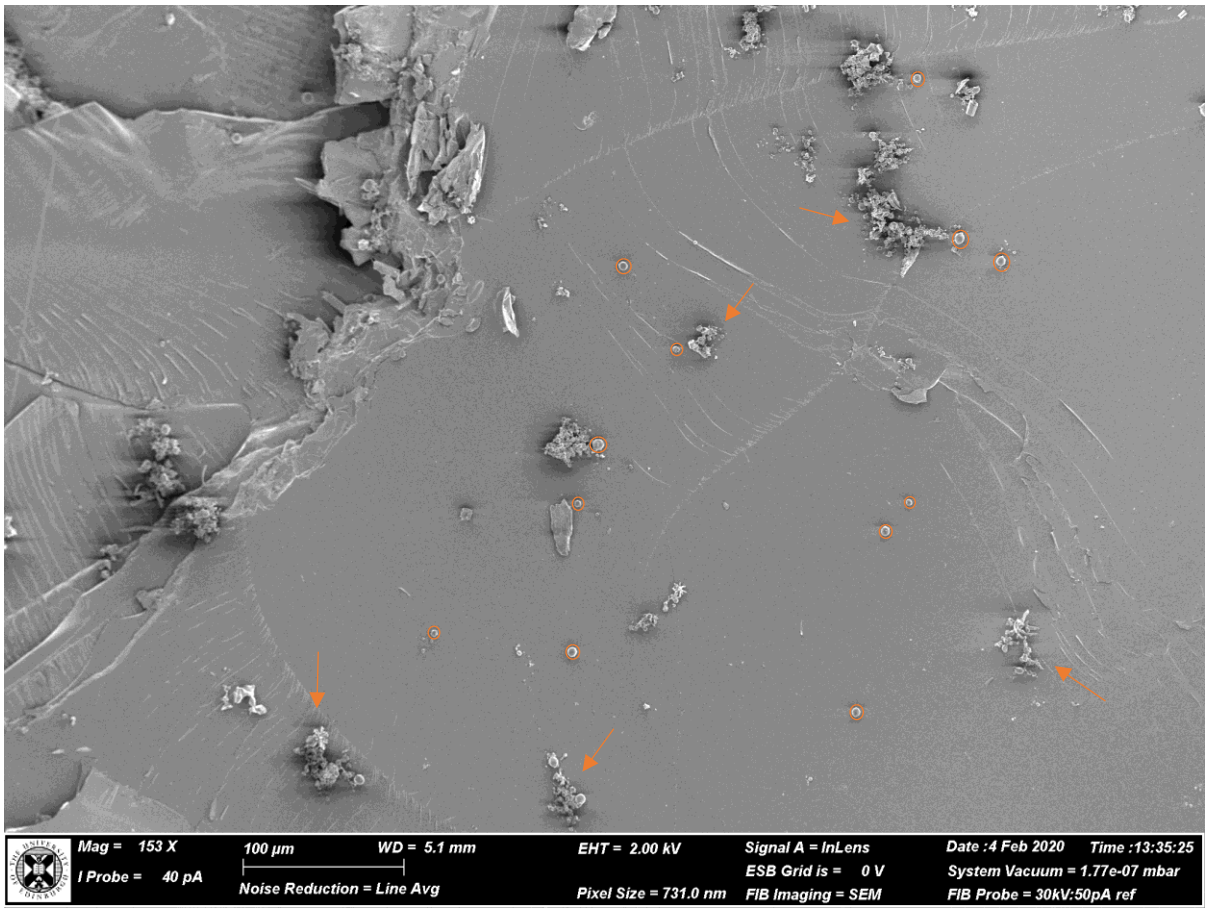

Figure 3.43. *Formations attributed to N_2 MBs (indicated with circles) of measured diameters ranging from 3.87 µm to 6.78 µm in pure water blended with MIL. White formations, indicated with arrows, are attributed to ice. The sample was frozen with liquid nitrogen at high pressure (2000 bar).*

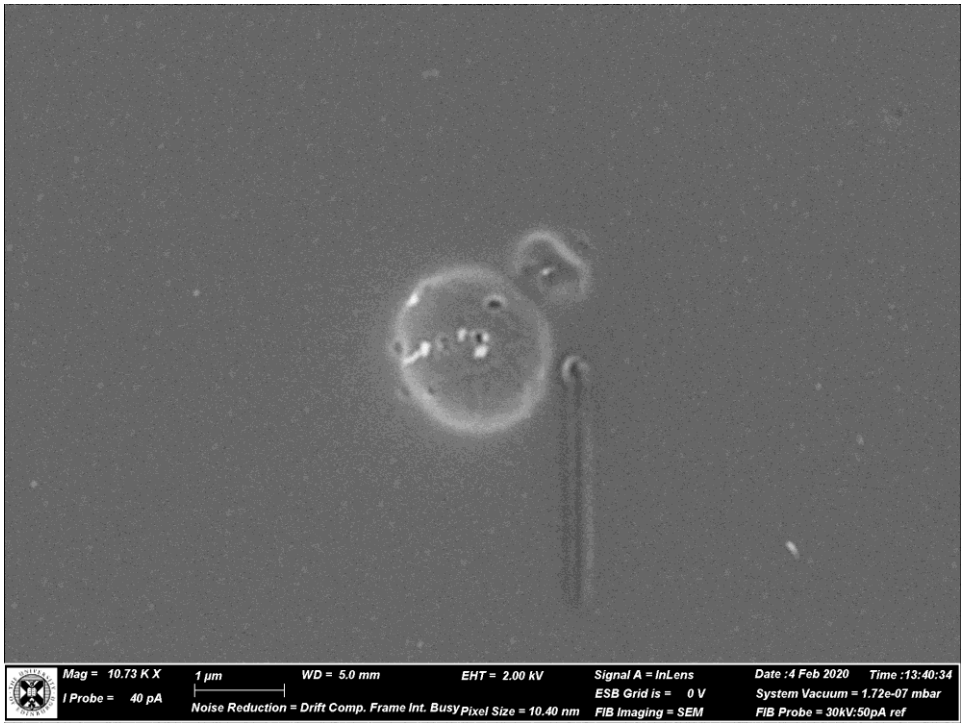

Figure 3.44. *Formation attributed to a N_2 microbubble with measured diameter of 1.85 µm in pure water blended with MIL. The sample was frozen with liquid nitrogen at high pressure (2000 bar).*

4. Discussion

Images were obtained after the observation of the samples at the cryo-SEM facility. Each sample was imaged after preliminary freezing with liquid nitrogen both at ambient pressure and at high pressure (2000 bar).

4.1 Pure water with O_2 NBs

The sample of pure water with O_2 NBs imaged, after its vitrification at ambient pressure, presented formations that were attributed to O_2 NBs and a formation attributed to an O_2 microbubble (as seen in Figs. 3.1-3.8 and Fig. 3.9 respectively). The fact that these formations do not have a fully spherical shape could be the result of the preparation process. In particular, during the preliminary freezing ice may have developed on the surface of the sample, thus altering its morphology. The development of ice on the formations attributed to NBs can be seen in Figs. 3.6-3.7. Formation of ice has also spread across the surface of the sample as seen in Figs. 3.10-3.11. The diameter of the formations we were able to measure, were the ones that had a spherical shape (seen in Figs. 3.1-3.7, 3.9). These diameters vary for the formations attributed to O_2 NBs from 512 to 934 nm (seen in Figs. 3.1-3.7). For the bigger formation attributed to an O_2 microbubble, the measured diameter is 1084 nm (seen in Fig. 3.9).

Contrary to the images obtained for pure water with O_2 NBs after vitrification at ambient pressure, when vitrification is performed at high pressure (2000 bar) the sample provides images where ice does not develop across the surface of the bubbles and it does not seem to influence their morphology, due to the high freezing rate. However, ice has developed around the bubbles, and this can be seen in Fig. 3.16. Also, the images obtained after preliminary freezing at high pressure present a larger number of spherical formations across the surface of the sample. The smaller number of NBs in the case of preliminary freezing at ambient pressure could be attributed to the smaller freezing rate that led to ice

being developed across the surface of the sample, preventing the observation of more NBs. Moreover, the spherical formations in the case of freezing at high pressure seem to be bigger in size in comparison with the images obtained after freezing at ambient pressure. In particular, most spherical formations were attributed to O_2 microbubbles with diameters ranging from 2.13 μm to 9.80 μm, as seen in Figs. 3.12-3.15. Moreover, formations attributed to O_2 NBs were imaged. Such formation with a measured diameter of 430 nm can be seen in Fig. 3.16. Also, a formation attributed to a bigger O_2 bubble with a measured diameter of 11.66 μm was imaged (as seen in Fig. 3.15).

The sample of pure water with O_2 NBs presented formations with diameter bigger than 1 μm after freezing at high pressure (2000 bar) that were not visible after freezing at ambient pressure (except from a formation with a diameter of 1084 nm seen in Fig. 3.9). One explanation could be that due to high pressure (2000 bar) during the freezing process, NBs merged thus producing bigger bubbles. Another parameter for the coalescence could be the time difference between the two experiments, as the experiments with high-pressure freezing were conducted 3 weeks after the ones with ambient pressure freezing. However, according to the literature [12], this time period could result in the diameters of the NBs being slightly increased but not in them being merged into microbubbles. Therefore, it is concluded that the high pressure (2000 bar) during the preliminary freezing was the reason for the coalescence of NBs and the formation of the microbubbles imaged.

DLS measurements and observation of the Tyndall effect were performed for similar O_2 NBs in pure water that had been produced by counterflow hydrodynamic cavitation with the same generator [12]. After 30 min of processing time, the mean size of the O_2 NBs according to DLS was 350 nm. Moreover, after observation of the Tyndall effect, the solution with O_2 NBs scattered the light of a green laser beam (with wavelength 495-570 nm). This observation was considered indicative for the existence of NBs with diameters between 400 and 900 nm. The NBs we observed, after freezing at ambient pressure, have a measured diameter of 512-934 nm (Figs. 3.1-3.7). These diameters are all bigger than the mean size measured by DLS, but their diameters are within the range expected according to the Tyndall effect (except from the NB of measured diameter 934 nm of Fig. 3.1). Smaller NBs would be expected according to the mean size measured by the DLS technique. However, it is suggested that ice developed across the surface of the sample prevents the observation of smaller NBs. In the case of the freezing at high pressure (2000 bar) the NB observed has a measured diameter of 430 nm (Fig. 3.16) which is bigger than the mean size measured by DLS but the diameter is within the range expected by the Tyndall effect. At the same time, as mentioned above, NBs have merged into microbubbles after freezing at high pressure, and therefore the formations of bubbles observed after this preliminary freezing technique cannot be correlated to the mean size of NBs measured by DLS, as our observations would not be representative of the initial sample imaged.

4.2 Pure water with O_2 NBs blended with magnetic ionic liquid (MIL), 20% v/v

The sample of pure water with O_2 NBs blended with MIL imaged, after its vitrification at ambient pressure, presented formations attributed to O_2 NBs and microbubbles as seen in Figs. 3.17-3.19 and Figs. 3.18-3.19 respectively. In these Figures, the water phase seems to have separated from the phase of the MIL, due to the web-like formations that constitute the MIL phase created on the sample's surface. These formations of the MIL phase may be the result of different molecular weights between the pure water and the MIL. Subsequently, the bubbles present in pure water in the initial sample have redispersed into the MIL phase. In Fig. 3.17, blots are imaged in the MIL phase that are attributed to NBs. Due to their minute size, precise measurement of their diameters has not been made, but they are estimated to be smaller than 200 nm. The web-like formations that presumably constitute the MIL phase

are clearly imaged in Figs. 3.18-3.19. Spherical formations are identified across all the web-like formations. These formations are considered as NBs and microbubbles with measured diameters ranging from 136 nm to 1.58 μm. It is noted that the range of diameters discussed is presented after having evaluated different areas of the web-like MIL phase. The existence of microbubbles may have preexisted in the sample or may be considered as a result of coalescence of NBs. In particular, it is possible that as the MIL phase has created the web-like formations on the sample's surface, NBs existing in the MIL phase have been pushed together and as a result they have merged into microbubbles. Moreover, it is noted that although the vitrification was performed at ambient pressure, ice does not seem to have developed on the surface of the bubbles, and therefore does not influence the observation of the bubbles.

In the case of vitrification of the sample at high pressure (2000 bar), the images obtained present formations, attributed to bubbles, with a wide range of sizes. In particular, formations attributed to NBs were imaged with measured diameters ranging from 213 nm to 998 nm as seen in Figs. 3.20, 3.22-3.24 and 3.28-3.30. Also, formations attributed to microbubbles ranging from 1.75 μm to 8.08 μm were imaged, as seen in Figs. 3.21, 3.25-3.28 and 3.30. In addition, a bigger formation of measured diameter 12.22 μm was imaged, as seen in Fig. 3.21. Moreover, there are obvious signs of unevenness and roughness on the external surface of the formation of Fig. 3.27, attributed to a microbubble and the right formation of Fig. 3.29, attributed to a NB. These characteristics are considered to be the result of contamination accumulated on the liquid/gas interface of the bubbles [20], as explained by the contamination theory in paragraph 2.1.1 of Chapter 1. These contaminants may have accumulated on the surface of the NBs during their generation process. Also, across the surface of the sample white formations attributed to ice have been imaged, as indicated in Figs. 3.20, 3.22 and 3.24. However, ice does not develop across the surface of the bubbles and it does not seem to influence their morphology, due to the high freezing rate.

Contrary to the vitrification at ambient pressure, after vitrification at high pressure (2000 bar) bigger bubbles are generally observed. In particular, NBs with diameters smaller than 200 nm were not observed. Furthermore, although in the case of ambient pressure the biggest microbubble was measured to have a diameter of 1.58 μm, after preparation at high pressure, the images obtained present formations attributed to even bigger bubbles, the biggest of which has a measured diameter of 12.22 μm (Fig. 3.21). It is suggested that the high pressure (2000 bar) during the preliminary freezing is the reason why coalescence of NBs was achieved and resulted in the formation of the bigger bubbles imaged. Moreover, the MIL phase after vitrification at high pressure did not present any web-like formation on the sample's surface, contrary to the imaged sample after vitrification at ambient pressure. It is deemed that due to the high freezing rate of the sample during the vitrification at high pressure, these web-like formations did not form, and that the phase of the pure water and the MIL did not separate.

DLS measurements and observation of the Tyndall effect were performed for similar O_2 NBs in pure water that had been produced by counterflow hydrodynamic cavitation with the same generator [12]. After 30 min of processing time, the mean size of the O_2 NBs according to DLS was 350 nm. Moreover, after observation of the Tyndall effect, the solution with O_2 NBs scattered the light of a green laser beam (with wavelength 495-570 nm). This observation was considered indicative for the existence of NBs with diameters between 400 and 900 nm. The bubbles we observed, after freezing at ambient pressure, have a wide range of diameters measured at 136 nm–1.58 μm (Figs. 3.18-3.19). These diameters could agree with the mean size measured by DLS and several of the NBs observed have diameters within the range expected according to the Tyndall effect. In the case of the freezing at high

pressure (2000 bar) the NBs observed have measured diameters ranging from 213 nm to 998 nm (Figs. 3.20, 3.22-3.24 and 3.28-3.30) which could agree with the mean size measured by DLS, taking into consideration also the fact that some of these NBs could be the result of coalescence of smaller NBs. Finally, several of the NBs observed have a diameter within the range expected by the Tyndall effect.

4.3 Pure water with N_2 NBs

The sample of pure water with N_2 NBs imaged, after its vitrification at ambient pressure, presented no formations of NBs. The reason why observation of the NBs was not successful may involve the preliminary freezing performed. In particular, ice could have developed on the sample's surface, which may have led to the prevention of the observation of NBs, as they would be "hidden" behind the ice. Also, another parameter could be the size of the NBs. If they are too small, it would be more difficult to identify them on the surface of the sample.

In the case of vitrification at high pressure (2000 bar), formations attributed to bubbles with a wide range of diameters were identified. These formations are considered as microbubbles (as seen in Figs. 3.31-3.35) and bigger bubbles (as seen in Figs. 3.31-3.32). As no NBs were identified, it is suggested that the high pressure (2000 bar) during the preliminary freezing is the reason why coalescence of NBs was achieved and resulted in the formation of the bigger bubbles imaged. Moreover, artefacts were identified on the surface of the sample, as seen in Fig. 3.36. These artefacts may have formed either during the NBs' generation process in pure water, or during the preparation procedure before the cryo-SEM imaging. In addition, ice is observed in the form of hexagonal ice crystals (see Figs. 3.33 and 3.34). Nevertheless, ice does not develop across the surface of the bubbles observed, and it does not seem to influence their morphology, due to the high freezing rate.

DLS measurements and observation of the Tyndall effect were performed for O_2 and air NBs in pure water that had been produced by counterflow hydrodynamic cavitation with the same generator [12]. After 30 min of processing time, the mean size of the O_2 NBs and the air NBs, according to DLS, were 350 nm and 430 nm respectively. Moreover, after observation of the Tyndall effect, the solution with N_2 NBs scattered the light of a green laser beam (with wavelength 495-570 nm). This observation was considered indicative for the existence of NBs with diameters between 400 and 900 nm. After freezing at ambient pressure, we could not observe any NBs. This fact is attributed to the development of ice across the surface of the sample, due to low freezing rate, that presumably prevents the observation of formations "hidden" behind its surface. In the case of the freezing at high pressure (2000 bar) again no NBs were observed. However, formations attributed to N_2 microbubbles and bigger bubbles were identified after freezing at high pressure (2000 bar) (Figs. 3.31-3.35). These diameters do not agree with the DLS measurements nor with the observation of the Tyndall effect, and they are considered to be the result of the coalescence of NBs due to the high pressure of the preliminary freezing.

4.4 Pure water with N_2 NBs blended with magnetic ionic liquid (MIL), 20% v/v

The sample of pure water with N_2 NBs blended with MIL imaged after its vitrification at ambient pressure presented formations that could be the result of phase separation, between the phase of the water and the phase of the MIL, as seen in Figs. 3.37-3.38. The reason behind the phase separation could be the different molecular weight of the components of the liquids, i.e. the water and the MIL (as in the case of pure water with O_2 NBs blended with MIL imaged, as seen in Figs. 3.17-3.19). Moreover, no formations that could have been attributed to bubbles were identified.

In the case of vitrification of the sample at high pressure (2000 bar), elliptical and spherical artefacts were present on the surface of the sample, as seen in Fig. 3.39. These artefacts may have formed either during the NBs' generation process in pure water, or during the preparation procedure before the cryo-SEM imaging. Furthermore, formations attributed to N_2 microbubbles were identified, as seen in Figs. 3.40-3.44. These formations have a measured diameter ranging from 1.02 μm to 6.87 μm. In addition, formations of ice in specific areas of the sample were identified (see Fig. 3.43). However, ice does not develop across the surface of the bubbles and it does not seem to influence the morphology of the bubbles, due to the high freezing rate.

The reason why formations of bubbles were visible after vitrification of the sample at high pressure but not after vitrification at ambient pressure may involve the separation of phases between the two liquids: water and MIL. In particular, it is possible that as the MIL phase has created formations on the sample's surface, NBs that had existed in the water phase were redispersed into the MIL phase, where they may have dissolved. Ice does not seem to have spread on the surface of the sample, preventing the observation of the NBs, and therefore it is not considered responsible for not observing any NBs. Also, another parameter that should be taken into consideration is the size of the NBs. If the NBs were too small, it would be more difficult to identify them on the surface of the sample. However, the microscope's resolution of our cryo-SEM facility is 0.9 nm at 15 kV and 1.6 nm at 1 kV and therefore it is rather unlikely that we would not identify any NBs due to their small size. Furthermore, as only microbubbles have been imaged after vitrification at high pressure, it is deemed that high pressure (2000 bar) during the preliminary freezing is the reason why coalescence of NBs was achieved and resulted in the formation of the microbubbles imaged. Moreover, web-like formations were not observed after freezing at high-pressure, due to the high freezing rate that did not enable the separation of phases, i.e. the phase of pure water and the phase of the MIL.

DLS measurements and observation of the Tyndall effect were performed for O_2 and air NBs in pure water that had been produced by counterflow hydrodynamic cavitation with the same generator [12]. After 30 min of processing time, the mean size of the O_2 NBs and the air NBs, according to DLS, were 350 nm and 430 nm respectively. Moreover, after observation of the Tyndall effect, the solution with N_2 NBs scattered the light of a green laser beam (with wavelength 495-570 nm). This observation was considered indicative for the existence of NBs with diameters between 400 and 900 nm. After freezing at ambient pressure, we could not observe any NBs. This fact is considered to be the result of NBs being pushed together in the MIL phase and subsequently dissolving into the MIL phase. In the case of the freezing at high pressure (2000 bar) again no NBs were observed. Formations attributed to N_2 microbubbles with diameters ranging from 1.02 μm to 6.87 μm were only identified (Figs. 3.40-3.44). These diameters do not agree with the DLS measurements nor with the observation of the Tyndall effect. It is suggested that no observation of NBs is associated with the high pressure (2000 bar) applied due to the preliminary freezing, that led to coalescence of the NBs.

5. Comparison of results with literature

In this study, the cryo-SEM technique is applied for the first time for the observation of bulk NBs. Studies for the visualization of NBs that have been found in literature, apply other techniques for the imaging. Ushida et al. applied TEM for the observation of O_2 NBs by preparing a replica sample [63],[103]. In Figure 5.1, an O_2 NB in pure water imaged with the cryo-SEM facility of our lab is compared to O_2 NBs in pure water imaged with TEM by Ushida et al. [63]. The NBs have, in both cases, a spherical shape.

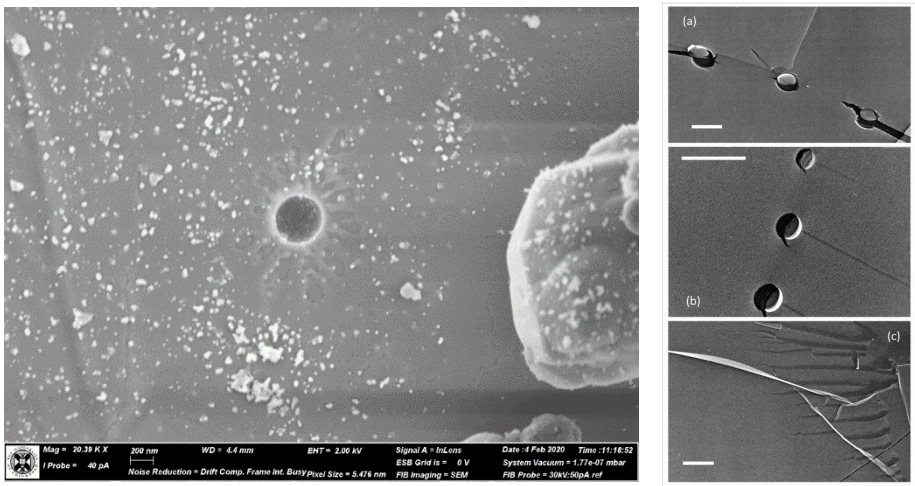

Figure 5.1. *(Left) Formation attributed to an O_2 NB with measured diameter of 430 nm in pure water. The sample was frozen with liquid nitrogen at high pressure (2000 bar). Ice has developed around the formation. (Right) TEM images of freeze-fractured replica of pure O_2 MNBs in pure water [63]. Each scale bar indicates 500 nm. Spherical or oval NBs were imaged and were located in ice crystallites (smooth surface) or on their grain boundaries. These NBs had a diameter equal to (a) 500 nm or (b) 200 nm. (c) Replica sample of pure water without aeration, imaged as a control.*

In another study, Ohgaki et al. applied SEM for the observation of methane, nitrogen, and argon NBs by preparing a replica film [8]. In Figure 5.2, O_2 NBs observed in pure water with MIL at the cryo-SEM facility of our lab are compared to nitrogen NBs in pure water imaged with SEM by Ohgaki et al. [8].

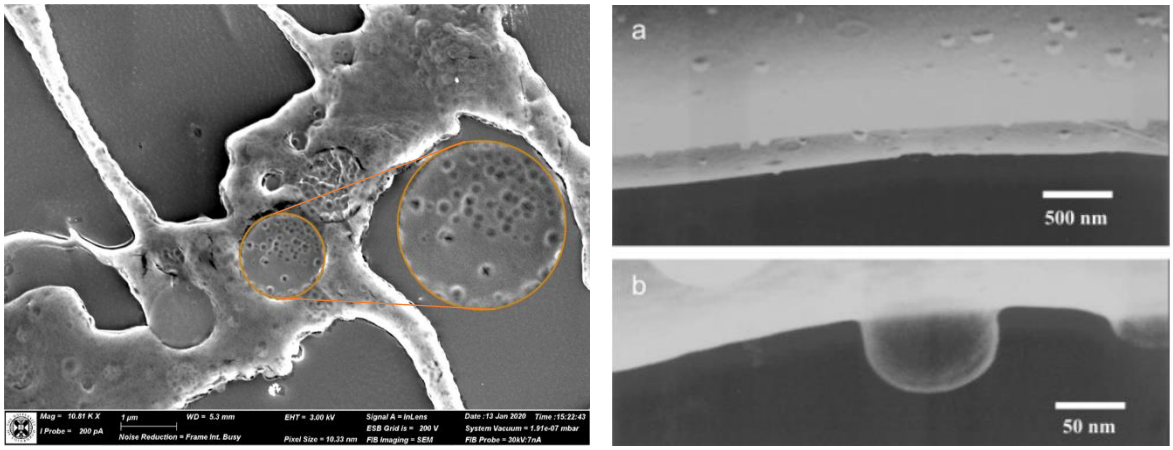

Figure 5.2. *(Left) Blots attributed to O_2 NBs in pure water blended with MIL. One specific area of blots has been magnified. The sample was frozen with liquid nitrogen at ambient pressure. Due to their minute size their diameter was not measured accurately but is smaller than 200 nm. (Right) (a) SEM image of nitrogen NBs located in an aqueous solution (b) and a magnified image of a nitrogen bubble (50 nm in radius) [8]. The sample was prepared in the form of a replica film and the observation was performed by means of a SEM of field emission type.*

Moreover, cryo-TEM has been applied by Li et al. [109] for the observation of N_2 NBs between two TEM as well as by Hernandez et al. [111] and Leon et al. [112] for the observation of NBs with perfluorocarbon gas cores. In Figure 5.3, O_2 NBs observed in pure water blended with MIL at the cryo-SEM facility of our lab are compared to nitrogen NBs in pure water imaged with cryo-SEM by Li et al. [109].

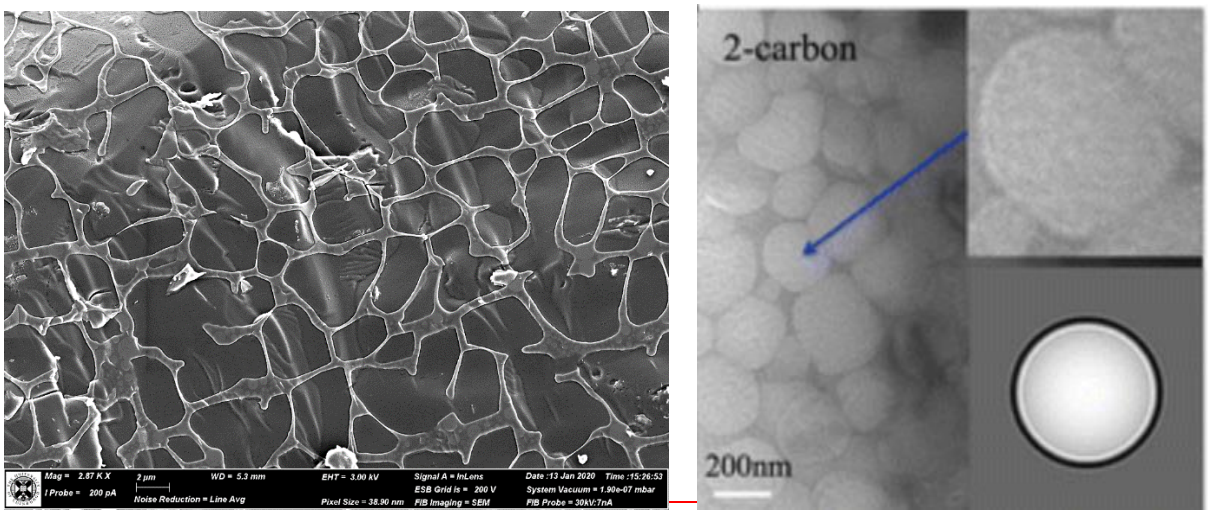

Figure 5.3. *(Left) Web-like formations on the surface of the sample of pure water with O_2 NBs blended with MIL. The sample was frozen with liquid nitrogen at ambient pressure. Inside the web-like formations there are spherical shapes attributed to O_2 NBs and microbubbles. Measurements of their diameter were made in different parts of the web-like formations and they have been found to range from 136 nm to 1.37 μm. (Right) Cryo-EM image that presents reaction solutions between two TEM grids coated with continuous carbon films [109]. N_2 NBs were observed, and one of them (that is indicated with an arrow) is magnified in the upper inset. The lower inset presents a simulated bubble with a diameter of 50 nm.*

Last but not least, Usukura et al. [110] developed a cryo-EM facility that performed SEM and STEM simultaneously to observe nanobubbles in water poured into holes in a QUANTIFOIL membrane.

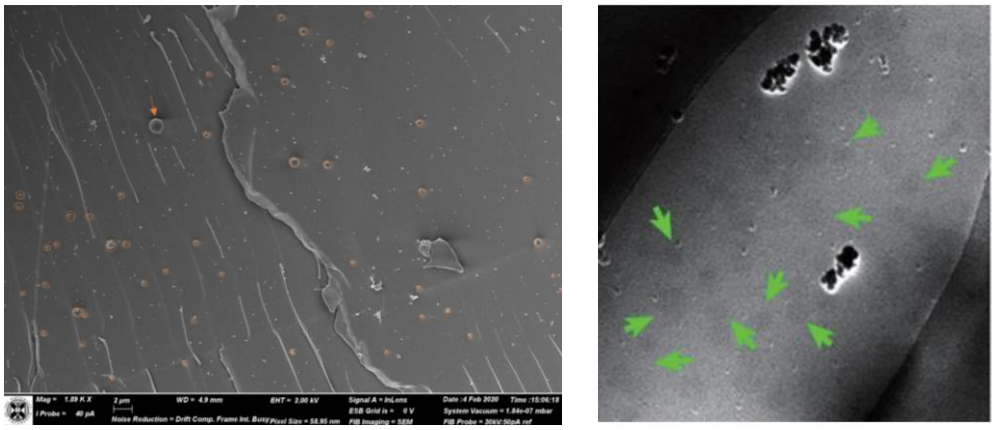

Figure 5.4. *(Left) Formations attributed to an O_2 microbubble (indicated with an arrow) of measured diameter 1.51 μm and to O_2 NBs (indicated with circles) of measured diameters ranging from 258 nm to 998 nm in pure water blended with MIL. The sample was frozen with liquid nitrogen at high pressure (2000 bar). (Right) STEM image obtained with developed cryo-EM facility by Usukura et al. [110]. Nanobubbles in water are observed (50-100 nm), indicated with arrows and appear dark in STEM images. SEM and STEM was performed simultaneously. In order to image the sample, water was poured into holes in a QUANTIFOIL membrane and prior to imaging, rapid freezing was performed.*

Chapter 3: Conclusions and Outlook

This is the first study, to the extent of the author's knowledge, that the technique of cryo-SEM imaging has been applied for the visualization of bulk nanobubbles in aqueous solutions. Nanobubbles generated in pure water at the "Materials & Membranes for Environmental Separations Laboratory" of NCSR "Demokritos" were visualized. Four different samples of pure water with a. O_2 NBs, b. O_2 NBs blended with magnetic ionic liquid (MIL), c. N_2 NBs and d. N_2 NBs blended with magnetic ionic liquid (MIL) were imaged. After having observed the Figures obtained, O_2 nanobubbles with spherical shapes were identified, and therefore the visualization of bulk nanobubbles in aqueous solutions with cryo-SEM imaging was successfully achieved. Moreover, the diameters of the bubbles observed were measured and the morphology of the four samples (a-d) imaged after cryo-SEM was discussed.

In particular, O_2 NBs were visible both in pure water and pure water blended with MIL (samples a and b) after preliminary freezing at ambient pressure and high pressure (2000 bar). A small number of O_2 microbubbles was also identified in the case of preliminary freezing at ambient pressure. Although their measured diameters did not exceed 1.58 μm, in the case of freezing at 2000 bar, various O_2 microbubbles were observed with measured diameters ranging from 1.75 μm to 9.80 μm and even bigger bubbles (>10 μm). One explanation could be that due to high pressure (2000 bar) during the freezing process, NBs merged thus producing bigger bubbles. Therefore, it is suggested that the high pressure (2000 bar) during the preliminary freezing was the reason for the coalescence of O_2 NBs present in the initial sample.

In the case of pure water with N_2 NBs and pure water with N_2 NBs blended with MIL (samples c and d), N_2 NBs could not be visualized at ambient pressure nor at high pressure (2000 bar). N_2 microbubbles and bigger bubbles were identified after preliminary freezing at 2000 bar for samples c and d. Their observation is attributed to the high pressure leading to the coalescence of N_2 NBs and the formation of microbubbles and bigger bubbles, as in the case O_2 NBs after high-pressure freezing. In the case of preliminary freezing at ambient pressure, ice developed across the surface may have been the reason that NBs could not be identified for sample c. Specifically, ice formations may have prevented the observation of NBs as they would be "hidden" behind the ice. In addition, the smaller the NBs were, the more difficult it would be to observe the NBs if ice developed on their surface.

Ice formation is an important parameter for the cryo-SEM that has been applied. Generally, if the cooling of the sample is achieved abruptly, it vitrifies the sample by preserving its nanostructure. It was expected that after preliminary freezing at ambient pressure, due to the low freezing rate, there would be time for ice to potentially develop on the surface of the sample and influence its morphology. This expectation was confirmed by the development of ice observed on the surface of the sample that extends even on the surface of the O_2 nanobubbles visualized, in the case of pure water with O_2 NBs (sample a). Ice development on sample a is considered to be the reason why the NBs we observed are bigger in correlation with the mean size of NBs measured by the DLS technique (as smaller bubbles would be "hidden" behind the ice imaged across the surface of sample a).

However, after preliminary freezing at ambient pressure for the pure water with O_2 NBs (sample b) and the pure water with N_2 NBs (sample d) that were blended with MIL, ice development was not observed. In these samples (b and d), web-like formations were observed. In particular, these formations are attributed to be the MIL phase that has separated from the phase of the pure water.

These formations of the MIL phase may be the result of different molecular weights between the pure water and the MIL.

In the case of preliminary freezing at high pressure (2000 bar), ice has developed at specific areas on the surface of all the samples imaged. Nevertheless, ice has not developed across the whole area or on the surface of the nanobubbles, and therefore it does not influence the observation of the bubbles. In particular, for samples a, b and d, amorphous ice has developed at specific areas on the surface of the sample imaged, whereas for sample c hexagonal ice crystals have been visualized. The creation of amorphous ice as well as the formation of hexagonal ice crystals are considered to be the result of insufficient rapid freezing.

In addition, signs of unevenness and roughness on the external surface of a O_2 microbubble and a O_2 NB were observed for pure water blended with MIL (sample b). These characteristics are considered to be the result of contamination accumulated on the liquid/gas interface of the bubbles and can be explained by the contamination theory according to which contaminants contribute to the long-term stability of nanobubbles. These contaminants may accumulate on the surface of the NBs during their generation process. Moreover, in the samples of pure water with N_2 NBs (samples c and d), artefacts have been imaged after preliminary freezing at high pressure (2000 bar). These artefacts may have formed either during the NBs' generation process in pure water, or during the preparation procedure before the cryo-SEM imaging.

In conclusion, cryo-SEM imaging was applied successfully for the first time for the observation of bulk nanobubbles. Specifically, in this study, O_2 nanobubbles were successfully imaged in pure water, and consequently their size was measured, and their morphology was identified. For all samples imaged, the formations identified through cryo-SEM were correlated to the preparation method for preliminary freezing applied before imaging. Therefore, an assessment of how the cryo-SEM technique followed influences the resulted images is made.

Cryo-SEM experiments on the sample of pure water (control sample), without nanobubbles, were not conducted. These experiments could allow to assess how the existence of nanobubbles alters the nature of the bulk solution, by comparing the results obtained after imaging the control sample with the results obtained after imaging the samples that contained nanobubbles. Therefore, cryo-SEM imaging of the control sample is proposed in order to further enhance the validity of the results presented in this study.

Moreover, in order to further assess how the preparation method implicates with the results obtained, follow-up experiments of the same samples as well as other samples containing bulk nanobubbles in aqueous solutions are proposed. The ultimate goal would be to standardise a process for observing NBs through cryo-electron microscopy techniques in order to obtain images of NBs, measure their sizes, and better understand their morphology, which could subsequently provide further information on their stability and the mechanisms behind their long-term existence. Having a better understanding of the nature of nanobubbles could help us acknowledge their influence on each process they are applied to (e.g. flotation, surface cleaning), and further improve the already-existing processes.

References

[1] Lohse, D. and Zhang, X. (2015). Surface nanobubbles and nanodroplets. *Reviews of Modern Physics*, 87(3), pp.981-1035.

[2] Zhang, X., Zhang, X., Sun, J., Zhang, Z., Li, G., Fang, H., Xiao, X., Zeng, X. and Hu, J. (2007). Detection of Novel Gaseous States at the Highly Oriented Pyrolytic Graphite−Water Interface. *Langmuir*, 23(4), pp.1778-1783.

[3] Michailidi, E. D., Bomis, G., Varoutoglou, A., Efthimiadou, E. K., Mitropoulos, A. C., & Favvas, E. P. (2019). Fundamentals and applications of nanobubbles. Advanced Low-Cost Separation Techniques in Interface Science. Interface Science and Technology, 69–99. doi: 10.1016/b978-0-12-814178-6.00004-2

[4] Parker, J., Claesson, P. and Attard, P. (1994). Bubbles, cavities, and the long-ranged attraction between hydrophobic surfaces. *The Journal of Physical Chemistry*, 98(34), pp.8468-8480.

[5] Lou, S., Ouyang, Z., Zhang, Y., Li, X., Hu, J., Li, M. and Yang, F. (2000). Nanobubbles on solid surface imaged by atomic force microscopy. *Journal of Vacuum Science & Technology B: Microelectronics and Nanometer Structures*, 18(5), p.2573.

[6] Ishida, N., Inoue, T., Miyahara, M. and Higashitani, K. (2000). Nano Bubbles on a Hydrophobic Surface in Water Observed by Tapping-Mode Atomic Force Microscopy. *Langmuir*, 16(16), pp.6377-6380.

[7] Seddon, J. and Lohse, D. (2011). Nanobubbles and micropancakes: gaseous domains on immersed substrates. *Journal of Physics: Condensed Matter*, 23(13), p.133001.

[8] Ohgaki, K., Khanh, N. Q., Joden, Y., Tsuji, A., & Nakagawa, T. (2010). Physicochemical approach to nanobubble solutions. Chemical Engineering Science, 65(3), 1296–1300. doi: 10.1016/j.ces.2009.10.003

[9] Nirmalkar, N., Pacek, A. W., & Barigou, M. (2018). On the Existence and Stability of Bulk Nanobubbles. Langmuir, 34(37), 10964–10973. doi: 10.1021/acs.langmuir.8b01163

[10] Weijs, J. H., Seddon, J. R. T., & Lohse, D. (2012). Diffusive Shielding Stabilizes Bulk Nanobubble Clusters. ChemPhysChem, 13(8), 2197–2204. doi: 10.1002/cphc.201100807

[11] Ebina, K., Shi, K., Hirao, M., Hashimoto, J., Kawato, Y., Kaneshiro, S., … Yoshikawa, H. (2013). Oxygen and Air Nanobubble Water Solution Promote the Growth of Plants, Fishes, and Mice. PLoS ONE, 8(6). doi: 10.1371/journal.pone.0065339

[12] Michailidi, E. D., Bomis, G., Varoutoglou, A., Kyzas, G. Z., Mitrikas, G., Mitropoulos, A. C., … Favvas, E. P. (2020). Bulk nanobubbles: Production and investigation of their formation/stability mechanism. Journal of Colloid and Interface Science, 564, 371–380. doi: 10.1016/j.jcis.2019.12.093

[13] Epstein, P. and Plesset, M. (1950). On the Stability of Gas Bubbles in Liquid-Gas Solutions. *The Journal of Chemical Physics*, 18(11), pp.1505-1509.

[14] Ljunggren, S. and Eriksson, J. (1997). The lifetime of a colloid-sized gas bubble in water and the cause of the hydrophobic attraction. *Colloids and Surfaces A: Physicochemical and Engineering Aspects*, 129-130, pp.151-155.

[15] Alheshibri, M., Qian, J., Jehannin, M. and Craig, V. (2016). A History of Nanobubbles. *Langmuir*, 32(43), pp.11086-11100.

[16] Dube, N., Oeffinger, B. and Wheatley, M. (2003). Development and characterization of a nano-sized surfactant stabilized contrast agent for diagnostic ultrasound. *IEEE 29th Annual Proceedings of Bioengineering Conference*.

[17] Zhang, X., Maeda, N. and Craig, V. (2006). Physical Properties of Nanobubbles on Hydrophobic Surfaces in Water and Aqueous Solutions. *Langmuir*, 22(11), pp.5025-5035.

[18] Kobayashi, H., Maeda, S., Kashiwa, M. and Fujita, T. (2014). Measurement and identification of ultrafine bubbles by resonant mass measurement method. *International Conference on Optical Particle Characterization (OPC 2014)*.

[19] Seo, D., German, S., Mega, T. and Ducker, W. (2015). Phase State of Interfacial Nanobubbles. *The Journal of Physical Chemistry C*, p.150615070529004.

[20] Ducker, W. (2009). Contact Angle and Stability of Interfacial Nanobubbles. *Langmuir*, 25(16), pp.8907-8910.

[21] Brenner, M. and Lohse, D. (2008). Dynamic Equilibrium Mechanism for Surface Nanobubble Stabilization. *Physical Review Letters*, 101(21).

[22] Seddon, J., Lohse, D., Ducker, W. and Craig, V. (2012). A Deliberation on Nanobubbles at Surfaces and in Bulk. *ChemPhysChem*, 13(8), pp.2179-2187.

[23] Simonsen, A., Hansen, P. and Klösgen, B. (2004). Nanobubbles give evidence of incomplete wetting at a hydrophobic interface. *Journal of Colloid and Interface Science*, 273(1), pp.291-299.

[24] Borkent, B., de Beer, S., Mugele, F. and Lohse, D. (2010). On the Shape of Surface Nanobubbles. *Langmuir*, 26(1), pp.260-268.

[25] Parkinson, L., Sedev, R., Fornasiero, D. and Ralston, J. (2008). The terminal rise velocity of 10–100 μm diameter bubbles in water. *Journal of Colloid and Interface Science*, 322(1), pp.168-172.

[26] Das, S., Snoeijer, J. and Lohse, D. (2010). Effect of impurities in description of surface nanobubbles. *Physical Review E*, 82(5).

[27] Dammer, S. and Lohse, D. (2006). Gas Enrichment at Liquid-Wall Interfaces. *Physical Review Letters*, 96(20).

[28] Schmelzer, J. W. P. (2005). Summary and Outlook. Nucleation Theory and Applications, 447–452. doi: 10.1002/3527604790.ch12

[29] Creux, P., Lachaise, J., Graciaa, A. and Beattie, J. (2007). Specific Cation Effects at the Hydroxide-Charged Air/Water Interface. *The Journal of Physical Chemistry C*, 111(9), pp.3753-3755.

[30] Jin, F., Li, J., Ye, X. and Wu, C. (2007). Effects of pH and Ionic Strength on the Stability of Nanobubbles in Aqueous Solutions of α-Cyclodextrin. *The Journal of Physical Chemistry B*, 111(40), pp.11745-11749.

[31] Bunkin, N., Shkirin, A., Suyazov, N., Babenko, V., Sychev, A., Penkov, N., Belosludtsev, K. and Gudkov, S. (2016). Formation and Dynamics of Ion-Stabilized Gas Nanobubble Phase in the Bulk of Aqueous NaCl Solutions. *The Journal of Physical Chemistry B*, 120(7), pp.1291-1303.

[32] Creux, P., Lachaise, J., Graciaa, A., Beattie, J. and Djerdjev, A. (2009). Strong Specific Hydroxide Ion Binding at the Pristine Oil/Water and Air/Water Interfaces. *The Journal of Physical Chemistry B*, 113(43), pp.14146-14150.

[33] Quincke, G. (1861). Ueber die Fortführung materieller Theilchen durch strömende Elektricität. *Annalen der Physik und Chemie*, 189(8), pp.513-598.

[34] McTaggart, H. (1914). XXXIII. The electrification at liquid-gas surfaces. *The London, Edinburgh, and Dublin Philosophical Magazine and Journal of Science*, 27(158), pp.297-314.

[35] Beattie, J., Djerdjev, A. and Warr, G. (2009). The surface of neat water is basic. *Faraday Discuss.*, 141, pp.31-39.

[36] Hamamoto, S., Takemura, T., Suzuki, K. and Nishimura, T. (2018). Effects of pH on nano-bubble stability and transport in saturated porous media. *Journal of Contaminant Hydrology*, 208, pp.61-67.

[37] Graciaa, A., Morel, G., Saulner, P., Lachaise, J. and Schechter, R. (1995). The ζ-Potential of Gas Bubbles. *Journal of Colloid and Interface Science*, 172(1), pp.131-136.

[38] Takahashi, M. (2005). ζ Potential of Microbubbles in Aqueous Solutions: Electrical Properties of the Gas−Water Interface. *The Journal of Physical Chemistry B*, 109(46), pp.21858-21864.

[39] Attard, P., Moody, M. and Tyrrell, J. (2002). Nanobubbles: the big picture. *Physica A: Statistical Mechanics and its Applications*, 314(1-4), pp.696-705.

[40] Hampton, M. and Nguyen, A. (2010). Nanobubbles and the nanobubble bridging capillary force. *Advances in Colloid and Interface Science*, 154(1-2), pp.30-55.

[41] Ushikubo, F., Enari, M., Furukawa, T., Nakagawa, R., Makino, Y., Kawagoe, Y. and Oshita, S. (2010). Zeta-potential of Micro- and/or Nano-bubbles in Water Produced by Some Kinds of Gases. *IFAC Proceedings Volumes*, 43(26), pp.283-288.

[42] Zhang, M. (2018). *SYSTEMATIC INVESTIGATION OF INTERACTIONS OF BULK NANOBUBBLES WITH SOFT MATTER*. Ph.D. University of Twente.

[43] Peng, H., Hampton, M. and Nguyen, A. (2013). Nanobubbles Do Not Sit Alone at the Solid–Liquid Interface. *Langmuir*, 29(20), pp.6123-6130.

[44] Berkelaar, R., Dietrich, E., Kip, G., Kooij, E., Zandvliet, H. and Lohse, D. (2014). Exposing nanobubble-like objects to a degassed environment. *Soft Matter*, 10(27), p.4947.

[45] Bonaccurso, E. and Gillies, G. (2004). Revealing Contamination on AFM Cantilevers by Microdrops and Microbubbles. *Langmuir*, 20(26), pp.11824-11827.

[46] Lo, Y., Huefner, N., Chan, W., Dryden, P., Hagenhoff, B. and Beebe, T. (1999). Organic and Inorganic Contamination on Commercial AFM Cantilevers. *Langmuir*, 15(19), pp.6522-6526.

[47] Kelsall, G., Tang, S., Yurdakul, S. and Smith, A. (1996). Electrophoretic behaviour of bubbles in aqueous electrolytes. *Journal of the Chemical Society, Faraday Transactions*, 92(20), p.3887.

[48] Bunkin, N., Kochergin, A., Lobeyev, A., Ninham, B. and Vinogradova, O. (1996). Existence of charged submicrobubble clusters in polar liquids as revealed by correlation between optical cavitation and electrical conductivity. *Colloids and Surfaces A: Physicochemical and Engineering Aspects*, 110(2), pp.207-212.

[49] Bunkin, N. and Lobeev, A. (1994). Bubbston-cluster structure under conditions of optical breakdown in a liquid. *Quantum Electronics*, 24(4), pp.297-301.

[50] Bunkin, N., Shkirin, A., Ignatiev, P., Chaikov, L., Burkhanov, I. and Starosvetskij, A. (2012). Nanobubble clusters of dissolved gas in aqueous solutions of electrolyte. I. Experimental proof. *The Journal of Chemical Physics*, 137(5), p.054706.

[51] Bunkin, N. and Shkirin, A. (2012). Nanobubble clusters of dissolved gas in aqueous solutions of electrolyte. II. Theoretical interpretation. *The Journal of Chemical Physics*, 137(5), p.054707.

[52] Fan, M., Tao, D., Honaker, R., & Luo, Z. (2010). Nanobubble generation and its application in froth flotation (part I): nanobubble generation and its effects on properties of microbubble and millimeter scale bubble solutions. Mining Science and Technology (China), 20(1), 1–19. doi: 10.1016/s1674-5264(09)60154-x

[53] Agarwal, A., Ng, W. J., & Liu, Y. (2011). Principle and applications of microbubble and nanobubble technology for water treatment. Chemosphere, 84(9), 1175–1180. doi: 10.1016/j.chemosphere.2011.05.054

[54] Kim, J.-Y., Song, M.-G., & Kim, J.-D. (2000). Zeta Potential of Nanobubbles Generated by Ultrasonication in Aqueous Alkyl Polyglycoside Solutions. Journal of Colloid and Interface Science, 223(2), 285–291. doi: 10.1006/jcis.1999.6663

[55] Cho, S.-H., Kim, J.-Y., Chun, J.-H., & Kim, J.-D. (2005). Ultrasonic formation of nanobubbles and their zeta-potentials in aqueous electrolyte and surfactant solutions. Colloids and Surfaces A: Physicochemical and Engineering Aspects, 269(1-3), 28–34. doi: 10.1016/j.colsurfa.2005.06.063

[56] Oeffinger, B. E., & Wheatley, M. A. (2004). Development and characterization of a nano-scale contrast agent. Ultrasonics, 42(1-9), 343–347. doi: 10.1016/j.ultras.2003.11.011

[57] Ahmadi, R., & Darban A. K. (2013). Modeling and Optimization of Nano-bubble Generation Process Using Response Surface Methodology. International Journal of Nanoscience and Nanotechnology, 9(3), 151-162

[58] Luttrell, G. H., & Young, C. (2012). Separation Technologies for Minerals, Coal, and Earth Resources. Society for Mining, Metallurgy and Exploration Incorporated, 458.

[59] Wu, C., Nesset, K., Masliyah, J., & Xu, Z. (2012). Generation and characterization of submicron size bubbles. Advances in Colloid and Interface Science, 179-182, 123–132. doi: 10.1016/j.cis.2012.06.012

[60] Kikuchi, K., Ioka, A., Oku, T., Tanaka, Y., Saihara, Y., & Ogumi, Z. (2009). Concentration determination of oxygen nanobubbles in electrolyzed water. Journal of Colloid and Interface Science, 329(2), 306–309. doi: 10.1016/j.jcis.2008.10.009

[61] Kikuchi, K., Tanaka, Y., Saihara, Y., & Ogumi, Z. (2006). Study of hydrogen nanobubbles in solution in the vicinity of a platinum wire electrode using double-potential step chronoamperometry. Electrochimica Acta, 52(3), 904–913. doi: 10.1016/j.electacta.2006.06.026

[62] Kikuchi, K., Tanaka, Y., Saihara, Y., Maeda, M., Kawamura, M., & Ogumi, Z. (2006). Concentration of hydrogen nanobubbles in electrolyzed water. Journal of Colloid and Interface Science, 298(2), 914–919. doi: 10.1016/j.jcis.2006.01.010

[63] Uchida, T., Oshita, S., Ohmori, M., Tsuno, T., Soejima, K., Shinozaki, S., … Mitsuda, K. (2011). Transmission electron microscopic observations of nanobubbles and their capture of impurities in wastewater. Nanoscale Research Letters, 6(1). doi: 10.1186/1556-276x-6-295

[64] An, H., Liu, G., Atkin, R., & Craig, V. S. J. (2015). Surface Nanobubbles in Nonaqueous Media: Looking for Nanobubbles in DMSO, Formamide, Propylene Carbonate, Ethylammonium Nitrate, and Propylammonium Nitrate. ACS Nano, 9(7), 7596–7607. doi: 10.1021/acsnano.5b02915

[65] Xu, C., Peng, S., Qiao, G. G., Gutowski, V., Lohse, D., & Zhang, X. (2014). Nanobubble formation on a warmer substrate. Soft Matter, 10(39), 7857–7864. doi: 10.1039/c4sm01025f

[66] Yang, S., Dammer, S. M., Bremond, N., Zandvliet, H. J. W., Kooij, E. S., & Lohse, D. (2007). Characterization of Nanobubbles on Hydrophobic Surfaces in Water. Langmuir, 23(13), 7072–7077. doi: 10.1021/la070004i

[67] Guan, M., Guo, W., Gao, L., Tang, Y., Hu, J., & Dong, Y. (2012). Investigation on the Temperature Difference Method for Producing Nanobubbles and Their Physical Properties. ChemPhysChem, 13(8), 2115–2118. doi: 10.1002/cphc.201100912

[68] Zhang, X., Li, G., Maeda, N. and Hu, J. (2006). Removal of Induced Nanobubbles from Water/Graphite Interfaces by Partial Degassing. Langmuir, 22(22), pp.9238-9243.

[69] Kline, T., Paxton, W., Mallouk, T. and Sen, A. (2005). Catalytic Nanomotors: Remote-Controlled Autonomous Movement of Striped Metallic Nanorods. *Angewandte Chemie International Edition*, 44(5), pp.744-746.

[70] Shen, G., Zhang, X., Ming, Y., Zhang, L., Zhang, Y. and Hu, J. (2008). Photocatalytic Induction of Nanobubbles on TiO_2 Surfaces. The Journal of Physical Chemistry C, 112(11), pp.4029-4032.

[71] Xiao, W., Ke, S., Quan, N., Zhou, L., Wang, J., Zhang, L., Dong, Y., Qin, W., Qiu, G. and Hu, J. (2018). The Role of Nanobubbles in the Precipitation and Recovery of Organic-Phosphine-Containing Beneficiation Wastewater. *Langmuir*, 34(21), pp.6217-6224.

[72] Kyzas, G. Z., Lazaridis, N. K., & Matis, K. A. (2019). Flotation: Recent innovations in an interesting and effective separation process. Interface Science and Technology, 15-42. doi: 10.1016/B978-0-12-814178-6.00002-9

[73] Gupta A., Yan D. (2016). Flotation. Mineral Processing Design and Operations (Second Edition), 689-741. doi: 10.1016/B978-0-444-63589-1.00018-6

[74] Fan, M., Chao, Y., Tao, D. (2012). Fundamental studies in nanobubble generation and applications in flotation. SME-Meeting, pp. 457–469.

[75] Sobhy, A. (2013). Cavitation nanobubble enhanced flotation process for more efficient coal recovery. Ph.D Thesis, College of Engineering-University of Kentucky, 145p.

[76] Sobhy, A., & Tao, D. (2013). Nanobubble column flotation of fine coal particles and associated fundamentals. International Journal of Mineral Processing, 124, 109–116. doi: 10.1016/j.minpro.2013.04.016

[77] Fan, M., Tao, D., Honaker, R., & Luo, Z. (2010). Nanobubble generation and its applications in froth flotation (part II): fundamental study and theoretical analysis. Mining Science and Technology (China), 20(2), 159–177. doi: 10.1016/s1674-5264(09)60179-4

[78] Yamasaki, K., Sakata, K., & Chuhjoh, K. (2006). U.S. Patent No. US7662288B2. Retrieved from https://patents.google.com/patent/US7662288B2/en

[79] Yamasaki, K., Uda, K., & Chuhjoh, K. (2006). U.S. Patent No. US7578942B2. Retrieved from https://patents.google.com/patent/US7578942B2/en

[80] Wang, X., & Zhang, Y. (2009). Degradation of alachlor in aqueous solution by using hydrodynamic cavitation. Journal of Hazardous Materials, 161(1), 202–207. doi: 10.1016/j.jhazmat.2008.03.073

[81] Kalumuck, K. M., & Chahine, G. L. (2000). The Use of Cavitating Jets to Oxidize Organic Compounds in Water. Journal of Fluids Engineering, 122(3), 465–470. doi: 10.1115/1.1286993

[82] Wang, X., Wang, J., Guo, P., Guo, W., & Li, G. (2008). Chemical effect of swirling jet-induced cavitation: Degradation of rhodamine B in aqueous solution. Ultrasonics Sonochemistry, 15(4), 357–363. doi: 10.1016/j.ultsonch.2007.09.008

[83] Arrojo, S., Benito, Y., & Tarifa, A. M. (2008). A parametrical study of disinfection with hydrodynamic cavitation. Ultrasonics Sonochemistry, 15(5), 903–908. doi: 10.1016/j.ultsonch.2007.11.001

[84] Mezule, L., Tsyfansky, S., Yakushevich, V., & Juhna, T. (2009). A simple technique for water disinfection with hydrodynamic cavitation: Effect on survival of Escherichia coli. Desalination, 248(1-3), 152–159. doi: 10.1016/j.desal.2008.05.051

[85] Chen, K. (2007). U.S. Patent No. US7488416B2. Retrieved from https://patents.google.com/patent/US7488416B2/en

[86] Wu, Z., Chen, H., Dong, Y., Mao, H., Sun, J., Chen, S., … Hu, J. (2008). Cleaning using nanobubbles: Defouling by electrochemical generation of bubbles. Journal of Colloid and Interface Science, 328(1), 10–14. doi: 10.1016/j.jcis.2008.08.064

[87] Wu, Z., Zhang, X., Zhang, X., Sun, J., Dong, Y., & Hu, J. (2007). In situ AFM observation of BSA adsorption on HOPG with nanobubble. Chinese Science Bulletin, 52(14), 1913–1919. doi: 10.1007/s11434-007-0288-8

[88] Liu, G., Wu, Z., & Craig, V. S. J. (2008). Cleaning of Protein-Coated Surfaces Using Nanobubbles: An Investigation Using a Quartz Crystal Microbalance. The Journal of Physical Chemistry C, 112(43), 16748–16753. doi: 10.1021/jp805143c

[89] Zhu, J., An, H., Alheshibri, M., Liu, L., Terpstra, P. M. J., Liu, G., & Craig, V. S. J. (2016). Cleaning with Bulk Nanobubbles. Langmuir, 32(43), 11203–11211. doi: 10.1021/acs.langmuir.6b01004

[90] Ghadimkhani, A., Zhang, W., & Marhaba, T. (2016). Ceramic membrane defouling (cleaning) by air Nano Bubbles. Chemosphere, 146, 379–384. doi: 10.1016/j.chemosphere.2015.12.023

[91] Yoshida, S., Kitano, M., & Eguchi, H. (1996). Water Uptake And Growth Of Cucumber Plants (Cucumis Sativus L.) Under Control Of Dissolved O_2 Concentration In Hydroponics. Acta Horticulturae, (440), 199–204. doi: 10.17660/actahortic.1996.440.35

[92] Owerkowicz, T., Elsey, R. M., & Hicks, J. W. (2009). Atmospheric oxygen level affects growth trajectory, cardiopulmonary allometry and metabolic rate in the American alligator (Alligator mississippiensis). Journal of Experimental Biology, 212(9), 1237–1247. doi: 10.1242/jeb.023945

[93] Ushikubo, F. Y., Oshita, S., Furukawa, T., Yoshio, M., Kawagoe, Y., & Shiina, T., (2008). A study of water containing micro and nano-bubbles and its possible effect on physiological activity. International Conference of Agricultural Engineering

[94] Hayakumo, S., Arakawa, S., Takahashi, M., Kondo, K., Mano, Y., & Izumi, Y. (2014). Effects of ozone nano-bubble water on periodontopathic bacteria and oral cells -in vitrostudies. Science and Technology of Advanced Materials, 15(5), 055003. doi: 10.1088/1468-6996/15/5/055003

[95] Dzubiella, J. (2010). Explicit and implicit modeling of nanobubbles in hydrophobic confinement. Anais Da Academia Brasileira De Ciências, 82(1), 3–12. doi: 10.1590/s0001-37652010000100002

[96] Owen, J., Mcewan, C., Nesbitt, H., Bovornchutichai, P., Averre, R., Borden, M., … Stride, E. (2016). Reducing Tumour Hypoxia via Oral Administration of Oxygen Nanobubbles. Plos One, 11(12). doi: 10.1371/journal.pone.0168088

[97] Iijima, M., Gombodorj, N., Tachibana, Y., Tachibana, K., Yokobori, T., Honma, K., … Yamanouchi, D. (2018). Development of single nanometer-sized ultrafine oxygen bubbles to overcome the hypoxia-induced resistance to radiation therapy via the suppression of hypoxia-inducible factor 1α. International Journal of Oncology. doi: 10.3892/ijo.2018.4248

[98] Ke, S., Xiao, W., Quan, N., Dong, Y., Zhang, L., & Hu, J. (2019). Formation and Stability of Bulk Nanobubbles in Different Solutions. Langmuir, 35(15), 5250–5256. doi: 10.1021/acs.langmuir.9b00144

[99] Malvernpanalytical.com. (2020). *NanoSight LM10 | Manual Nanoparticle Characterization*. [online] Available at: https://www.malvernpanalytical.com/en/products/product-range/nanosight-range/nanosight-lm10 [Accessed 3 Mar. 2020].

[100] Filipe, V., Hawe, A., & Jiskoot, W. (2010). Critical Evaluation of Nanoparticle Tracking Analysis (NTA) by NanoSight for the Measurement of Nanoparticles and Protein Aggregates. Pharmaceutical Research, 27(5), 796–810. doi: 10.1007/s11095-010-0073-2

[101] Kyzas, G. Z., Bomis, G., Kosheleva, R. I., Efthimiadou, E. K., Favvas, E. P., Kostoglou, M., & Mitropoulos, A. C. (2019). Nanobubbles effect on heavy metal ions adsorption by activated carbon. Chemical Engineering Journal, 356, 91–97. doi: 10.1016/j.cej.2018.09.019

[102] Huang, T., Liu, S., Chuang, Y., Hsieh, H., Tsai, C., Wu, W., Tsai, C., Mirsaidov, U., Matsudaira, P., Chang, C., Tseng, F. and Chen, F. (2013). Dynamics of hydrogen nanobubbles in KLH protein solution studied with in situ wet-TEM. Soft Matter, 9(37), p.8856.

[103] Uchida, T., Liu, S., Enari, M., Oshita, S., Yamazaki, K. and Gohara, K. (2016). Effect of NaCl on the Lifetime of Micro- and Nanobubbles. Nanomaterials, 6(2), p.31.

[104] White, E., Mecklenburg, M., Singer, S., Aloni, S. and Regan, B. (2011). Imaging Nanobubbles in Water with Scanning Transmission Electron Microscopy. Applied Physics Express, 4(5), p.055201.

[105] Tomo, Y., Takahashi, K., Nishiyama, T., Ikuta, T. and Takata, Y. (2017). Nanobubble nucleation studied using Fresnel fringes in liquid cell electron microscopy. International Journal of Heat and Mass Transfer, 108, pp.1460-1465.

[106] Grogan, J., Schneider, N., Ross, F. and Bau, H. (2013). Bubble and Pattern Formation in Liquid Induced by an Electron Beam. Nano Letters, 14(1), pp.359-364.

[107] Sasaki, Y., Kitaura, R., Yuk, J., Zettl, A. and Shinohara, H. (2016). Efficient preparation of graphene liquid cell utilizing direct transfer with large-area well-stitched graphene. Chemical Physics Letters, 650, pp.107-112.

[108] Hoppe, S., Sasaki, D., Kinghorn, A. and Hattar, K. (2013). In-Situ Transmission Electron Microscopy of Liposomes in an Aqueous Environment. Langmuir, 29(32), pp.9958-9961.

[109] Li, M., Tonggu, L., Zhan, X., Mega, T. and Wang, L. (2016). Cryo-EM Visualization of Nanobubbles in Aqueous Solutions. Langmuir, 32(43), pp.11111-11115.

[110] Usukura, J., Narita, A., Matsumoto, T., Usukura, E., Sunaoshi, T., Tamba, Y., Nagakubo, Y., Azuma, J., Mizuo, T., Nimura, K., Osumi, M., Tamochi, R., Ose, Y. (2018). Cryo-electron Microscope Developed for Simultaneous STEM, SEM Imaging and Its Application. Technical magazine of Electron Microscope and Analytical Instruments

[111] Hernandez, C., Gulati, S., Fioravanti, G., Stewart, P. and Exner, A. (2017). Cryo-EM Visualization of Lipid and Polymer-Stabilized Perfluorocarbon Gas Nanobubbles - A Step Towards Nanobubble Mediated Drug Delivery. Scientific Reports, 7(1).

[112] De Leon, A., Perera, R., Hernandez, C., Cooley, M., Jung, O., Jeganathan, S., Abenojar, E., Fishbein, G., Sojahrood, A., Emerson, C., Stewart, P., Kolios, M. and Exner, A. (2019). Contrast enhanced ultrasound imaging by nature-inspired ultrastable echogenic nanobubbles. *Nanoscale*, 11(33), pp.15647-15658.

[113] Nirmalkar, N., Pacek, A. W., & Barigou, M. (2018). Interpreting the interfacial and colloidal stability of bulk nanobubbles. Soft Matter, 14(47), 9643–9656. doi: 10.1039/c8sm01949e

[114] Oh, S. H., & Kim, J.-M. (2017). Generation and Stability of Bulk Nanobubbles. Langmuir, 33(15), 3818–3823. doi: 10.1021/acs.langmuir.7b00510

[115] Zhang, X. H., Quinn, A., & Ducker, W. A. (2008). Nanobubbles at the Interface between Water and a Hydrophobic Solid. Langmuir, 24(9), 4756–4764. doi: 10.1021/la703475q

[116] German, S. R., Wu, X., An, H., Craig, V. S. J., Mega, T. L., & Zhang, X. (2014). Interfacial Nanobubbles Are Leaky: Permeability of the Gas/Water Interface. ACS Nano, 8(6), 6193–6201. doi: 10.1021/nn5016049

[117] Steitz, R., Gutberlet, T., Hauss, T., Klösgen, B., Krastev, R., Schemmel, S., … Findenegg, G. H. (2003). Nanobubbles and Their Precursor Layer at the Interface of Water Against a Hydrophobic Substrate. Langmuir, 19(6), 2409–2418. doi: 10.1021/la026731p

[118] Doshi, D. A., Watkins, E. B., Israelachvili, J. N., & Majewski, J. (2005). Reduced water density at hydrophobic surfaces: Effect of dissolved gases. Proceedings of the National Academy of Sciences, 102(27), 9458–9462. doi: 10.1073/pnas.0504034102

[119] Mezger, M., Reichert, H., Schoder, S., Okasinski, J., Schroder, H., Dosch, H., Palms, D., Ralston, J. and Honkimaki, V. (2006). High-resolution in situ x-ray study of the hydrophobic gap at the water-octadecyl-trichlorosilane interface. Proceedings of the National Academy of Sciences, 103(49), pp.18401-18404.

[120] Liu, Y. and Dillon, S. (2014). In situ observation of electrolytic H_2 evolution adjacent to gold cathodes. Chem. Commun., 50(14), pp.1761-1763.

[121] Carr, M., Hillman, A., Lubetkin, S. and Swann, M. (1989). Detection of electrolytically generated bubbles using an electrochemical quartz crystal microbalance. Journal of Electroanalytical Chemistry and Interfacial Electrochemistry, 267(1-2), pp.313-320.

[122] Switkes, M. and Ruberti, J. (2004). Rapid cryofixation/freeze fracture for the study of nanobubbles at solid–liquid interfaces. Applied Physics Letters, 84(23), pp.4759-4761.

[123] Friedrich, H., Frederik, P., de With, G. and Sommerdijk, N. (2010). Imaging of Self-Assembled Structures: Interpretation of TEM and Cryo-TEM Images. Angewandte Chemie International Edition, 49(43), pp.7850-7858.

[124] Bullivant, S. and Ames, A. (1966). A SIMPLE FREEZE-FRACTURE REPLICATION METHOD FOR ELECTRON MICROSCOPY. The Journal of Cell Biology, 29(3), pp.435-447.

[125] Steere, R. (1957). ELECTRON MICROSCOPY OF STRUCTURAL DETAIL IN FROZEN BIOLOGICAL SPECIMENS. The Journal of Biophysical and Biochemical Cytology, 3(1), pp.45-60.

[126] Parente, R., Höchli, M. and Lentz, B. (1985). Morphology and phase behavior of two types of unilamellar vesicles prepared from synthetic phosphatidylcholines studied by freeze-fracture electron microscopy and calorimetry. *Biochimica et Biophysica Acta (BBA) - Biomembranes*, 812(2), pp.493-502.

[127] Emsdiasum.com. (2020). Cryogenic Specimen Prep Technical Data Sheet. [online] Available at: https://www.emsdiasum.com/microscopy/technical/datasheet/cryosem_adv.aspx [Accessed 4 Mar. 2020].

[128] Rsb.org.uk. (2020). *Focus on: Cryo-electron microscopy*. [online] Available at: https://www.rsb.org.uk/biologist-features/158-biologist/features/1582-focus-on-cryo-electron-microscopy [Accessed 4 Mar. 2020].

[129] ISSMAN, L. and TALMON, Y. (2012). Cryo-SEM specimen preparation under controlled temperature and concentration conditions. *Journal of Microscopy*, 246(1), pp.60-69.

[130] Elder, H., Gray, C., Jardine, A., Chapman, J. and Biddlecombe, W. (1982). Optimum conditions for cryoquenching of small tissue blocks in liquid coolants. *Journal of Microscopy*, 126(1), pp.45-61.

[131] Adrian, M., Dubochet, J., Lepault, J. and McDowall, A. (1984). Cryo-electron microscopy of viruses. *Nature*, 308(5954), pp.32-36.

[132] Talmon, Y., Davis, H., Scriven, L. and Thomas, E. (1979). Cold-stage microscopy system for fast-frozen liquids. *Review of Scientific Instruments*, 50(6), pp.698-704.

[133] Echlin, P., Paden, R., Dronzek, B., Wayte, R., 1970, Scanning electron microscopy of labile biological material maintained under controlled conditions, Scanning Electron Microsc. 1970: 49–56.

[134] Emsdiasum.com. (2020). *Cryogenic Specimen Prep Technical Data Sheet*. [online] Available at: https://www.emsdiasum.com/microscopy/technical/datasheet/cryosem_adv.aspx [Accessed 4 Mar. 2020].

[135] Jeol.co.jp. (2020). *JEOL Application Data Sheet*. [online] Available at: https://www.jeol.co.jp/en/applications/pdf/sm/469_en.pdf [Accessed 4 Mar. 2020].